ALLOYING ELEMENT SEGREGATION AND ITS EFFECT ON THE AUSTENITE TO FERRITE TRANSFORMATION

ALLOYING ELEMENT SEGREGATION AND ITS EFFECT ON THE AUSTENITE TO FERRITE TRANSFORMATION

By JOSHUA FEATHER B.ENG

A Thesis Submitted to the School of Graduate Studies in Partial Fulfilment of the

Requirements for the Degree Master of Applied Science

Abstract

Controlled decarburization experiments were carried out on ternary and quaternary iron alloys. The planar ferrite interfaces formed during decarburization were subsequently investigated using atom probe tomography (APT) to measure interfacial segregation. The segregation results for the Fe-Si-C, Fe-Mn-C, and Fe-Mo-C were used to improve the three-jump-model developed Zurob et al. These three systems were accurately modelled using interfacial binding energy values in agreement with the atom probe tomography results. Qualitative explanations for the modelling results of Sun et al. on the Fe-Mn-Mo-C system and Qiu et al. on the Fe-Mn-Si-C system have also been provided using the results from the atom probe tomography investigation.

Acknowledgements

My sincerest thanks to my supervisor Dr. Hatem Zurob. I am grateful for his patience and continued direction during the work of this thesis. Without his training and invaluable insights, this thesis would not have been accomplished. I am deeply thankful for the opportunity to learn from him and take part in his research.

I am indebted to Dr. Brian Langelier for his superb work on the atom probe. His expertise and insights were essential to this thesis. I am thankful for the time he took to teach me and to create solutions to the challenges faced in analyzing the results.

I wish to thank Dr. Gary Purdy and Dr. Yves Brechet for their fruitful discussions. Their advice and ideas were a great help to me as I formulated the thesis.

I thank my beloved wife Amira for her enduring patience and steadfast support. Her encouragements made this thesis possible.

Praise to the Lord, from whom all blessings flow.

Table of Contents

1.0 Introduction 1

2.0 The Ferrite Phase Transformation 2

2.1 Rate Controlling Processes 2

2.2 Element Redistribution During Transformation 5

2.3 Effects of Alloying Elements 12

2.31 Thermodynamic Contribution 12

2.32 Energy Dissipation 16

3.0 Summary of the Three-Jump-Model 19

3.1 Substitutional Element Diffusion 20

3.2 Carbon Concentration at the Interface 22

3.3 Bulk Carbon Diffusion 24

3.4 Growth Rate 25

4.0 Experimental Method 26

4.1 Controlled Decarburization Review 26

4.2 Creation of Alloys 29

4.21 Fe-Ni-C Diffusion Couple 29

4.22 Ternary and Quaternary Alloys 30

4.3 Decarburization....31

4.4 Atom Probe Tomography....32

4.41 Review of Technique....32

4.42 Common Artefacts....35

4.43 Atom Probe Tomography Method....36

5.0 APT Results....36

5.1 Ternary Systems....37

5.11 Fe-Ni-C....38

5.12 Fe-Al-C....40

5.13 Fe-Mn-C....42

5.14 Fe-Mo-C....43

5.15 Fe-Si-C....44

5.2 Quaternary Systems....45

5.21 Fe-Mn-Al-C....45

5.22 Fe-Mn-Si-C....46

5.23 Fe-Mn-Mo-C....52

6.0 Discussion....55

6.1 Interfacial Roughness....56

6.2 Interfacial Velocity 57

6.3 Carbon Behaviour 59

6.4 Calculating Excess Area and K_{2nm} 61

6.5 Ternary Segregation Behaviour 64

6.51 Fe-Ni-C.....65

6.52 Fe-Mn-C.....66

6.53 Fe-Mo-C.....66

6.54 Fe-Si-C 67

6.55 Fe-Al-C.....68

6.6 Quaternary.....68

6.61 Fe-Mn-Al-C 69

6.62 Fe-Mn-Mo-C.....70

6.63 Fe-Mn-Si-C.....73

7.0 Modelling Results and Discussion.....77

7.1 Model Parameters 78

7.2 Fe-Si-C 80

7.3 Fe-Mo-C.....83

7.4 Fe-Mn-C.....86

7.5 Quaternary Implications 90

7.51 Fe-Mn-Mo-C 90

7.52 Fe-Mn-Si-C 91

8.0 Conclusions 94

Appendix 1: TEM-EELS Data 96

Appendix 2: The Effect of Element Concentration on Segregation 98

Appendix 3: Fe-Al-C and Fe-Mn-Al-C Modelling Results 100

Appendix 4: Silicon Segregation in an Fe-Mn-Mo-C Sample 102

References 104

List of Figures

Figure 1: Carbon profiles for ferrite precipitation under a) diffusion-control, b) interface-control, and c) mixed mode [1].....3

Figure 2: X and carbon profiles under LE-P conditions [17]. 7

Figure 3: X(Mn) and carbon profiles under LENP conditions [17]. 9

Figure 4: Sample Fe-X-C phase diagram with PE and LENP regions [29]. 11

Figure 5: Fe-Mn-C phase diagram at 1048K.....13

Figure 6: Fe-Al-C phase diagram at 1173K.....13

Figure 7: Fe-Mo-C phase diagram at 1048K.....14

Figure 8: Cahn's approximate solute drag as a function of velocity [30]. 17

Figure 10: X chemical potential profiles at the interface for a) manganese b) molybdenum c) nickel [24,25]. 20

Figure 11: The atomic planes at the interface for the three-jump model [24,25]. 21

Figure 12: Carbon evolution during transformation at 1048K for a) the Fe-Ni-C and b) Fe-Mo-C systems [24,25]. 23

Figure 13: Carbon concentration profile during decarburization experiments. [24,25] ...25

Figure 14: Classical precipitation method (left) and controlled decarburization method (right) [24]. 27

Figure 15: a) A visualisation of field evaporation. b) Potential energy vs distance diagram [41]. 33

Figure 16: Plot illustrating conditions that allow for field evaporation [41]. 34

Figure 17: Cylindrical ROI used to create the profile for an Fe-Mn-Mo-C APT tip. Carbon atoms represented in red. 37

Figure 18: APT profile for Fe-Ni-C diffusion couple, decarburized at 775°C for 120 min..38

Figure 19: APT profile for Fe-Ni-C diffusion couple, decarburized at 775°C for 465 min. (Tip A) 39

Figure 20: APT profile for Fe-Ni-C diffusion couple, decarburized at 775°C for 465 min. (Tip B) 39

Figure 21: APT profile for Fe-Ni-C diffusion couple, decarburized at 775°C for 870 min..40

Figure 22: APT profile for Fe-1.0Al-0.6C alloy decarburized at 900°C for 32 min. 41

Figure 23: APT profile for Fe-1.0Al-0.6C alloy decarburized at 950°C for 64 min. (Tip A).41

Figure 24: APT profile for Fe-1.0Al-0.6C alloy decarburized at 950°C for 64 min. (Tip B).42

Figure 25: APT profile for Fe-1.41Mn-.47C alloy decarburized at 775°C for 18.5 min. OAD (Tip A) 43

Figure 26: APT profile for Fe-1.41Mn-.47C alloy decarburized at 775°C for 18.5 min. (Tip B) 43

Figure 27: APT profile for Fe-.51Mo-.54C alloy decarburized at 775°C for 79 min. 44

Figure 28: APT profiles for Fe-1.61at%Si-3.41at%C alloy decarburized at 775°C for a) 64 min and b) 240 min [42].....44

Figure 29: APT profile for Fe-1.9Mn-1.8Al-0.6C alloy decarburized at 900°C for 17 min. (Tip A) 45

Figure 30: APT profile for Fe-1.9Mn-1.8Al-0.6C alloy decarburized at 900°C for 17 min. (Tip B) 46

Figure 31: APT profile for Fe-94Mn-.94Al-0.6C alloy decarburized at 900°C for 17 min. .46

Figure 32: SEM image of ferrite precipitation in the Fe-1.5Mn-1.3Si-.66C sample.....48

Figure 33: SEM image of ferrite precipitation in the Fe-1.0Mn-0.9Si-.68C sample.....48

Figure 34: APT profile for Fe-1.5Mn-1.3Si-.66C alloy decarburized at 755°C for 240 min. OAD 49

Figure 35: APT profile for Fe-1.0Mn-.9Si-.68C alloy decarburized at 755°C for 240 min. (Tip A) 49

Figure 36: APT profile for Fe-1.0Mn-.9Si-.68C alloy decarburized at 755°C for 240 min. (Tip B) 50

Figure 37: APT profile for Fe-1.5Mn-1.5Si-.67C alloy decarburized at 755°C for 16 min. .50

Figure 38: APT profile for Fe-1.5Mn-1.5Si-.67C alloy decarburized at 755°C for 32 min. (Tip A) 51

Figure 39: APT profile for Fe-1.5Mn-1.5Si-.67C alloy decarburized at 755°C for 32 min. (Tip B) 51

Figure 40: APT profile for Fe-1.5Mn-1.5Si-.67C alloy decarburized at 755°C for 32 min. (Tip C) 52

Figure 41: APT profile for Fe-1.36Mn-.42Mo.48C alloy decarburized at 755°C for 23.5 min. (Tip A) 53

Figure 42: APT profile for Fe-1.36Mn-.42Mo.48C alloy decarburized at 755°C for 23.5 min. (Tip B) 53

Figure 43: APT profile for Fe-1.36Mn-.42Mo.48C alloy decarburized at 755°C for 120 min. (Tip A) 54

Figure 44: APT profile for Fe-1.36Mn-.42Mo.48C alloy decarburized at 755°C for 120 min. OAD (Tip B) 54

Figure 45: APT profile for Fe-1.36Mn-.42Mo.48C alloy decarburized at 755°C for 240 min. (Tip A) 55

Figure 46: APT profile for Fe-1.36Mn-.42Mo.48C alloy decarburized at 755°C for 240 min. (Tip B) 55

Figure 47: TEM image of the ferrite/austenite interface in a duplex stainless steel [43]. 57

Figure 48: Visualization of excess area calculation. 63

Figure 49: Comparison of molybdenum segregation at 23.5 min in tips A and B. 71

Figure 50: Comparison of manganese segregation at 23.5 min in tips A and B. 72

Figure 51: Excess areas of manganese and molybdenum in the Fe-Mn-Mo-C samples. .. 73

Figure 52: Modelling of Fe-.88Si-.58C decarburized at 775°C. 82

Figure 53: Modelling of Fe-.88Si-.58C decarburized at 806°C. 82

Figure 54: Modelling of Fe-.88Si-.58C decarburized at 825°C. 83

Figure 55: Modelling of Fe-.88Si-.58C decarburized at 850°C. 83

Figure 56: Modelling of Fe-.51Mo-.54C decarburized at 775°C. 85

Figure 57: Modelling of Fe-.51Mo-.54C decarburized at 806°C. 85

Figure 58: Modelling of Fe-.51Mo-.54C decarburized at 825°C. 86

Figure 59: Modelling of Fe-.94Mn-.57C decarburized at 755°C. 88

Figure 60: Modelling of Fe-.94Mn-.57C decarburized at 775°C. 88

Figure 61: Modelling of Fe-.94Mn-.57C decarburized at 806°C. 89

Figure 62: Modelling of Fe-.94Mn-.57C decarburized at 825°C. 89

Figure 63: TEM image of the ferrite/austenite interface. 96

Figure 64: EELS map of the interface for manganese (left) and carbon (right). 97

Figure 65: EELS concentration profile across the interface. 97

Figure 66: Visualization of proposed relationship between segregation and concentration. 99

Figure 67: Comparison of the decarburization results for Fe-1.0Al-0.6C at 900°C and the LENP predictions. 101

Figure 68: APT profile of the Fe-1.36Mn-.42Mo.48C alloy decarburized at 755°C for 23.5 min with high silicon. (Tip A) 103

List of Tables

Table 1: Segregation values for ternary APT samples. 68

Table 2: Segregation values for quaternary APT samples. 76

Table 3: Summary of ternary boundary adjustments and resultant effective BEs. 90

1.0 Introduction

For over 100 years, phase transformations in iron alloys have been studied. Even after such a large body of research has been conducted, discoveries are still to be made. One area that has garnered significant interest is the transformation from austenite into ferrite.

The ferrite transformation received attention in part due to its impact on the strength and ductility of the material. Producers have often desired to increase the hardenability of the steel and have searched for alloys that would slow or prevent ferrite from forming. Others have desired a ferritic or dual phase steel and needed to predict the microstructure for a given heat treatment. Whether one wishes to avoid or achieve ferrite, knowledge of the transformation has practical importance.

One of the challenges faced by researchers is quantifying the effect an alloying element has on the transformation. While many ternary systems have been investigated and a few quaternary systems, there still remains a gap between these alloys and the alloys commonly used in industry. For example, 3rd generation steels can often have non-negligible amounts of Mo, Mn, Cr, Al and Si. The purpose of this thesis is to add to the knowledge of the ferrite transformation in ternary and quaternary systems. The focus will be on alloying elements and their interactions with the moving ferrite/austenite interface.

2.0 The Ferrite Phase Transformation

It is prudent to begin with a review of the large body of work done on this transformation. It has been well established that at high temperatures, the austenite to ferrite transformation occurs through reconstructive diffusion [1-4]. It is not a displacive transformation which advances the interface through physical deformation, rather the interface advances through diffusion [1-4]. In the subsequent sections, the possible rate controlling processes for this reconstructive transformation will be discussed, along with the theories on how solute elements redistribute during the transformation.

2.1 Rate Controlling Processes

Reconstructive transformations can be rate controlled by diffusion across the interface (interface-controlled) or diffusion ahead of the interface (diffusion-controlled). The transformation is interface-controlled if the free energy is primarily dissipated by diffusion across the interface [1-4]. The transformation is diffusion-controlled if the free energy is primarily dissipated by diffusion ahead of the interface [1]. Both of these are two extremes of a spectrum and in practice, both the interface and the diffusion ahead of it can have non-negligible effects on the kinetics of the ferrite to austenite transformation [1-4].

Diffusion-controlled growth occurs when the atoms diffusing away from the interface limit the rate of transformation [1-4]. At this extreme, the interfacial processes become an insignificant factor for the transformation kinetics. The mobility of the interface is considered to be sufficiently large so that it will instantly advance once the element has

diffused away from the interface. As the transformation progresses, a spike forms ahead of the interface, the height of which approaches the equilibrium value of $x^{\gamma/\alpha}$ (Figure 1a). The assumption of local equilibrium at the interface is often used when under diffusion-control. Generally, diffusion-controlled growth is faster than the transformation under interface-control in multi-component systems and grows parabolically as a function of time (EQ.1) [1,5]:

$$Z = \alpha t^{0.5} \quad (1)$$

where Z is the ferrite layer thickness, α is the parabolic constant, and t is time. The parabolic constant depends on the concentration gradient and the diffusion coefficient of the diffusing element.

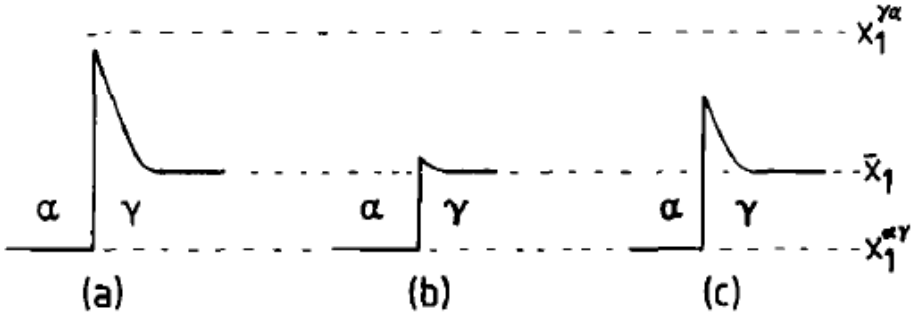

Figure 1: Carbon profiles for ferrite precipitation under a) diffusion-control, b) interface-control, and c) mixed mode [1].

The interface-controlled growth differs from the diffusion-controlled growth. The velocity of the interface can be modelled as a function of interface mobility (M) and the concentration difference in the austenite (EQ.2) [1,2].

$$\nu = \mathrm{M} \cdot (C_2 - C_1) \qquad (2)$$

C_2 is the carbon concentration at the austenite side of the interface and C_1 is approximately equal to the bulk carbon concentration in the austenite. The difficulty in modelling interface-controlled growth is that M is intrinsic to the interface and can only be found empirically [1]. The composition at the austenite side of the interface should be close to the bulk value at the onset of transformation (Figure 1b). Unlike the diffusion-controlled growth, the interface concentration does not begin near the equilibrium value, but as the transformation progress, the concentration approaches the equilibrium value. The common assumption that the interface experiences a local equilibrium would be invalid if the transformation is near interface-control.

The mixed-mode growth is not completely controlled by diffusion across or ahead of the interface. Though all diffusional transformations are technically mixed-mode, this often refers to transformations where they are not close enough to either extreme to reasonably select one [1]. The concentration profile is not shallow like that under interface-control, but it does not reach the equilibrium concentration at the onset of growth that diffusion-controlled growth attains (Figure 1c). Modelling growth in this way often includes a flux term from the partial element spike and using a finite interface mobility that also limits the kinetics [1].

This section is based on carbon that needs to diffuse away from the growing ferrite for interface motion to occur. The following section will discuss the theories for when substitutional solutes are present in the alloy. Unlike carbon, these elements may or may not need to redistribute to allow for isothermal ferrite growth.

2.2 Element Redistribution During Transformation

There have been varying opinions on how elements redistribute during the austenite to ferrite transformation. In the binary Fe-C system, several authors assumed diffusion-controlled growth and that the interface remains in chemical equilibrium [6-10]. They were able to accurately model the Fe-C system through these assumptions. As carbon is a fast diffuser it is a reasonable assumption that it would be in equilibrium at the interface. For precipitation, the ferrite would grow at its equilibrium composition and would cease when austenite reaches its equilibrium carbon content.

When the iron alloy includes substitutional elements, the system grows in complexity. Several different assumptions have been made over the years to account for the behaviour of substitutional elements during the ferrite transformation. In the simple ternary case, the alloy takes the form of Fe-X-C where X is the substitutional element. Modellers have often assumed that X and carbon are either in local equilibrium [11-16] or in Paraequilibrium (PE) while the ferrite grows into the parent austenite.

Local equilibrium at the interface assumes that all elements are in chemical equilibrium (EQ.3):

$$\begin{cases} \mu_C^{\alpha} = \mu_C^{\gamma} \\ \mu_{Fe}^{\alpha} = \mu_{Fe}^{\gamma} \\ \mu_X^{\alpha} = \mu_X^{\gamma} \end{cases} \quad (3)$$

An appropriate tie-line must be selected such that conservation of mass is maintained. The simplified mass balance equations for the moving interface are as follows (EQ.4,5) [1]:

$$v\left(X_C^{\gamma\alpha} - X_C^{\alpha\gamma}\right) = -D_C \frac{\partial X_C}{\partial z} \quad (4)$$

$$v\left(X_X^{\gamma\alpha} - X_X^{\alpha\gamma}\right) = -D_X \frac{\partial X_X}{\partial z} \quad (5)$$

Where v is the velocity of the interface, $X_i^{\gamma\alpha}$ is the mole fraction of the element at the austenite side of the interface, and $X_i^{\alpha\gamma}$ is the mole fraction of the element at the ferrite side of the interface. The challenge in determining the tie-line is that carbon has a significantly higher diffusivity than the X elements due to the interstitial diffusion of carbon. As $D_C >>> D_X$, the concentration gradients and interfacial contact conditions must compensate so that both EQ.4 and EQ.5 are satisfied. Depending on where the composition lies in the α+γ phase field, the X element will either partition or have negligible partitioning. Two modes of growth stems from this behaviour: local equilibrium-partitioning (LE-P) and local equilibrium-negligible partitioning (LENP). The zero-partition line separates the region where LE-P and LENP [12] (Figure 2). Below the zero-partition line, LENP conditions should exist during growth, while above the line LE-P

conditions should be present during growth. The kinetics and solute redistribution during ferrite growth under LE-P and LENP conditions will be subsequently detailed.

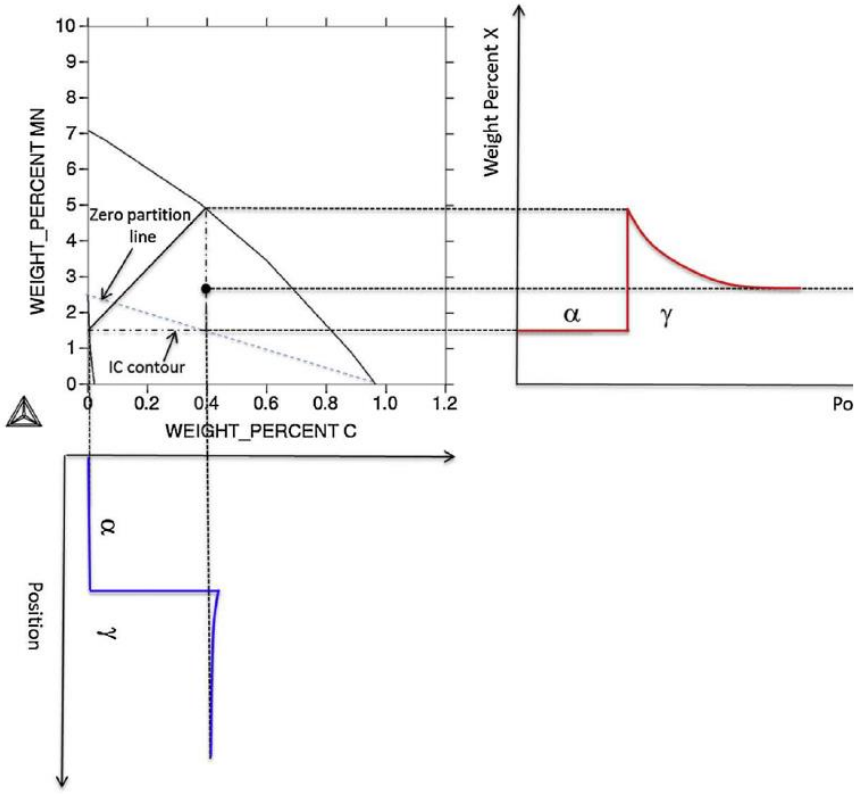

Figure 2: X and carbon profiles under LE-P conditions [17].

LE-P solves the mass conservation equations by allowing X to partition and keeping the carbon gradient exceedingly low to compensate for the higher diffusivity (Figure 2). For this example with manganese, both the ferrite and austenite manganese concentrations differ from the bulk composition. Extremely slow growth in comparison to the binary Fe-C system is characteristic of LE-P. LE-P growth is rate-controlled by the partitioning of X rather than carbon diffusion.

Alternatively, LENP solves the mass conservation equations by allowing for a thin X element spike at the austenite side of the interface (Figure 3) [11]. The spike has a sufficiently high concentration gradient to offset the unbalanced diffusion coefficients. The X element does not necessarily need to partition for ferrite growth [11,12]. Below the zero-partition line, ferrite would still lower the free energy of the system if X does not partition (Figure 3). As X negligibly partitions, the transformation is no longer rate-controlled by the diffusion of X. This leads to significantly higher kinetics than that of LE-P. The price of the higher kinetics is solute or solvent trapping within the ferrite [18]. Though solute (X) or solvent (Fe) atoms have a chemical driving force to leave the ferrite, it is kinetically unfavourable and are trapped.

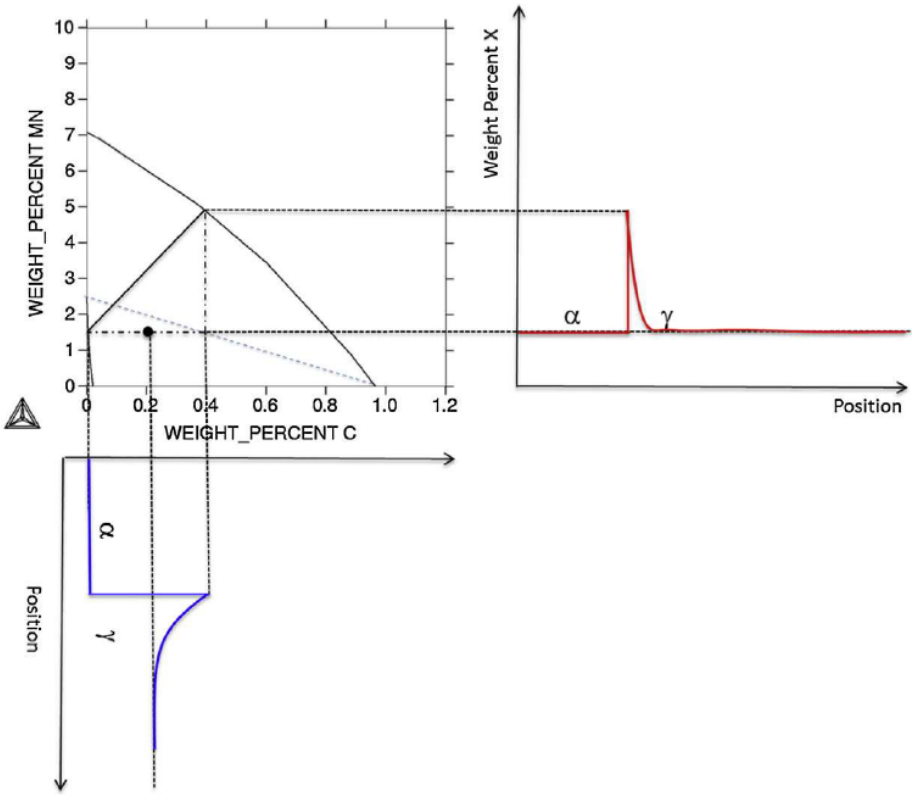

Figure 3: X(Mn) and carbon profiles under LENP conditions [17].

One critique of the LENP assumption is the feasibility of the X spike. The width of the X element spike can be approximated to (EQ.6) [19]:

$$w = \frac{2D_X^\gamma}{v} \qquad (6)$$

where v is the velocity of the interface and D_X^γ is the diffusion coefficient of X in austenite. D_X^γ is often much smaller in magnitude than v, leading to a calculated width that can be less than an atomic distance [19]. Coates suggested that for the spike to be stable, w would need to be greater than five nanometers [16]. For this reason, Hillert concluded that deviations from local equilibrium must occur if the width of the spike approaches

atomic dimensions [20]. However, the LENP assumption has been used to successfully model alloys within the Fe-Ni-C [21,22] and Fe-Mn-C systems [23-25]. This has led some to use LENP but to use an atomistic model rather than a continuum model [24-26].

The previous conditions were based on the local equilibrium assumption at the interface. Local equilibrium is not necessary for ferrite growth, the Paraequilibrium assumption may also be utilized. The PE assumption is that only carbon is in equilibrium at the interface. This was put forward by Hultgren [27] and further developed by Hillert [28]. Under PE conditions, carbon has a uniform chemical potential across the interface while iron and X suffer a chemical potential difference (EQ.7) [27,28].

$$\begin{cases} \mu_C^{\alpha} = \mu_C^{\gamma} \\ X_X\left(\mu_X^{\gamma} - \mu_X^{\alpha}\right) = X_{Fe}\left(\mu_{Fe}^{\gamma} - \mu_{Fe}^{\alpha}\right) \end{cases} \quad (7)$$

The reasoning behind PE is that the iron and X atoms have a much lower diffusivity than carbon and are assumed to remain stationary during the transformation. Unlike the LE-P and LENP, PE has differing ferrite and austenite phase boundaries that lie within the two-phase region (Figure 4). The PE phase boundaries are constructed from the carbon component rays from the ternary isothermal phase diagram [27,28]. Authors stressed that the PE region is purely based on thermodynamic calculations and may or may not be realized in practice [27,28].

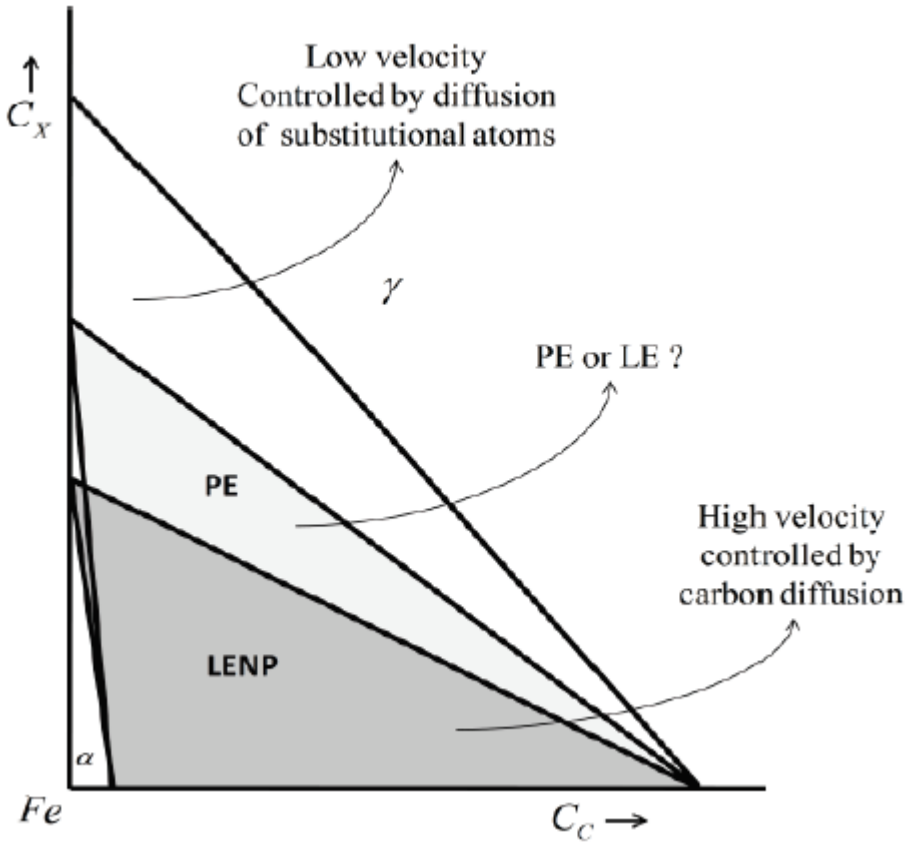

Figure 4: Sample Fe-X-C phase diagram with PE and LENP regions [29].

The PE and local equilibrium conditions can offer quite different kinetic predictions. They are in agreement that slow, partitioning growth occurs above the PE boundary. Below the envelope of zero partitioning, both predict a faster growth governed by carbon diffusion. PE predicts slightly higher kinetics in this region because of the difference in carbon interfacial concentrations. The major discrepancy between PE and local equilibrium lies in the PE region that is above the zero-partitioning line. Local equilibrium predicts slow partitioning growth according to LE-P while PE still predicts high kinetics.

Phillion et al.'s work with the Fe-Ni diffusion couple would suggest that ferrite can form in the PE only region, but the kinetics are much slower than what PE predicts [21].

The transformation is not necessarily constrained to a single interfacial condition throughout its entirety. Several authors have suggested that PE conditions could play a role in the nucleation and early growth conditions [26,29,28]. These conditions would then transition to LENP or LE-P as the transformation progresses.

Experimental data has shown that growth kinetics can be predicted by using PE or LENP conditions for certain alloys. However, there are many compositions and temperature conditions that cannot be fully explained by PE or LENP. This is especially true of alloys lying within the LENP region that have markedly slower kinetics than what LENP predicts. One possible cause for this discrepancy is the influence of X on the moving interface.

2.3 Effects of Alloying Elements

2.31 Thermodynamic Contribution

One of the most influential effects an element can have on the ferrite phase transformation is altering the thermodynamic stabilities of the two phases. Though the later discussed energy dissipation may slow the transformation, altering the relative stabilities can prevent the transformation from ever beginning. Substitutional elements may increase the austenite stability or the ferrite stability or have a negligible impact on the two phases. Isothermal phase diagrams with tie lines have been made in Thermo-Calc

for the Fe-Mn-C system at 1048K (Figure 5), the Fe-Al-C system at 1173K (Figure 6), and the Fe-Mo-C system at 1048K(Figure 7).

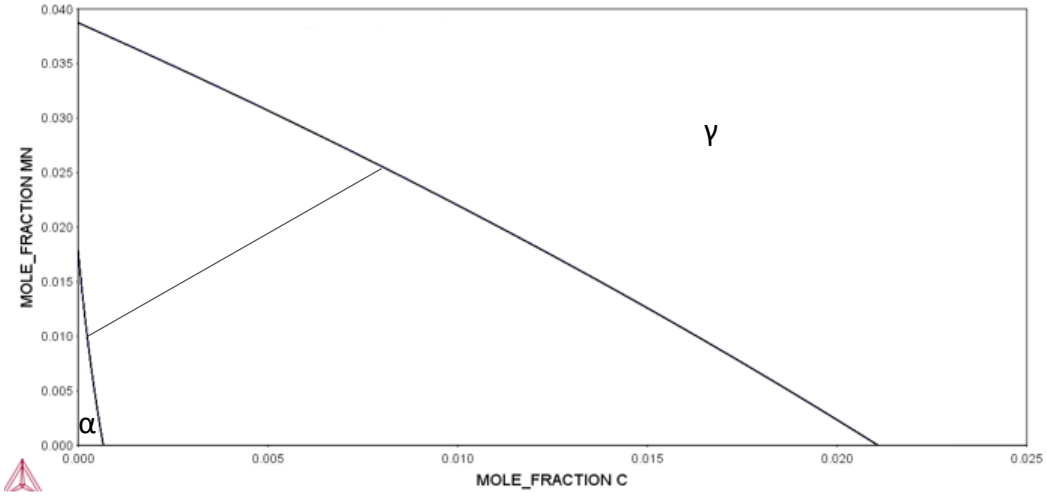

Figure 5: Fe-Mn-C phase diagram at 1048K

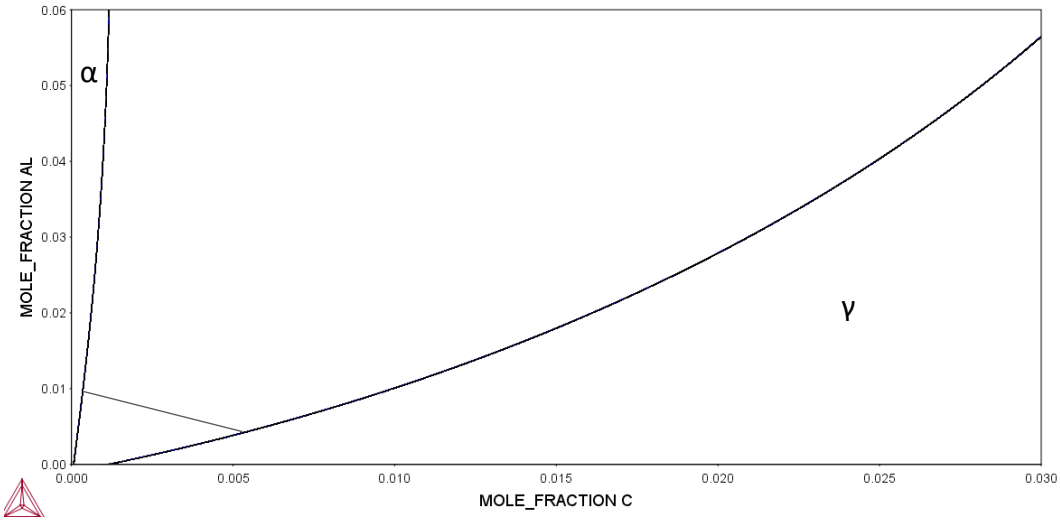

Figure 6: Fe-Al-C phase diagram at 1173K

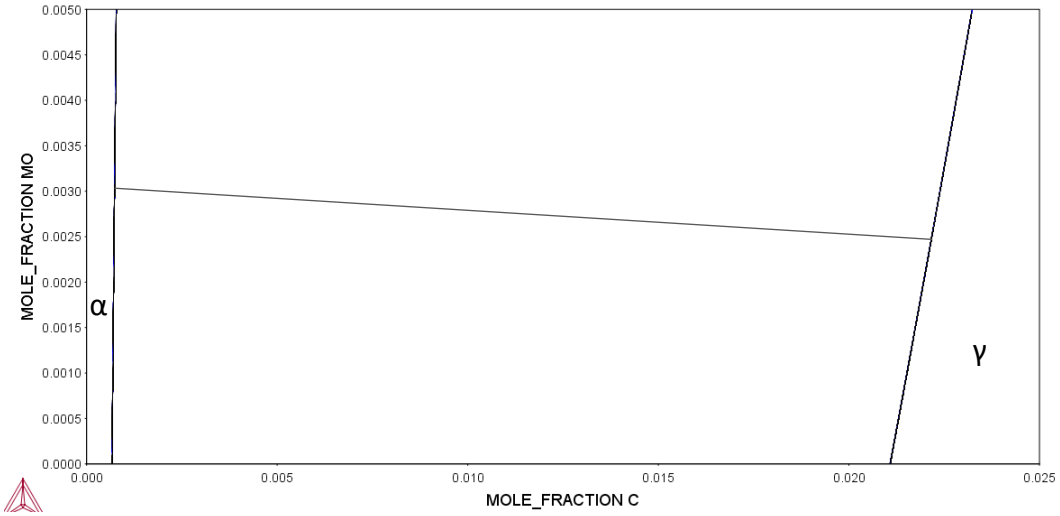

Figure 7: Fe-Mo-C phase diagram at 1048K

Manganese is an austenite stabilizer while aluminum is a ferrite stabilizer. At 1048K, molybdenum is a weak ferrite stabilizer and does not significantly influence the phase diagram. Changing the manganese concentration can prevent the ferrite from forming by moving the alloy into the austenite phase field. A shift in manganese could also move the alloy from the envelope of zero partitioning to the partitioning region. By simply adjusting the manganese content, the transformation kinetics can go from non-existent to an extremely slow partitioning transformation to a relatively fast non-partitioning transformation.

Under controlled decarburization experiments, the flux of carbon within the ferrite allows for ferrite growth to occur. This flux can be significantly affected by the carbon solubility in the ferrite, as flux is directly proportional to the concentration gradient as stated in

Fick's first law. Therefore, all else being equal, the ferrite kinetics should increase with increasing carbon solubility in the ferrite.

A major limitation to early efforts of predicting ferrite growth was inadequate thermodynamic information. The inaccurate thermodynamic descriptions would lead to inaccurate carbon conditions, which in turn would lead to inaccurate kinetic predictions. For example, if carbon solubility in ferrite is overstated due to inaccurate thermodynamic descriptions, LENP and PE kinetic predictions would also be overstated. Accurate thermodynamic descriptions are the foundations for analyzing the effects that alloying elements have on growth kinetics. They determine the LENP and PE predictions. Further analysis and modelling is based on how the experimental data compares to these predictions. If these kinetic predictions were overstated, it would lead to the errant conclusion that the element has a significant retarding effect on the transformation.

If altering the phase diagram is the only effect a substitutional element has on the kinetics of ferrite growth, this would be relatively simple to model. Equilibrium conditions can be computed in programs such as Thermo-Calc to allow for modelling with conditions such as LENP or PE. As previously mentioned, these conditions cannot fully predict the transformation kinetics. Perfect thermodynamic information may not be able to harmonize the data with predictions. This would suggest other effects that X may have on the transformation.

2.32 Energy Dissipation

For decades it has been known that even dilute solute concentrations can slow the movement of grain boundaries [30-32]. Lucke and Detert proposed a solute drag force at the grain boundaries [31] and the theory was later improved on by Cahn and then by Lucke and Stuwe [30,32]. They proposed that the solutes have an affinity toward the grain boundaries and that as a boundary moves, the solute atoms exert a retarding force. Cahn developed the equation below for the solute drag force P (EQ.8) [30]:

$$P = \frac{\alpha v C_0}{1 + \beta^2 v^2} \qquad (8)$$

where

$$\frac{\alpha}{\beta^2} = \frac{N}{kT} \int_{-\infty}^{+\infty} \left(\frac{\partial E}{\partial x}\right)^2 D_X(x)\, dx \qquad (9)$$

v is the velocity of the interface, C_0 is the bulk solute concentration, N is the solute atoms at the interface per unit volume, D_X is the diffusion coefficient for the substitutional element, and E is the interaction energy of the solute with the interface. Cahn showed that the that the sign of E did not influence the solute drag. The solutes attracted to the boundary would drag behind it while the repelled solutes would be pushed ahead of the boundary. The solute drag was plotted as a function of velocity (**Error! Reference source not found.**). It was shown to be low at both low and high velocities, with a maximum at some intermediate velocity. If the overall driving force is low, the solute drag would make

intermediate velocities unattainable, allowing for a discontinuous jump from high to low velocity regions [30]. The difficulty with calculating solute drag at that time was that quantities in EQ.9 were not accurately known. Though solute segregation at boundaries could be detected, an accurate quantity could not be obtained. Sufficiently accurate diffusion coefficients were also unknown and the trans-interfacial diffusion coefficient for substitutional elements remains uncertain to this day. The last significant unknown was the energy profile across the interface for X. Cahn used a wedge profile, but this was simply done to perform the sample calculations.

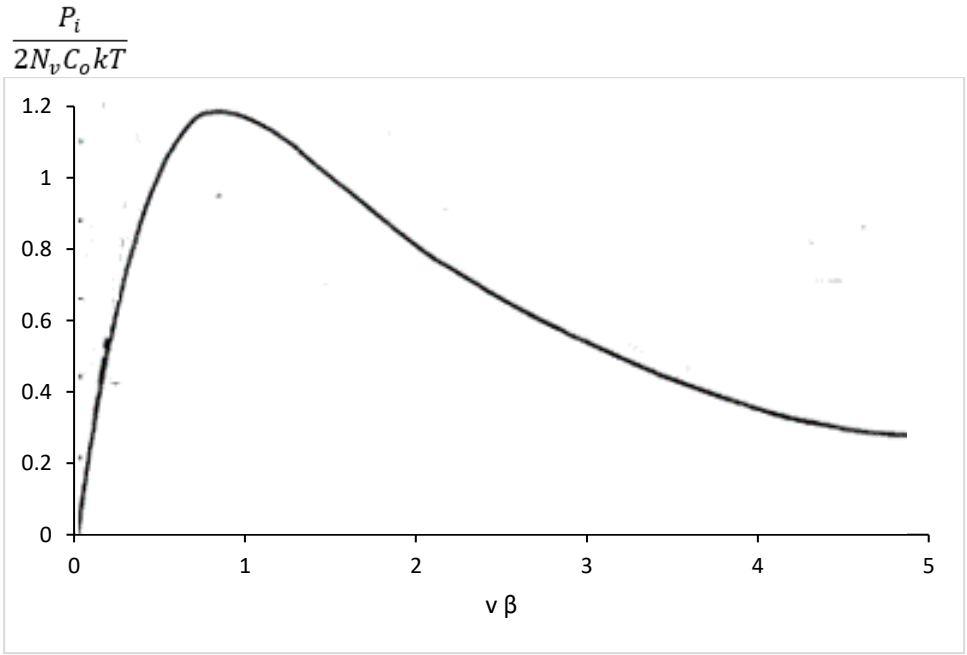

Figure 8: Cahn's approximate solute drag as a function of velocity [30].

Hillert took a different approach from the previous force-based models [33]. He instead developed an energy dissipation model. While Cahn considered a force balance, Hillert used free energy to calculate the free energy dissipation and arrived at similar results. This free energy dissipation would lower the driving force and the transformation kinetics. For the binary system, Hillert and Sundman calculated the rate of free energy dissipated using EQ.10 [34]:

$$\frac{dG}{dt} = -\int_V J_B \frac{d(G_B - G_A)}{dy} dV \qquad (10)$$

During steady state, they assumed the energy dissipation (P) would be (EQ.11):

$$P = \left(\frac{dG}{dt}\right)\frac{\Delta t}{V_m} \qquad (11)$$

Plugging in EQ.10 to EQ.11 gives the energy dissipation as (EQ.12):

$$P = -\frac{1}{v}\int_{-\infty}^{+\infty} J_B \frac{d(G_B - G_A)}{dy} dy \qquad (12)$$

They showed that under certain conditions, the energy dissipation can conform to Cahn's force-based model [19,34]. One key distinction between the two models is the $\left(\frac{\partial E}{\partial x}\right)$ force term being replaced by the free energy dissipation term. Though Cahn's approach was designed for the movement of grain boundaries, Hillert extended his energy approach to phase transformations as well. Hillert later critiqued the early force-based models, showing that there would be significant difficulty in using them for phase transformations

[35]. However, Purdy and Brechet were able to extend Cahn's approach to phase transformations [36-38].

Reducing unknowns within the solute dissipation models could increase their effectiveness in modelling ferrite growth. Notable unknowns include: the binding energy of a solute to the interface and co-segregation effects at the interface. The magnitude and profile of the binding energy can have significant effects on the solute dissipation calculations [30,33]. Finding the quantitative segregation of various solutes could be used to reduce the binding energy unknown. Comparing ternary and quaternary segregation data could also shed light on co-segregation behavior. Reducing these unknowns is the purpose for the experimental work of this thesis.

3.0 Summary of the Three-Jump-Model

The model that this thesis uses is the three-jump-model developed by Zurob et al. [24,25]. This model was influenced by the work of Odqvist et al. and Hutchinson et al. [22,26]. The following is a summary of the model detailed in the paper by Zurob et al. and the thesis of Daman Panahi [24,25]. This model has three main components: substitutional element diffusion across the interface, the interaction of carbon at the interface, and carbon diffusion in the bulk phases. All of these components are used to predict ferrite growth over a range of temperatures and compositions.

3.1 Substitutional Element Diffusion

The model incorporates the assumption that PE conditions exist during nucleation and early growth. After this short time, the conditions would begin to transition to LENP. Once the condition has departed from PE, X is then free to diffuse in response to the chemical potential differences that exist (Figure 9).

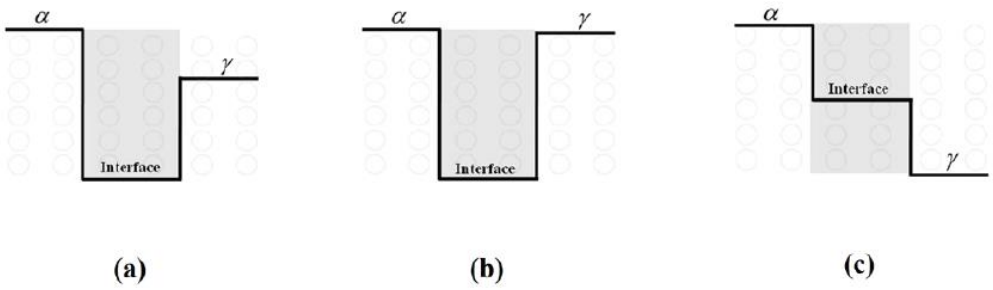

Figure 9: X chemical potential profiles at the interface for a) manganese b) molybdenum c) nickel [24,25].

There are three main ways that X may view the interfacial region. The first (Figure 9a) is when X has a significant attraction/repulsion to the interface and a difference exists with the chemical potentials of ferrite and austenite. One example of this is the Fe-Mn-C system. Manganese has an attraction to the interface and would also prefer to diffuse from the ferrite into the austenite in order to balance the chemical potentials. The second (Figure 9b) is when X has a significant attraction/repulsion to the interface and an insignificant difference in the chemical potentials of the two phases. This is can be true in the Fe-Mo-C system for certain conditions. Molybdenum has a strong attraction toward the interface, but it has an insignificant driving force to diffuse into austenite or ferrite. The last (Figure 9c) is when X does not have a significant attraction/repulsion to the

interface but there does exist a chemical potential difference between the two phases. Nickel has shown a negligible affinity towards the interface, but it would prefer to diffuse from ferrite to austenite because of the chemical potential difference.

A discrete three-jump model is used for X element diffusion (Figure 10). Substitutional elements take three jumps to cross the interface from one phase to the other. Each jump has a unique diffusion coefficient (D_i) and flux (J_i). D_1 and D_3 are the diffusion coefficients for element X in ferrite and austenite respectively. The values are taken from DICTRA, using the MOB2 database. D_2 is simply the geometric average of D_1 and D_3.

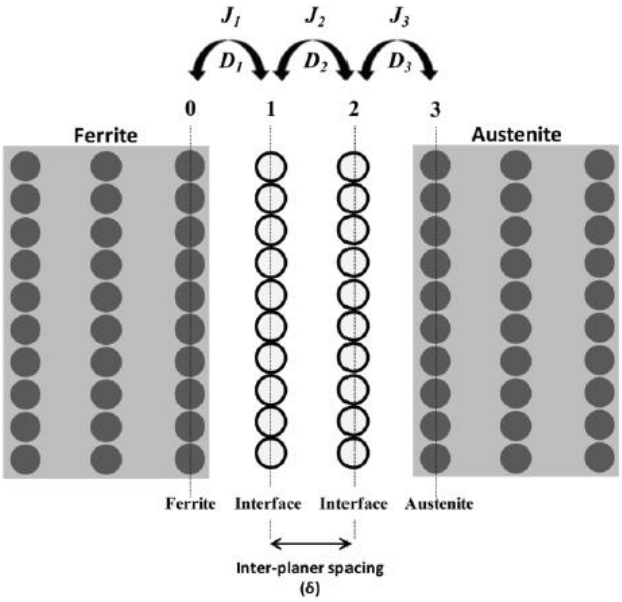

Figure 10: The atomic planes at the interface for the three-jump model [24,25].

The jumps that X atoms take are incorporated into the energy dissipation calculations. This dissipation is calculated using an equation proposed by Hillert and Sundman for discrete-jumps (EQ.13) [34]:

$$\Delta G^{dis} = \sum_{i=1}^{3} -\frac{V_m}{\nu} J_X^i \left[\left(\mu_X^i - \mu_X^{i-1} \right) - \left(\mu_{Fe}^i - \mu_{Fe}^{i-1} \right) \right] \quad (13)$$

This allows for the energy dissipation to be computed for a given velocity. The model obtains the chemical potentials using a modified version of the TCFE2 database in Thermo-Calc. There is no boundary phase in Thermo-Calc and so modifications are necessary. A boundary phase was created in Thermo-Calc in order to carry out the calculations. The data used for the boundary phase is nearly identical to the austenite phase. The differences are the modifications to account for the binding energies to the interface and corrections to account for surface energy. The energy dissipation is subsequently used to calculate the carbon concentration at the interface.

3.2 Carbon Concentration at the Interface

The carbon content at the interface is calculated based on two major assumptions as outlined by Zurob et al. [25]. The first assumption is that carbon has the same chemical potential across the interface. The rationale for this is that carbon has a sufficiently high diffusivity at the temperatures of interest. The second assumption is that the chemical driving force for interface motion is dissipated by the frictional and diffusional processes (EQ.14):

$$D_{int}^{chem} + \Delta G^{friction} + \Delta G^{diff} = 0 \quad (14)$$

$\Delta G^{friction}$ is assumed to be negligible at the temperatures of interest. ΔG^{diff} is the energy dissipation term from X that is taken from discrete-jump equation (EQ.13)

proposed by Hillert and Sundman. D_{int}^{chem} is the chemical driving force at the interface taken from Hutchinson et al. [22] and is given by (EQ.15):

$$D_{int}^{chem} = \frac{\left(U_X^{fcc} + U_X^{bcc}\right)}{2}\left(\mu_X^{fcc} - \mu_X^{bcc}\right) + \frac{\left(U_{Fe}^{fcc} + U_{Fe}^{bcc}\right)}{2}\left(\mu_{Fe}^{fcc} - \mu_{Fe}^{bcc}\right) \quad (15)$$

The energy balance (EQ.14) and the assumption that carbon has a uniform chemical potential across the interface allows for the calculation of the carbon content at the interface. As energy is dissipated the carbon concentration instantly adjusts. The interfacial concentrations are therefore functions of velocity and evolves as the transformation progresses. Two examples of how carbon evolves at the austenite side of the interface are provided (Figure 11). The transformation is set to PE conditions and transitions to LENP over time. Both the Fe-Ni-C (Figure 11a) and Fe-Mo-C (Figure 11b) were simulated at 1048K.

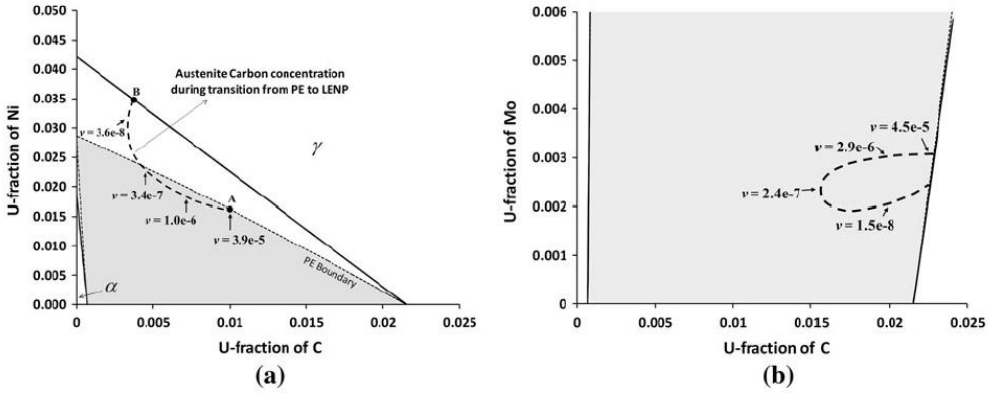

Figure 11: Carbon evolution during transformation at 1048K for a) the Fe-Ni-C and b) Fe-Mo-C systems [24,25].

Though Fe-Ni-C shows an unsurprising path from PE to LENP, Fe-Mo-C is not intuitive. The PE and LENP conditions are not significantly different from each other for Fe-Mo-C, yet

the carbon desegregates to a greater extent at intermediate velocities. This complexity is due to the dissipation at the interface during the transformation. As energy dissipation is at a maximum at intermediate velocities, so the carbon content at the austenite side of the interface decreases to lower the chemical driving force for the transformation. Thus the carbon content is used to maintain the energy balance (EQ.14).

3.3 Bulk Carbon Diffusion

Determining the diffusion of carbon in the bulk phases is essential to modelling ferrite growth. The carbon fluxes are required to calculate the velocity of the interface. Decarburized growth must take into account diffusion in both the ferrite and the austenite, while precipitation is only concerned with the austenite phase. The austenite is assumed to be semi-infinite, which is a reasonable assumption for a sufficiently large sample and short decarburizing times. The model employs the Murry-Landis explicit finite-difference method [39] for diffusion in both phases and accounts for the carbon concentration dependence for carbon diffusion in the austenite. The expected carbon profile should resemble an error function distribution in the austenite, while the shape in the ferrite would depend on the relative fluxes at the surface and the interface (Figure 12). The shape of ferrite carbon profile is generally considered to resemble an error function or a straight line. Once the interfacial conditions have been calculated, the error function approximation can be used to calculate the carbon fluxes.

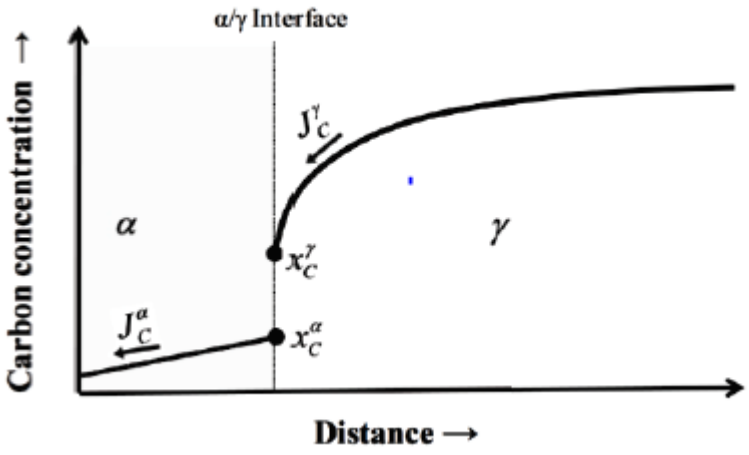

Figure 12: Carbon concentration profile during decarburization experiments. [24,25]

3.4 Growth Rate

The previous three areas of the model are used to calculate the growth rate of ferrite. The energy dissipation caused by the substitutional elements can have a significant effect on the carbon concentrations at the interface. These carbon concentrations are then used to determine the carbon fluxes at each side of the interface. The instantaneous velocity of the interface is calculated by solving the mass balance at the interface. For decarburization, the interface velocity can be represented by the following equation (EQ.16):

$$v = \frac{J_C^\alpha - J_C^\gamma}{X_C^\alpha - X_C^\gamma} \qquad (16)$$

where J_C^α is the carbon flux away from the interface and into the ferrite, J_C^γ is the carbon flux from the austenite to the interface. X_C^α and X_C^γ are the interfacial contact compositions of carbon for ferrite and austenite respectively.

4.0 Experimental Method

Controlled decarburization experiments and atom probe tomography of the subsequently formed interfaces were conducted to improve the modelling of the ferrite transformation. Controlled decarburization experiments provide kinetic data to evaluate the model. Atom probe tomography provides evidence to the behaviour of alloying elements at the interface. The observed behaviour can be subsequently used to improve the energy dissipation calculations within the model. A background for both experiments is given, along with a description of the methods employed.

4.1 Controlled Decarburization Review

Controlled decarburization experiments were performed on ternary and quaternary iron alloy systems. Decarburization experiments require the alloy to have enough carbon to be in the austenite region at the selected temperature (Figure 13). As the carbon is removed, ferrite nucleates at the surface and proceeds to grow inwards as a planar front.

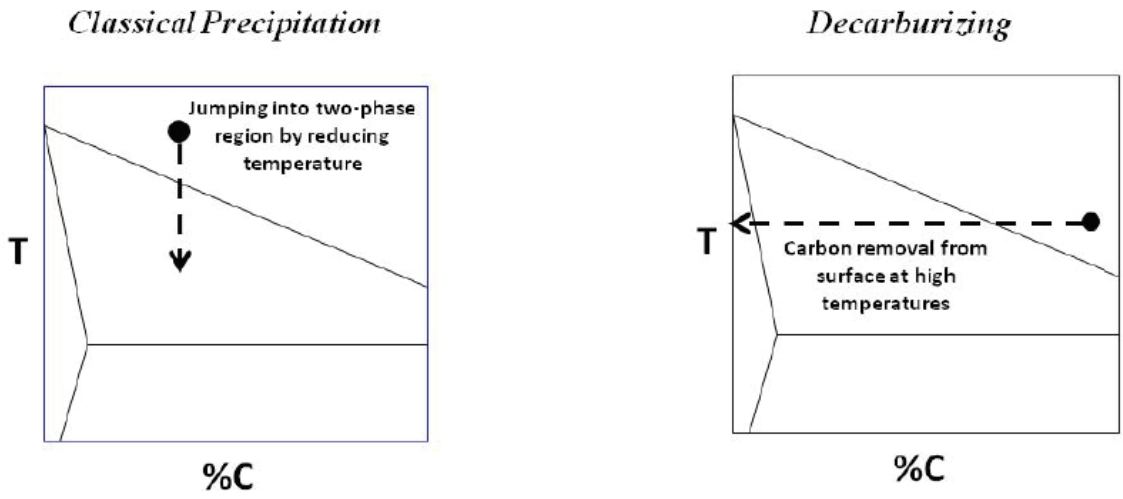

Figure 13: Classical precipitation method (left) and controlled decarburization method (right) [24].

Classical precipitation experiments involve austenitizing the sample at an elevated temperature and then dropping the temperature to place the alloy in the ferrite-austenite region (Figure 13). The ferrite precipitates tend to form on austenite grain boundaries and grow into the grains.

Controlled decarburization was selected over precipitation for several reasons. The first and foremost reason is that the focus of the research is on the interface. The orientation of austenite grains may have a substantial effect on the growing ferrite. The quasi-planar ferrite interface would have consumed several austenite grains of varying orientations during decarburization. This may limit the orientation effect at high and intermediate velocities. Next, the velocity of a decarburized interface has the potential to be calculated, unlike interfaces with during precipitation experiments. A precipitate may have been in a state of fast or slow growth before it was quenched but with a series of decarburization

times, the velocity at a given time can be approximated. The velocity can be calculated by taking the derivative of equation 1 with respect to time. If velocity has an impact on the interface, decarburization is more effective at controlling the variable. However, the velocity of an interface formed by decarburization cannot be calculated with complete certainty. The purging step and subsequent quench could facilitate interface motion and alter the velocity. Purging should eliminate the driving force for ferrite growth and slow the interface. A slow quench allows for ferrite growth as the decrease in temperature increases the driving force. One last reason for utilizing decarburization experiments is that it allows for one dimensional growth. If the sample is investigated far enough from the surface, it can be assumed that the interface is perpendicular to the growth direction and that grew through one dimensional diffusion. For precipitation experiments, three-dimensional growth occurs and there may be overlapping diffusion profiles. During optical and electron microscopy the researcher would only observe the sample in two dimensions and would be unaware of the microstructure below the surface or the microstructure removed from above, both of which could have influenced the growth of the precipitate.

Decarburization also has disadvantages that will need to be taken into account while interpreting the results. One issue is that there is some uncertainty as to when the decarburization effectively begins and ends. This is determined by the wet H_2 flow. Decarburization times are reported by when the flow begins and ends, but the atmosphere may not be fully decarburizing at the onset of flow. It may still decarburize at the onset of the argon purge. Data would need error bars to account for this uncertainty,

but it would still make short time samples unreliable. This method is more suited for intermediate to long decarburization times to limit the influence of this uncertainty. Another issue is surface oxidation of alloying elements. Even in a wet H_2 atmosphere, certain X elements like aluminum and silicon could potentially oxidize at the surface. This may have an effect on decarburization conditions at the surface and on initial nucleation. This can be limited by polishing the surface and plating iron on to it. Polishing removes previous formed oxide, along with surface impurities that could delay decarburization. Plating a few microns of pure iron may protect vulnerable X elements from oxidizing by providing a barrier between the atmosphere and the alloy.

Decarburization experiments were conducted on various homogeneous alloys. The purpose of these experiments was to measure ferrite growth as a function of decarburization time and to provide suitable interfaces to study segregation through APT. Decarburization experiments for an Fe-Ni diffusion couple were also conducted. The purpose of these experiments was to investigate the effects of nickel on the moving boundary and whether or not a full LENP spike forms during the transformation.

4.2 Creation of Alloys

4.21 Fe-Ni-C Diffusion Couple

Creating the diffusion couple began with the making of two Fe-Ni ingots through arc-melting high purity stocks. The two ingots had nickel concentrations of one and five wt%. The ingots were subsequently homogenized and hot-rolled. Next, the ingots were

diffusion-bonded at 900°C in forming gas (95% Ar, 5% H_2). The couple was then cut with a precision cutter into 2 mm thick slices. The slices were then homogenized at 1400°C for two days in a forming gas atmosphere, under a vacuum. This homogenization was to allow for a wide and shallow nickel concentration profile. After homogenization, the slices were cut into 2 mm wide rectangular prisms. The samples were later carburized in a 95:1 CO/CO_2 atmosphere at 1100°C for 36 hours. The ratio was calculated in Thermo-Calc and the target carbon concentration was approximately 0.45 wt%. This carbon concentration was confirmed through combustion analysis and the nickel concentration at either end was confirmed by Inductively coupled plasma (ICP) and Glow Discharge Optical Emission Spectroscopy (GDOES).

4.22 Ternary and Quaternary Alloys

The ternary and quaternary alloys used in this thesis were created through arc melting high purity stocks. Several alloys were made at collaborating universities while a few were made at McMaster university. These alloys were made into finger ingots. The ingots were vacuum sealed in quartz tubes and then homogenized for three days at 1200°C. After homogenization, the ingots were hot-rolled in a rolling mill to approximately 15% reduction. ICP and combustion analysis were used to verify the alloy compositions. The samples were cut with a precision cutter into 2-3 mm thick slices.

4.3 Decarburization

Various ternary and quaternary samples underwent isothermal controlled decarburization in tube furnaces. The samples were polished at the surface to remove any oxide or impurities. They were subsequently spot-welded with nichrome or steel wire to allow for quick extraction from the furnace. Temperature of the furnace was always verified by using K or R-type thermocouples. Samples were inserted into the furnace with an argon atmosphere. The alloys were held for five minutes to allow for austenization. After austenization, wet H_2 was used to decarburize the samples. Ultra-high purity H_2 was passed through water at room temperature to produce the wet H_2. After the decarburization was completed, the tube was purged with argon for four minutes. The samples were then quickly extracted and quenched in water.

The diffusion couple had a different procedure from the other alloys. Decarburization experiments took place in a vertical tube furnace instead of the horizontal set-up. This allowed for a direct quench in water and did not undergo an argon purge. Each sample had two decarburizations instead of one. The first decarburization was for five minutes to find where the ferrite stops forming along the nickel gradient. To observe this, the samples were mounted, polished, and etched with Nital. The 1 wt% Ni side was removed except for 100 µm from where the ferrite stopped. Samples were then decarburized again for various times, ranging from one hour to 14.5 hours.

4.4 Atom Probe Tomography

APT has been used extensively in this work to investigate interfacial solute segregation. Although Electron Energy Loss Spectroscopy (EELS), Energy Dispersive Spectroscopy (EDS), and Electron Probe MicroAnalysis (EPMA) are also popular methods, APT appears to give superior semi-quantitative results for the thin interface region. The mechanisms that allow for APT will be briefly reviewed, along with standard practices, resolution capabilities, and possible errors and/or artifacts that can be present in APT results.

4.41 Review of Technique

This review comes from the information provided by Miller and Gault's books on the subject [40,41]. A rudimentary understanding of APT will be an aid in interpreting the results.

Field evaporation of atoms is the essential process behind APT [40,41]. Atoms at the surface of a specimen can be ionised and desorbed from the surface in the presence of a sufficiently strong electric field [40,41]. The exact mechanism for field evaporation has yet to be verified [41]. However, it is generally accepted that there exists an energy barrier for ionization that is significantly lower in an electric field (Figure 14). The energy barrier is then overcome through thermal activation [41].

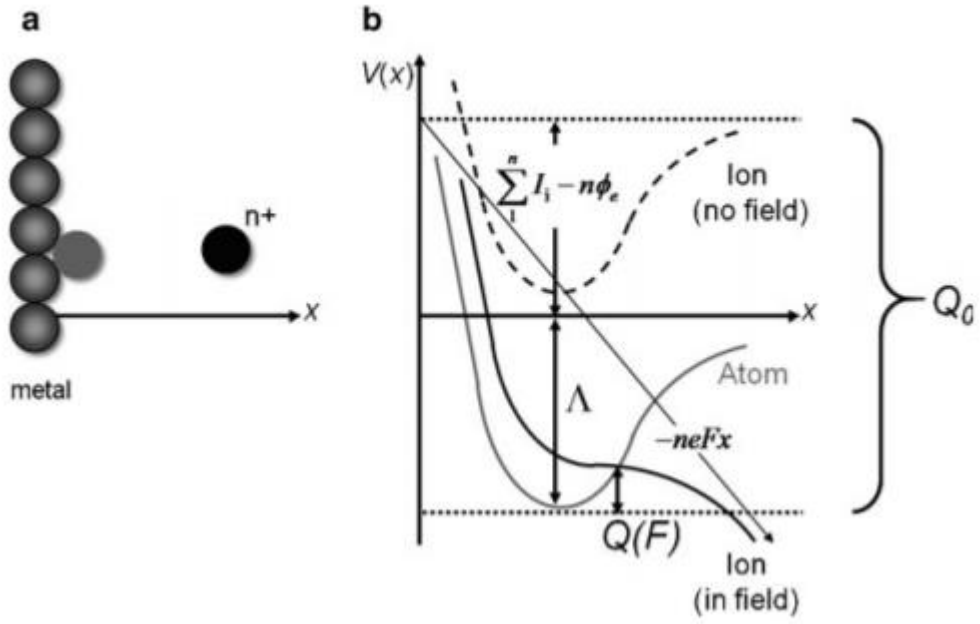

Figure 14: a) A visualisation of field evaporation. b) Potential energy vs distance diagram [41].

Field evaporation of atoms is not guaranteed at a given a temperature and field strength, but the probability of evaporation, P_{evap}, generally follows the Maxwell-Boltzmann equation (EQ.17) [41]:

$$P_{evap} \propto e^{\left(-\frac{Q(F)}{k_B T}\right)} \qquad (17)$$

The predicted evaporation rate, Φ_{evap}, (EQ.18) incorporates the probability of evaporation and the ν_0 which relates to the atom's oscillating frequency [41].

$$\Phi_{evap} = \nu_0 P_{evap} \qquad (18)$$

This equation has been supported by experimental observation but deviates at high temperatures and temperatures lower than 40K [41]. Figure 15 shows a simple plot for

conditions that would allow for field evaporation. Increasing the electric field strength and/or the temperature of the sample should produce field evaporated ions.

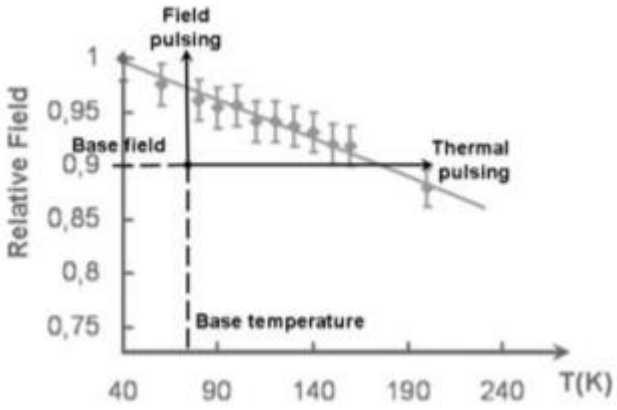

Figure 15: Plot illustrating conditions that allow for field evaporation [41].

The first step in APT is to make needle-shaped tips to be evaporated. These are made through ion milling or electrochemical etching. The tip should allow preferential field evaporation of atoms at the apex of the tip. The predictable order that the atoms evaporate in makes reconstruction a simpler process. During testing, the sample is kept at a low temperature and is subjected to an electric field. The sample is kept below the temperature and field strength at which the probability for field evaporation is high (Figure 15). It is subsequently pulsed, either the temperature or the field strength, so that it alternates between conditions that allow for field evaporation and those that do not. The pulsing is done to control the evaporation rate and to reduce ions being simultaneously detected. The time of flight data is recorded and is simply the time it takes the atom to reach the detector after a pulse. The time of flight is then used to calculate

the mass-to-charge ratio, which identifies the detected element. If the sample is instead held in a field evaporation region, the time of flight would be then be unknown, leaving the detected ions unidentifiable. The data obtained from the detectors allows for a 3D spatial reconstruction of the atom probe tip.

4.42 Common Artefacts

To interpret APT data accurately, an understanding of common artefacts and errors is required. An artefact in APT is a result that is influenced by the testing method and does not accurately reflect the sample. Key errors that may arise are preferential retention/evaporation, surface diffusion, complexes, and identical mass-to-charge ratios. If elements in the sample have a significantly different affinity towards field evaporation, preferential retention/evaporation may occur. An element may be retained for a time in the sample until the field strength increases. This would show a spatial shift of the retained element which does not reflect the true profile. Surface diffusion can occur in samples with an elevated temperature and surface-active elements. Keeping the sample at low temperatures can help to minimize this artefact. Complexes such as hydrides and oxides can form on the tip during evaporation. Finding these complexes in the results does not mean they were necessarily in the original tip. Lastly, charge-to-mass ratios can be shared between elements. The relative abundance of isotopes can be used deduce the contributions of each element but there would still be ambiguity in spatially identifying the individual elements.

4.43 Atom Probe Tomography Method

Dr. Brian Langelier conducted all APT tests at the CCEM. Various ferrite-austenite interfaces from several alloy systems were tested. The reason for these tests was to study the alloying element segregation at the phase interface. The needles were created using a focused ion beam (FIB). Each interface selected was sufficiently far enough away from the sides of the sample so that the one-dimension carbon diffusion assumption would hold.

Once the tip has been made, it is ready to be field evaporated. The needles were field evaporated using laser pulses. Pulse frequency and energy can be varied along with temperature and the electric field. The pulse frequency was typically 250kHz at an energy of 60pJ. The temperature was kept low to decrease error and averaged 47.7K. The evaporated ions were detected and used to spatially reconstruct the tip in IVAS. The IVAS software was used to deconvolute elements that shared the same charge-to-mass ratio.

5.0 APT Results

The APT tests were conducted at the CCEM by Dr. Brian Langelier. Several ternary and quaternary alloy systems were investigated. The Fe-Ni-C, Fe-Al-C, and Fe-Mn-Al-C samples were prepared at McMaster university while the rest were prepared at Monash university under the direction of Dr. Christopher Hutchinson. Linear concentration profiles across the interfaces have been prepared by using a cylindrical ROI with a radius of approximately 25 nm (*Figure* 16). Through these concentration profiles, the segregation

behaviour of the various elements can be observed. The austenite or former austenite was identified as the phase with the larger carbon concentration in the APT tip. It was labelled γ and the ferrite was labelled α on the profiles. The profiles are in the analysis direction (left to right) unless explicitly stated. Profiles not in the analysis direction will be labelled as Opposite of the Analysis Direction (OAD).

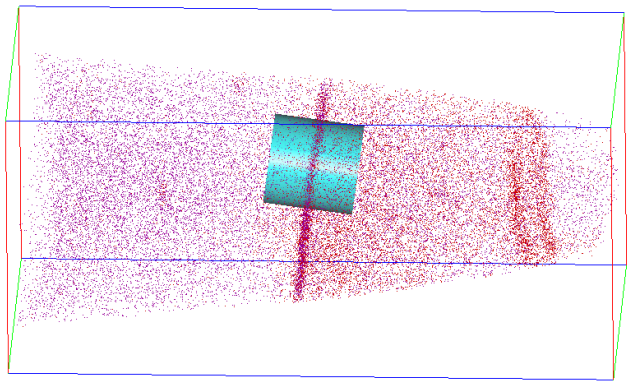

Figure 16: Cylindrical ROI used to create the profile for an Fe-Mn-Mo-C APT tip. Carbon atoms represented in red.

5.1 Ternary Systems

Four ternary Fe-X-C alloy systems were investigated using APT. These alloys systems are: Fe-Ni-C, Fe-Al-C, Fe-Mn-C, and Fe-Mo-C. The Fe-Ni-C samples had a nickel concentration gradient from 1 wt% Ni to 5wt% Ni. The rest of the alloys were homogeneous in concentration. The APT results of an Fe-Si-C alloy reported by Van Landeghem et al. were also included as these results will be further analyzed in the discussion [42].

5.11 Fe-Ni-C

Three samples of the Fe-Ni-C diffusion couple were investigated using APT. These samples differed in decarburization times but were all decarburized at 775°C. The shortest time was 120 min (Figure 17) and showed carbon segregation but negligible nickel segregation. The next longest time was 465 min and two tips from this sample were tested (Figure 18,Figure 19). These showed carbon and nickel segregation at the interface, though the nickel segregation was relatively low. The longest time was 870 min (Figure 20) and both carbon and nickel segregation were observed.

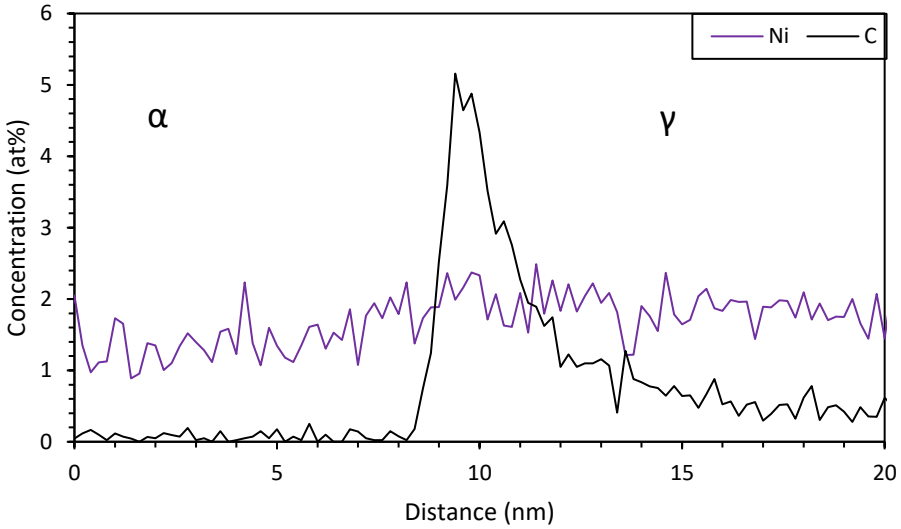

Figure 17: APT profile for Fe-Ni-C diffusion couple, decarburized at 775°C for 120 min.

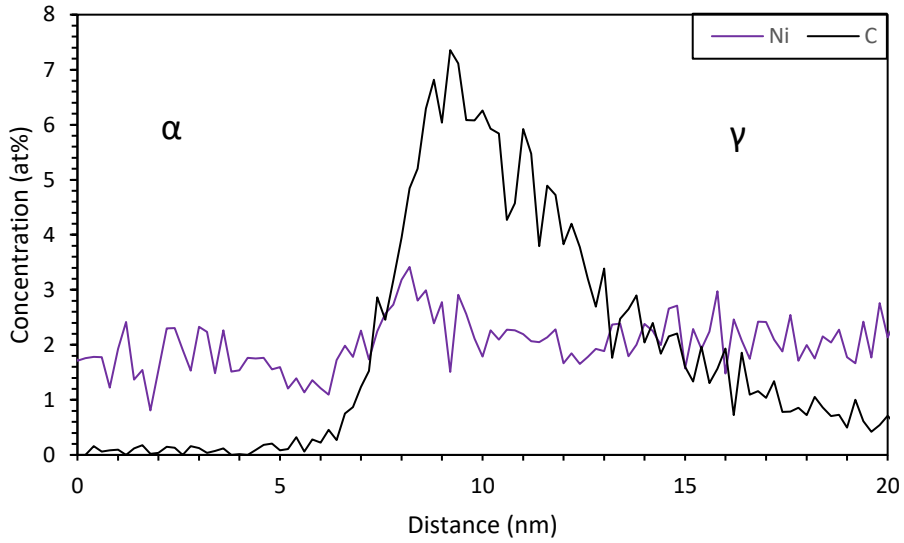

Figure 18: APT profile for Fe-Ni-C diffusion couple, decarburized at 775°C for 465 min. (Tip A)

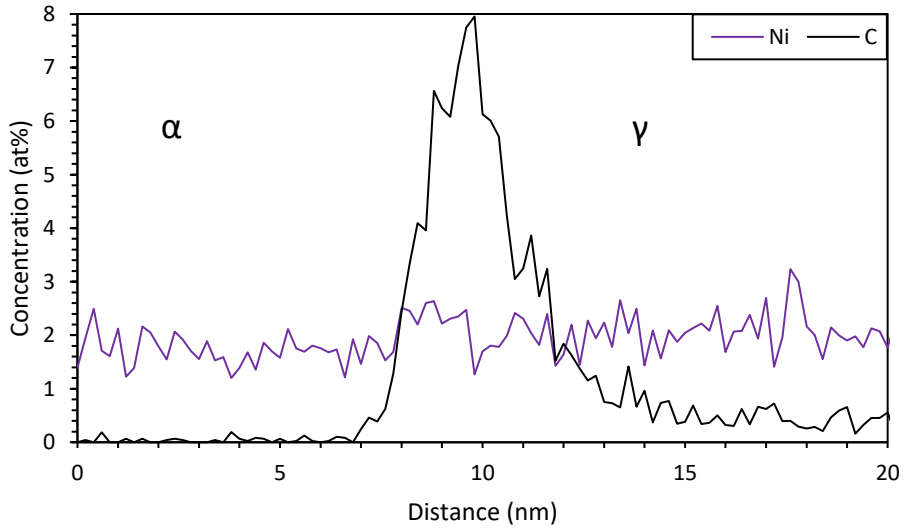

Figure 19: APT profile for Fe-Ni-C diffusion couple, decarburized at 775°C for 465 min. (Tip B)

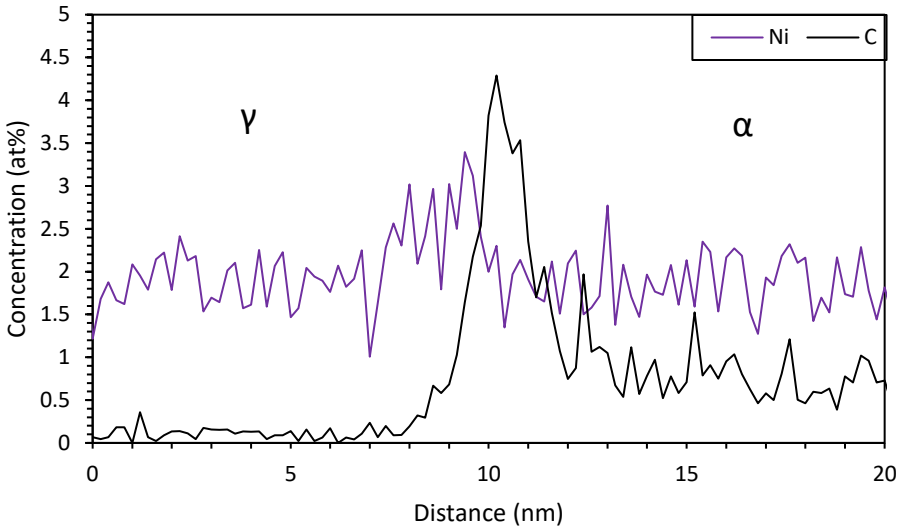

Figure 20: APT profile for Fe-Ni-C diffusion couple, decarburized at 775°C for 870 min.

5.12 Fe-Al-C

Two samples were investigated from the Fe-1.0Al-0.6C alloy. These samples varied in both decarburization time and temperature. The first sample was decarburized at 900°C for 32 min (Figure 21). The second sample had two tips investigated and was decarburized at 950°C for 64 min (Figure 22,Figure 23). All three tips tested showed negligible aluminum segregation and strong carbon segregation.

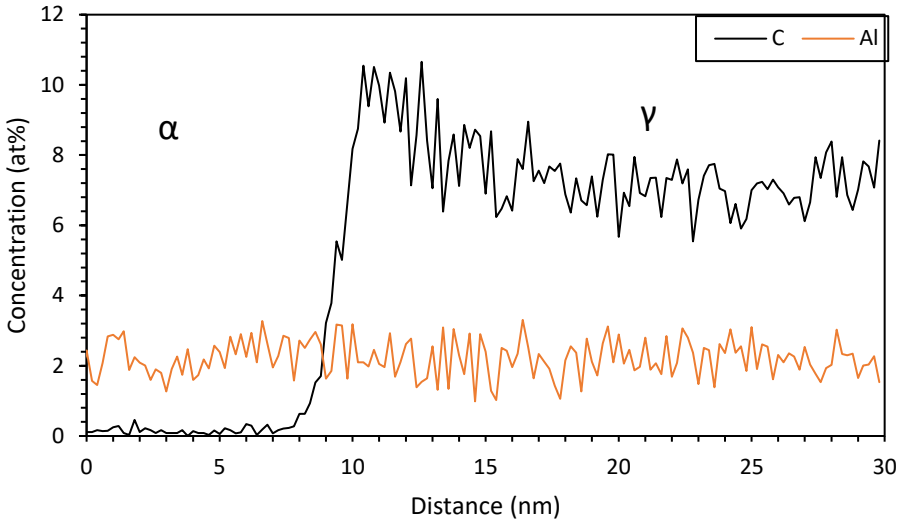

Figure 21: APT profile for Fe-1.0Al-0.6C alloy decarburized at 900°C for 32 min.

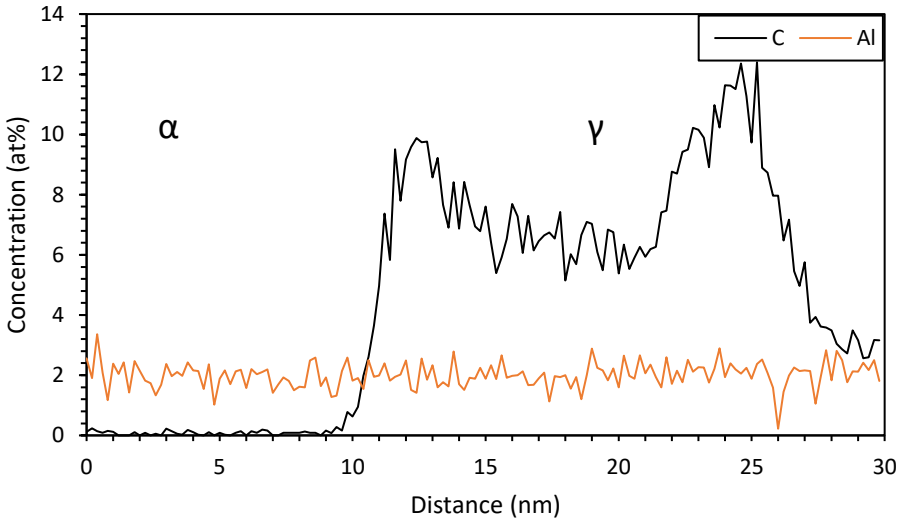

Figure 22: APT profile for Fe-1.0Al-0.6C alloy decarburized at 950°C for 64 min. (Tip A)

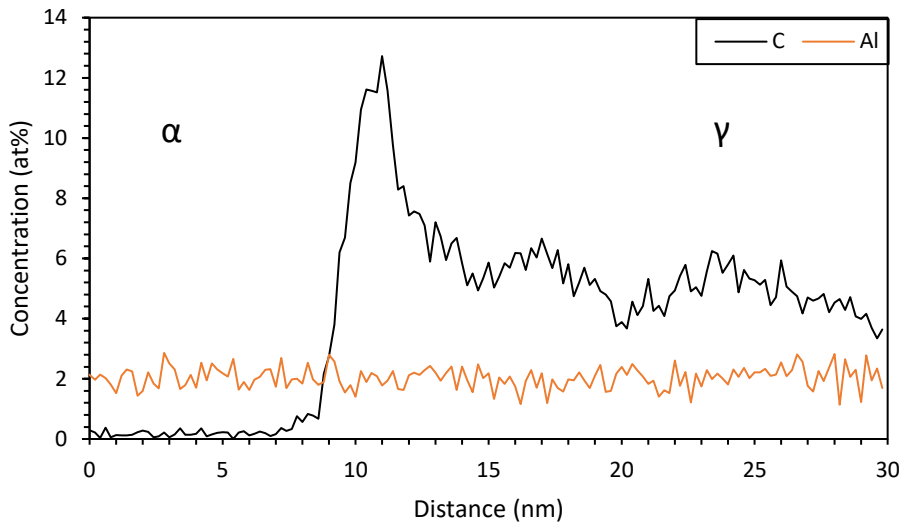

Figure 23: APT profile for Fe-1.0Al-0.6C alloy decarburized at 950°C for 64 min. (Tip B)

5.13 Fe-Mn-C

One sample was investigated from the Fe-1.41Mn-.47C alloy. The sample was decarburized at 775°C for 18.5 min and two tips were tested using APT (Figure 24,Figure 25). Both tips showed strong carbon and manganese segregation at the interface.

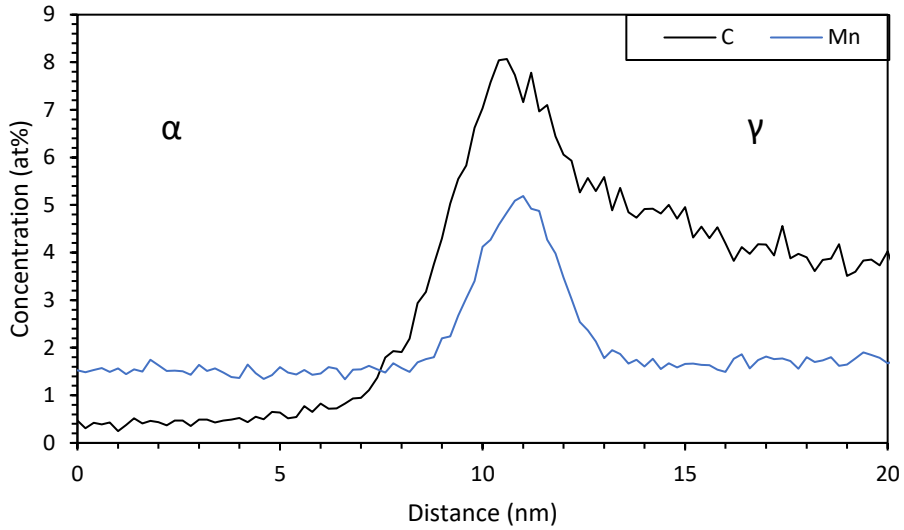

Figure 24: APT profile for Fe-1.41Mn-.47C alloy decarburized at 775°C for 18.5 min. OAD (Tip A)

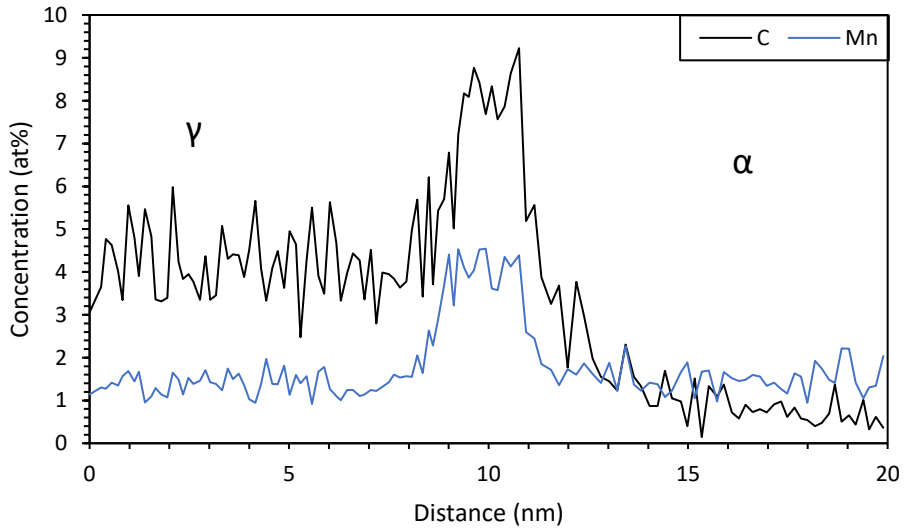

Figure 25: APT profile for Fe-1.41Mn-.47C alloy decarburized at 775°C for 18.5 min. (Tip B)

5.14 Fe-Mo-C

One sample from the Fe-.51Mo-.54C alloy was investigated. It was decarburized at 775°C for 79 min and exhibited strong molybdenum and carbon segregation (Figure 26).

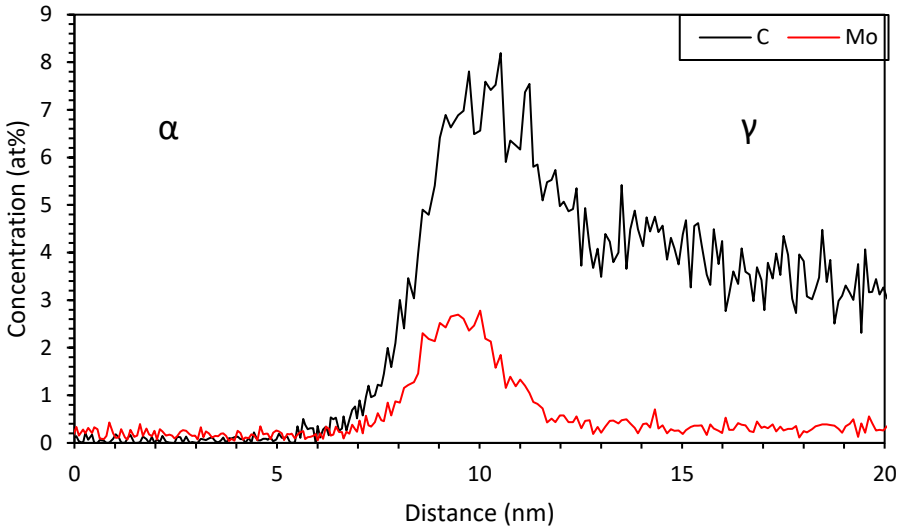

Figure 26: APT profile for Fe-.51Mo-.54C alloy decarburized at 775°C for 79 min.

5.15 Fe-Si-C

Two samples from the Fe-1.61(at%)Si-3.41(at%)C alloy were investigated by Van Landeghem et al. [42]. These were decarburized 775°C for 64 min (Figure 27a) and 240 min (Figure 27b). Both samples showed strong carbon segregation while only the 64 min sample exhibited silicon desegregation at the interface.

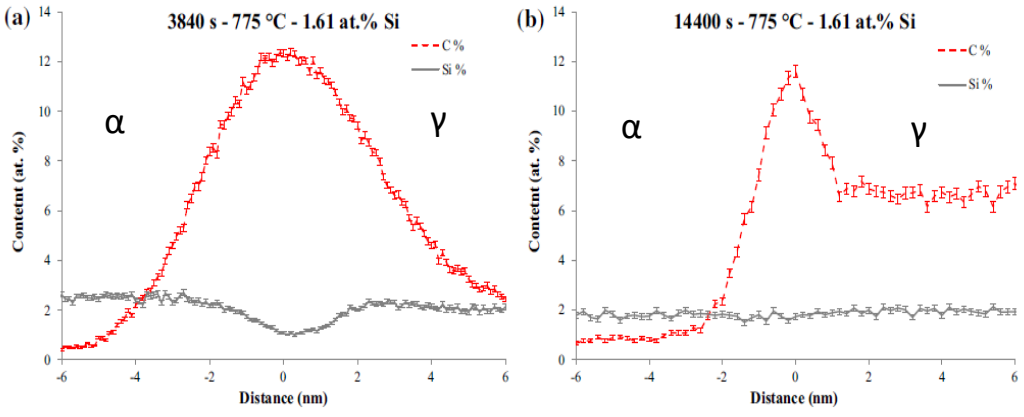

Figure 27: APT profiles for Fe-1.61at%Si-3.41at%C alloy decarburized at 775°C for a) 64 min and b) 240 min [42].

5.2 Quaternary Systems

Three quaternary Fe-X-Y-C systems were investigated using APT. These three systems include Fe-Mn-Al-C, Fe-Mn-Si-C, and Fe-Mn-Mo-C. Manganese was included in all three systems in order to investigate possible co-segregation behaviour between manganese and the other three substitutional elements.

5.21 Fe-Mn-Al-C

Two samples, each with a different composition, were investigated in the Fe-Mn-Al-C system. Both samples were decarburized at 900°C for 17 min. The first composition is Fe-1.9Mn-1.8Al-0.6C and two tips were tested (Figure 28,Figure 29). The second composition is Fe-.94Mn-.94Al-0.6C (Figure 30). Both samples had strong carbon and manganese segregation, with negligible aluminum segregation at the interface.

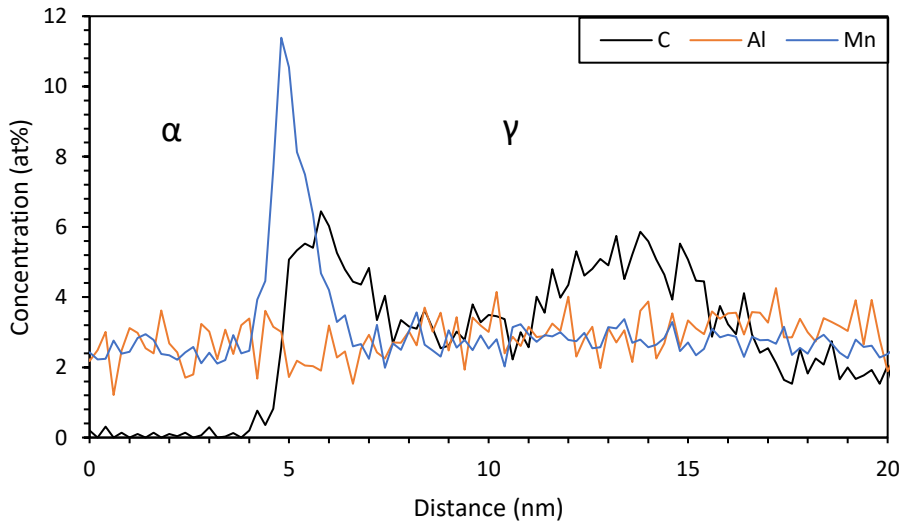

Figure 28: APT profile for Fe-1.9Mn-1.8Al-0.6C alloy decarburized at 900°C for 17 min. (Tip A)

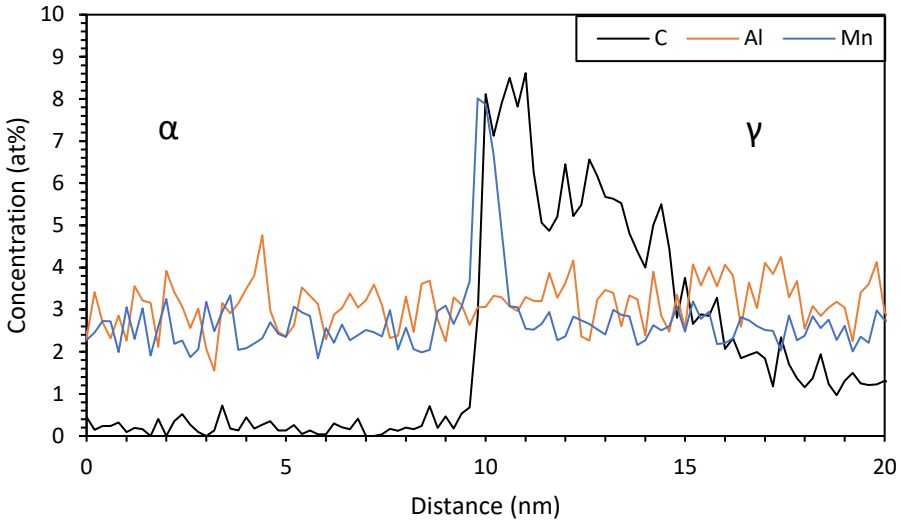

Figure 29: APT profile for Fe-1.9Mn-1.8Al-0.6C alloy decarburized at 900°C for 17 min. (Tip B)

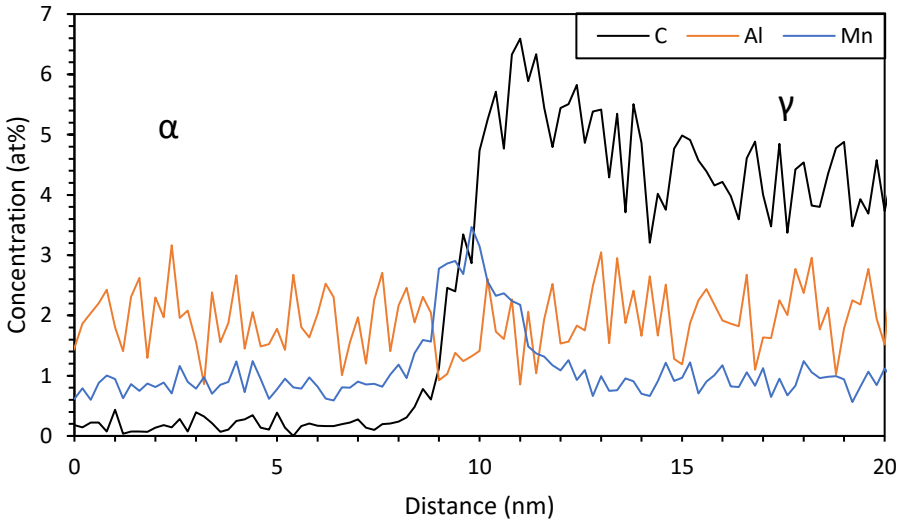

Figure 30: APT profile for Fe-94Mn-.94Al-0.6C alloy decarburized at 900°C for 17 min.

5.22 Fe-Mn-Si-C

Three different alloy compositions were investigated for the Fe-Mn-Si-C system. The samples from the Fe-1.5Mn-1.3Si-.66C and Fe-1.0Mn-0.9Si-.68C compositions had ferrite

precipitation ahead of the interface (Figure 31,Figure 32). Possible causes of the ferrite precipitation will be discussed in the subsequent section. Both of these alloys were decarburized at 755°C for 240 min. The Fe-1.5Mn-1.3Si-.66C alloy had one tip tested (Figure 33) while the Fe-1.0Mn-0.9Si-.68C alloy had two tips tested (Figure 34,Figure 35). All three tips exhibited manganese and carbon segregation while only the Fe-1.5Mn-1.3Si-.66C alloy exhibited silicon segregation. The two tips from the Fe-1.0Mn-0.9Si-.68C alloy had negligible silicon segregation. The Fe-1.5Mn-1.5Si-.67C alloy was also decarburized at 755°C for times of 16 min and 32 min. The 16 min sample had one tip tested (Figure 36) and the 32 min sample had three tips tested (Figure 37,Figure 38Figure 39). None of these samples had ferrite precipitation ahead of the interface and they all exhibited manganese and carbon segregation. All the tips had silicon segregation present at the interface except for tip “C” of the 32 min sample.

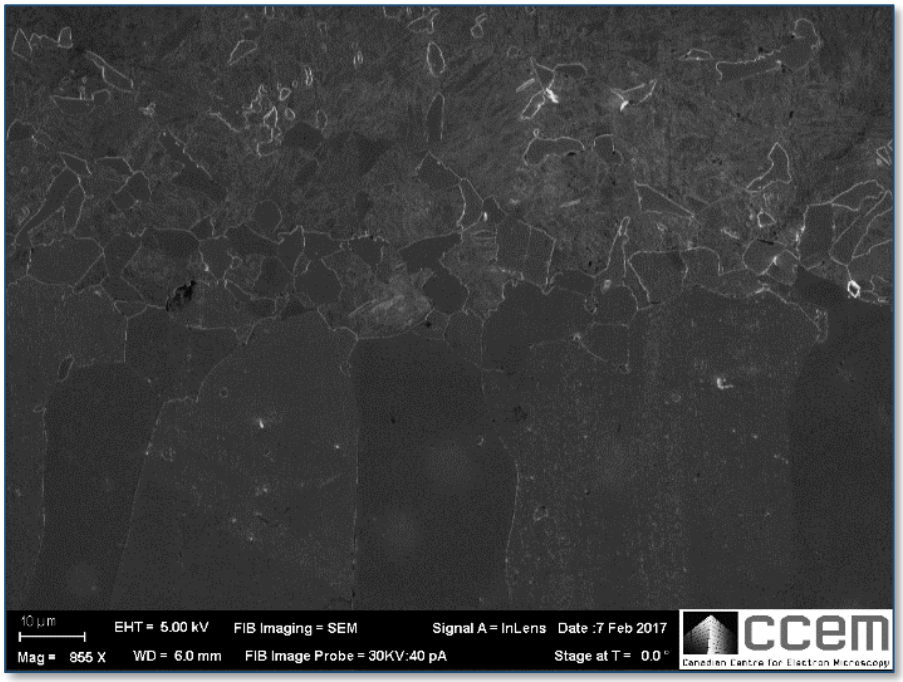

Figure 31: SEM image of ferrite precipitation in the Fe-1.5Mn-1.3Si-.66C sample.

Figure 32: SEM image of ferrite precipitation in the Fe-1.0Mn-0.9Si-.68C sample.

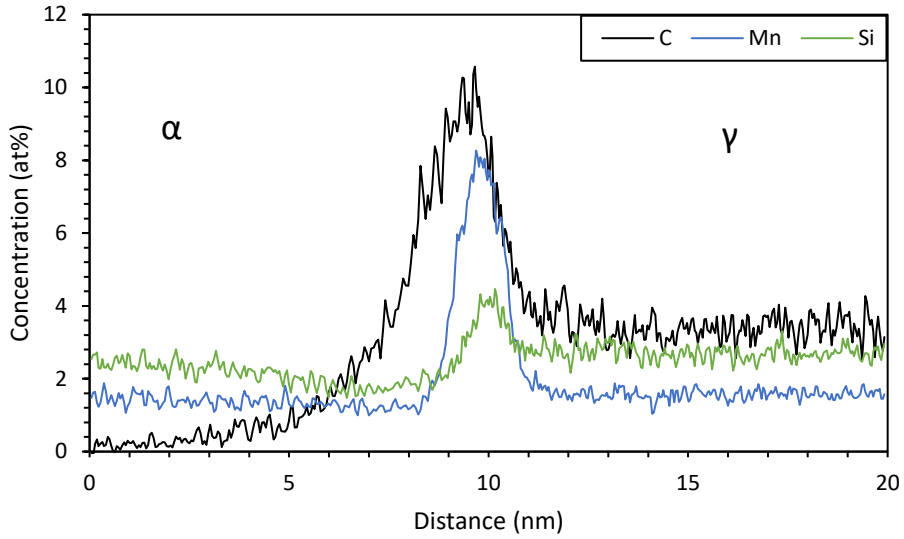

Figure 33: APT profile for Fe-1.5Mn-1.3Si-.66C alloy decarburized at 755°C for 240 min. OAD

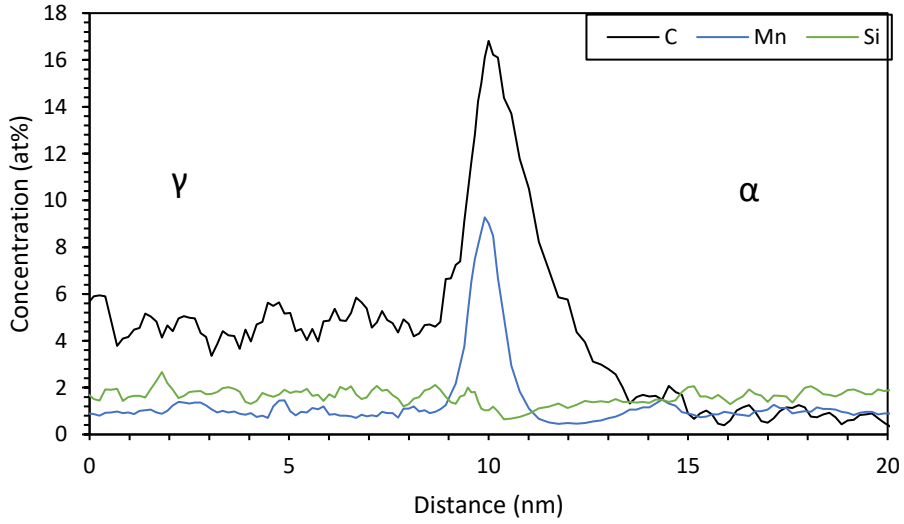

Figure 34: APT profile for Fe-1.0Mn-.9Si-.68C alloy decarburized at 755°C for 240 min. (Tip A)

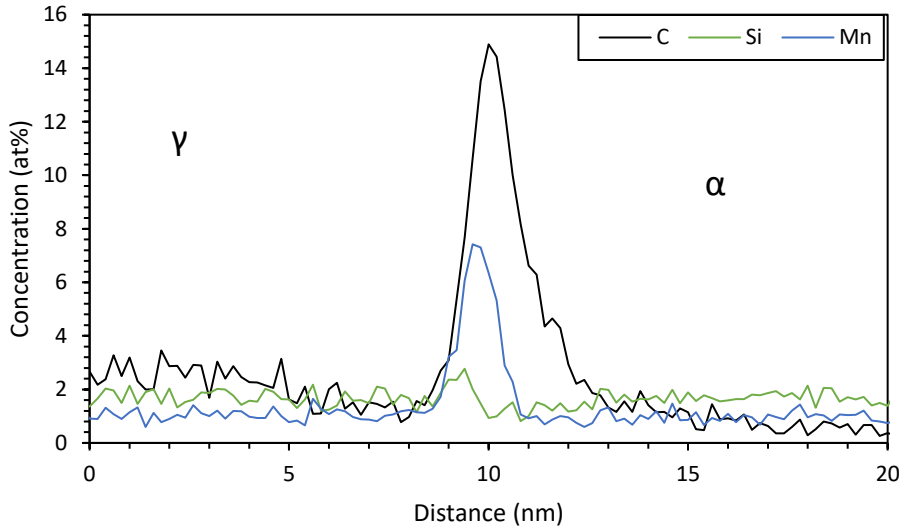

Figure 35: APT profile for Fe-1.0Mn-.9Si-.68C alloy decarburized at 755°C for 240 min. (Tip B)

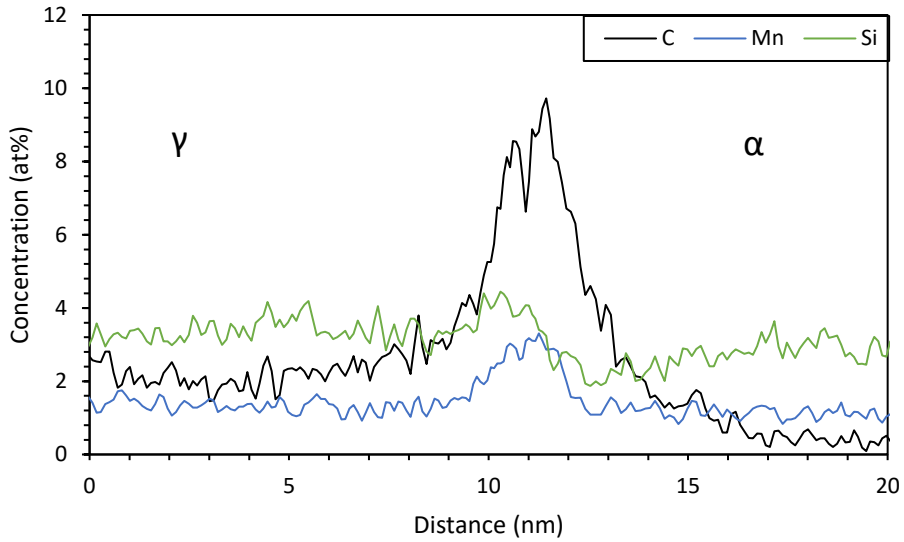

Figure 36: APT profile for Fe-1.5Mn-1.5Si-.67C alloy decarburized at 755°C for 16 min.

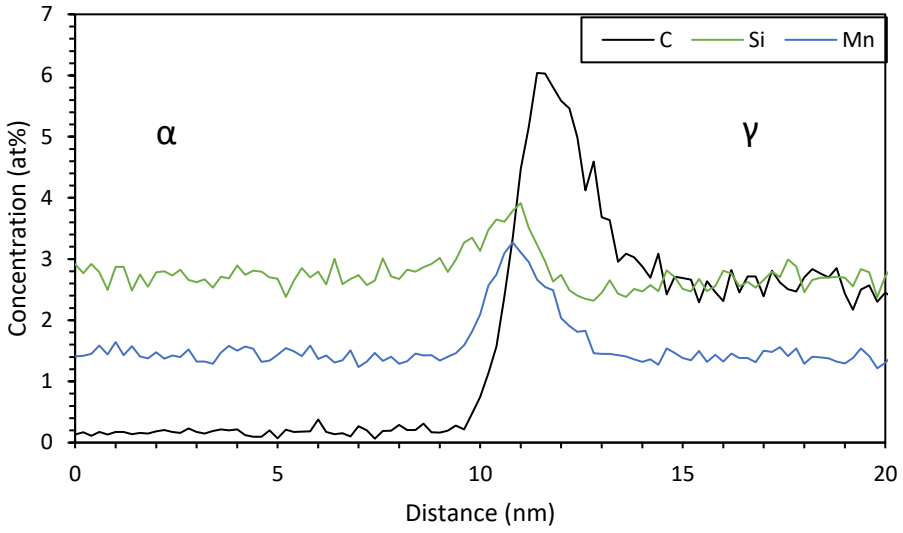

Figure 37: APT profile for Fe-1.5Mn-1.5Si-.67C alloy decarburized at 755°C for 32 min. (Tip A)

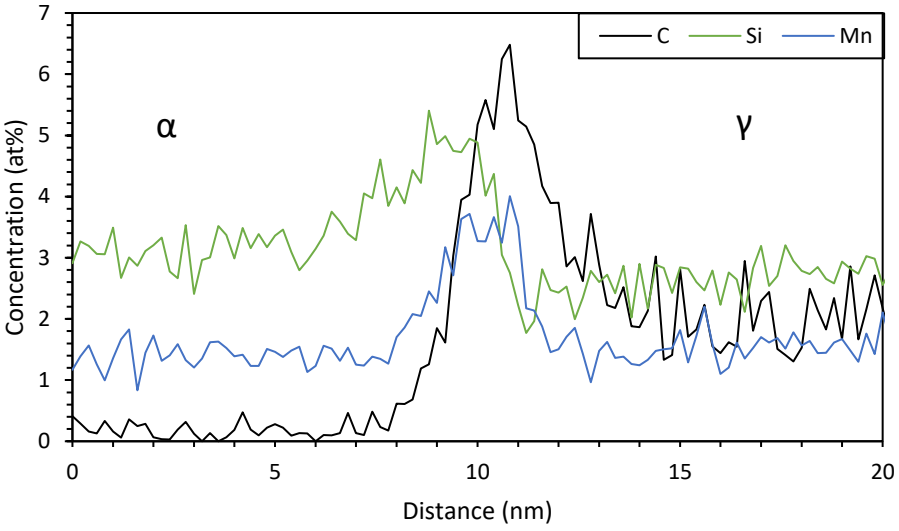

Figure 38: APT profile for Fe-1.5Mn-1.5Si-.67C alloy decarburized at 755°C for 32 min. (Tip B)

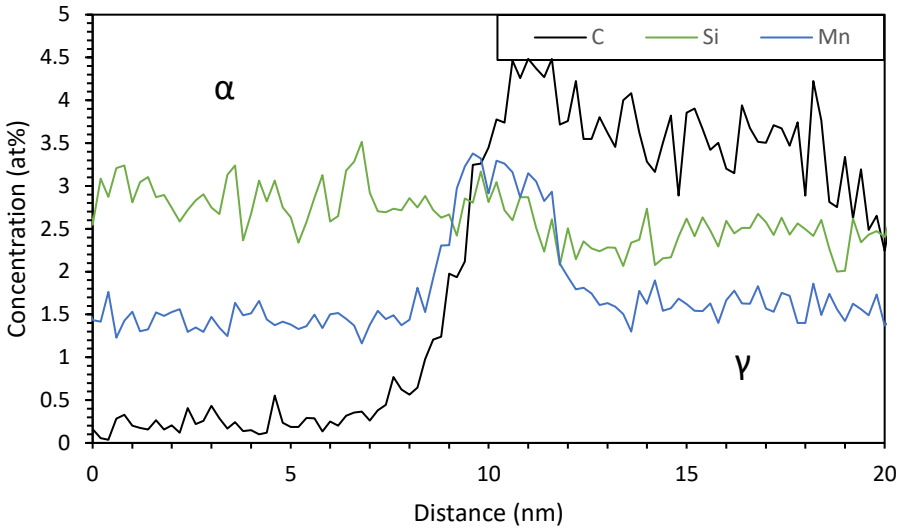

Figure 39: APT profile for Fe-1.5Mn-1.5Si-.67C alloy decarburized at 755°C for 32 min. (Tip C)

5.23 Fe-Mn-Mo-C

Three samples from the Fe-1.36Mn-.42Mo-.48C alloy were investigated using APT. Each sample was decarburized at 775°C and two tips were tested for each sample. The three samples had varying decarburization times, with times of 23.5 min (Figure 40Figure 41), 120 min (Figure 42,Figure 43), and 240 min (Figure 44,Figure 45). All 6 tips exhibited strong carbon, manganese, and molybdenum segregation at the interface. EELS was also conducted on the 23.5 min sample and the results can be found in Appendix 1.

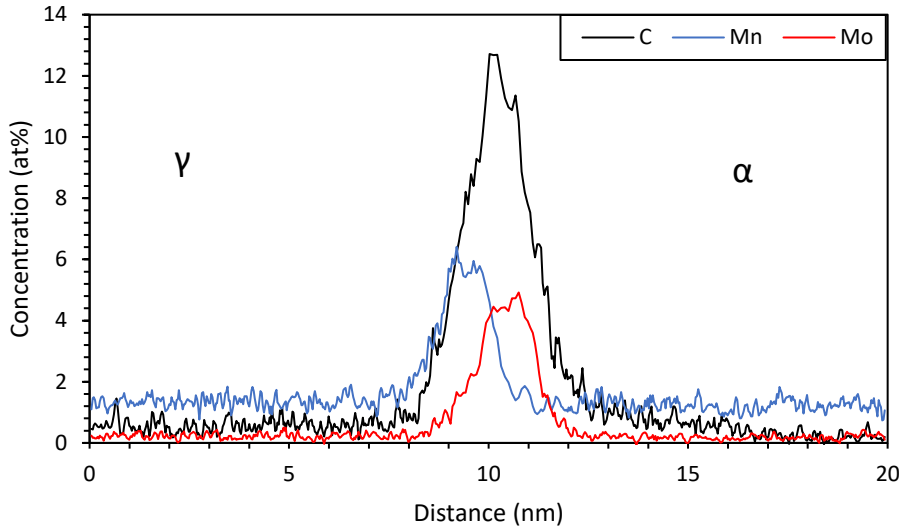

Figure 40: APT profile for Fe-1.36Mn-.42Mo.48C alloy decarburized at 755°C for 23.5 min. (Tip A)

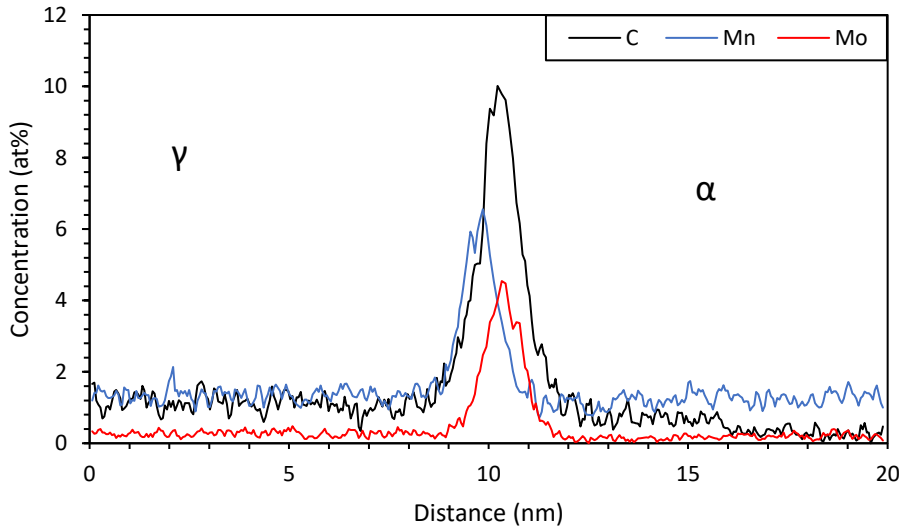

Figure 41: APT profile for Fe-1.36Mn-.42Mo.48C alloy decarburized at 755°C for 23.5 min. (Tip B)

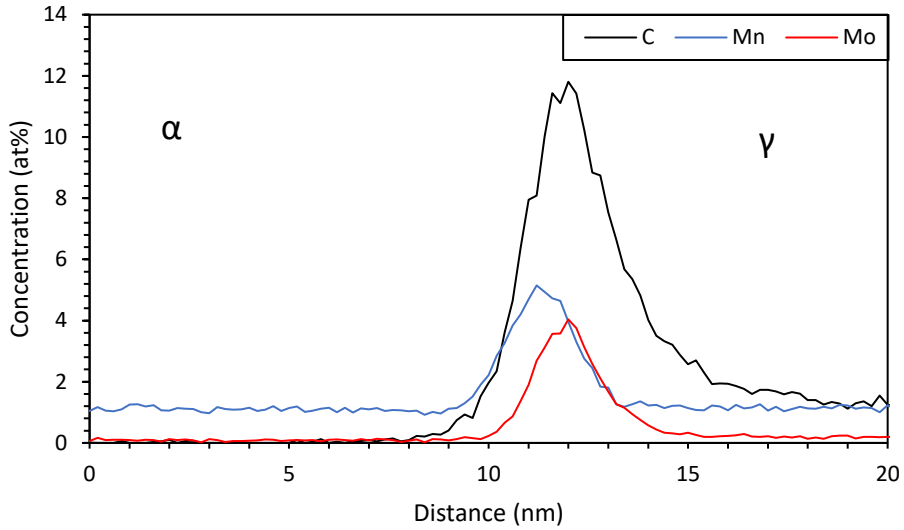

Figure 42: APT profile for Fe-1.36Mn-.42Mo.48C alloy decarburized at 755°C for 120 min. (Tip A)

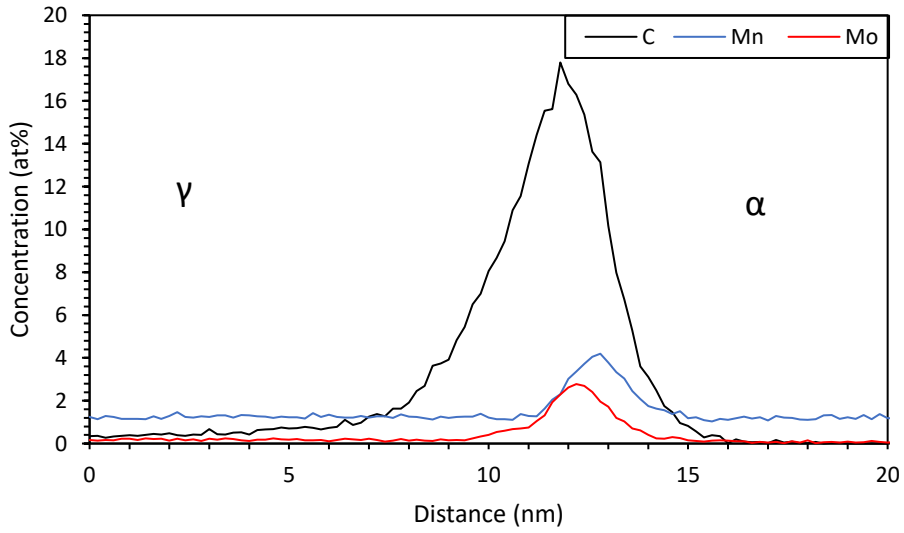

Figure 43: APT profile for Fe-1.36Mn-.42Mo.48C alloy decarburized at 755°C for 120 min. OAD (Tip B)

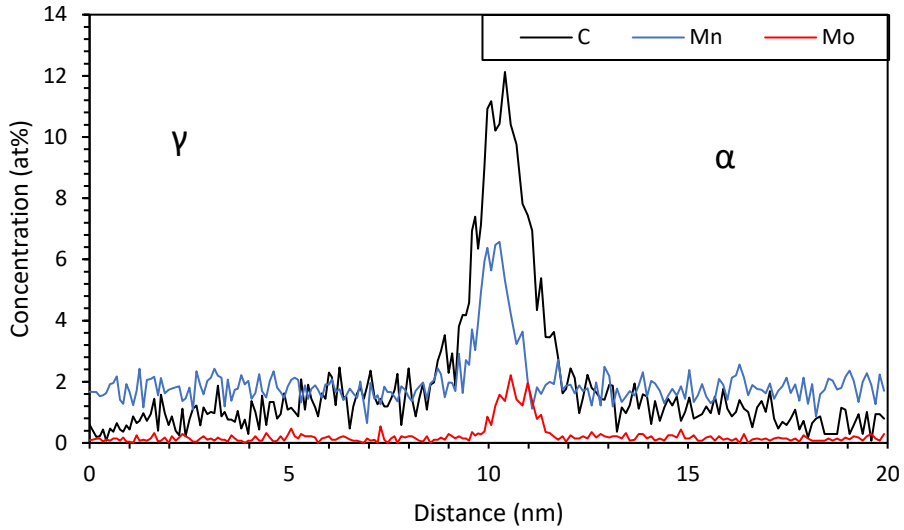

Figure 44: APT profile for Fe-1.36Mn-.42Mo.48C alloy decarburized at 755°C for 240 min. (Tip A)

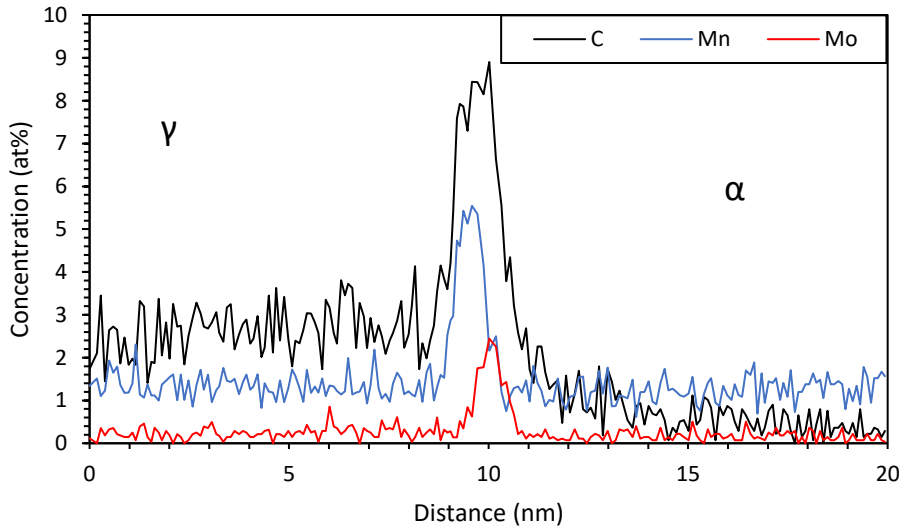

Figure 45: APT profile for Fe-1.36Mn-.42Mo.48C alloy decarburized at 755°C for 240 min. (Tip B)

6.0 Discussion

Before beginning the analysis of the APT results and discussing their implications on energy dissipation, complications to the analysis should be discussed. Three complications

that will be subsequently discussed are: interfacial roughness, interfacial velocity, and the behaviour of carbon at the interface. All three of these provided challenges in analyzing the segregation behaviour of elements at the interface.

6.1 Interfacial Roughness

An interface that is relatively flat would be simple to analyze. There would be little ambiguity as to the position of the interface and the ROI used to create the APT profiles could be placed perfectly normal to the interface. It was thought that the interface would appear relatively smooth as the scale becomes finer. However, the Transmission Electron Microscopy (TEM) work of Hui Yuan [43] has shown that the ferrite/austenite interface can have significant roughness, even on the nanometer scale (Figure 46). As the TEM image shows, the roughness varies significantly across the width and the depth of the foil. This is significant because the analysis of APT results usually involves the use of a cylindrical ROI of radius ~25 nm. The roughness of the interface within this volume would lead to a broad solute profile across the interface. Although the TEM image is of a duplex stainless steel, this same roughness can be seen while creating the tip and in the final APT reconstruction. Interfacial roughness provides a challenge in interpreting the APT results. This roughness likely broadens the segregation profiles in the APT results. Reporting the peak solute concentration is common for APT, but if broadening takes place, the peak value does not convey the true extent of the segregation. To more accurately depict the

solute segregation, the excess area will instead be calculated. The method of calculation is included in section 6.4.

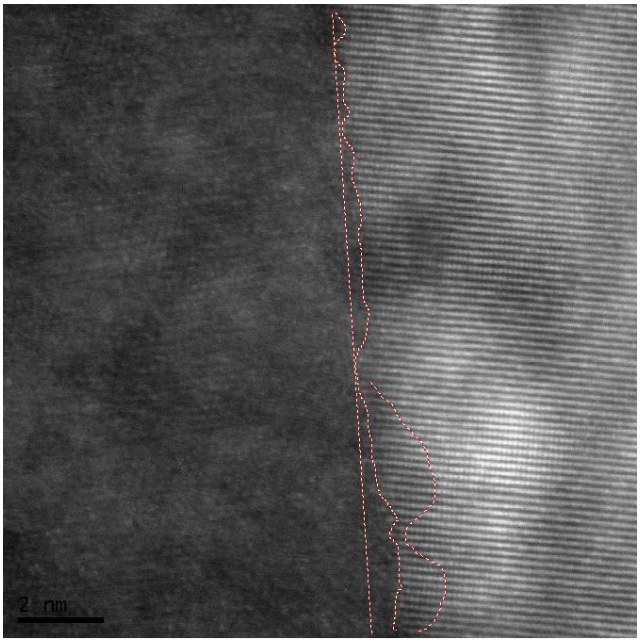

Figure 46: TEM image of the ferrite/austenite interface in a duplex stainless steel [43].

6.2 Interfacial Velocity

It is generally understood that segregation to a moving boundary is non-equilibrium segregation [30,44-48]. At a sufficiently high velocity, the substitutional element cannot keep up with the interface and as a result there is less segregation. As the velocity approaches zero, the segregation should approach the equilibrium level. Initially, the ternary manganese and molybdenum samples were selected because they would have the same velocity based on the global transformation kinetics. The challenge faced is that the local velocity varied depending on quenching conditions and (potentially) depending on the local position within at the interface. For example, it is estimated that during the

argon purge, the velocity would certainly decrease as the driving force from decarburization has ceased. The sample remains at high temperature during this time and the alloying elements would continue to diffuse for the three to five minutes of purging. After the purge, the interface may also move slightly during the quench, adding another uncertainty to the velocity. Therefore, the purge and quench may alter the instantaneous velocity of the interface. This could in turn alter the segregation at the interface and make it appear as though segregation was not a function of velocity. It is also important to keep in mind possible variations within the interface. Inhomogeneities at grain boundaries have been widely reported [48-53] and it is quite possible that inhomogeneities would also exist at phase interfaces. Significant variations in segregation values have been observed within the same sample and even the same tip. These variations could overshadow the impact of the velocity. If the velocity difference is small or the impact itself is weak, the effect of velocity on segregation may not rise above the noise. In that case, several more regions of the interfaces would need to be investigated to get a more accurate representation of the segregation. Given these explanations, it is concluded that although velocity would be a factor during the transformation, it cannot be accurately quantified from the APT results.

6.3 Carbon Behaviour

The last difficulty in analyzing the APT results is the behaviour of carbon at the interface. First, the carbon behaviour in the APT results will be summarized and then the complications associated with the analysis will be discussed.

Carbon segregated strongly to each of the tested interfaces. As an interstitial element, there is a significant driving force for carbon to diffuse to lattice defects and reduce strain energy. The incoherent interface formed by decarburization provides an abundance of sites that would attract carbon atoms. The carbon segregation observed in the APT results is in agreement with the segregation behaviour of carbon in literature [17,42,54,55]. Carbon segregation varied significantly even within the same sample. At times, the carbon concentration was higher than predicted in the martensite and could be evidence of it actually being retained austenite or a precursor to a carbide. However, definitive conclusions cannot be given on the behaviour of carbon in the martensite.

Although carbon segregation is thought to be an important factor in the segregation behaviour of the other elements, it was the only element that was not analyzed using excess area. Three reasons for this decision are: the room temperature mobility of carbon, influences of quenching, and artefacts that the limit spatial accuracy of carbon in APT. Even though the diffusion coefficient of carbon is often two orders of magnitude less at room temperature than at decarburization temperature, carbon atoms cannot be considered strictly immobile. This effect is clear in the Fe-Ni-C samples. The 465 min

samples (Figure 18Figure 19) were aged at room temperature for two years whereas the rest were only aged for a month (Figure 17Figure 20). The carbon segregation in these profiles is significantly higher with longer aging time. As time progresses, the carbon segregation could approach amounts that reflect the ferrite/martensite interface at room temperature rather than the ferrite/austenite interface at the transformation temperature. Next, the carbon profile could be more susceptible to quenching conditions. Carbon cannot be considered strictly immobile during the quench, unlike the substitutional elements. If the quench is long enough, carbon may diffuse to the interface or the austenite. Studies have shown that segregation can increase with a slower quench at higher temperatures [56]. Lastly, artefacts from APT can alter the carbon concentration profile. The most significant artefact is the preferential retention of carbon during evaporation. This causes the carbon peak to be offset from the other solute peaks such as manganese. It is consistently shown in the data that the offset occurs in the direction of evaporation. To confirm preferential retention was the cause of the offset, the 465 min and 870 min Fe-Ni-C APT tips were evaporated in opposite directions. Both show that the nickel spike precedes the carbon segregation, regardless of evaporation direction. This offset due to preferential retention is a nanometer on average and could alter the perceived segregation amounts. The “tail” following the carbon segregation is also caused by carbon being retained at the tip surface and spreading the segregation past the interfacial region. For the previous reasons listed, the carbon profile observed through APT may not quantitatively reflect the carbon profile during the transformation. Carbon

could certainly be a significant factor in the segregation of the substitutional elements, but the uncertainty of its behaviour cannot be sufficiently controlled. Therefore, carbon segregation will not be quantified, and significant conclusions should not be based on the carbon profiles.

6.4 Calculating Excess Area and K_{2nm}

The primary data extracted from the APT profiles was the excess area at the interface. The excess area was chosen over the peak concentration for several reasons. The robustness of excess area is a significant advantage over using the peak concentration. Peak concentration is susceptible to interface roughness, a misaligned ROI, and several artefacts that may spread the segregation. Although the spreading from interface roughness could be decreased by using a smaller radius for the ROI, this would significantly increase the statistical uncertainty in the data. Using excess area allows for segregation that has been spread out during evaporation to still contribute to the data. A second advantage to using excess area is that it conveys more information. Two profiles may have identical peak concentrations, but one may be broad and the other thin. The broad peak could have double the excess area of the thin peak, but that information would be lost when conveying only the peak concentration. One final advantage of using excess area is its versatility. The chemical potential profile of each element across the interface remains uncertain. The excess area can be reshaped into various profiles as

advancements come in interface thermodynamics. Therefore, excess area will be the primary data analyzed from the APT results.

To calculate excess area, an understanding of what each data point represents is required. The APT profiles were constructed using a cylindrical ROI with a radius of approximately 25 nm. Each data point represents the concentration of an individual slice of the ROI. Each slice has a fixed thickness known as the bin width. Fixing the bin width allows for each data point to represent a uniform volume and these APT profiles typically had a bin width fixed at 0.2 nm. Therefore, each point of the APT profile is the concentration of a fixed volume with a fixed bin width.

The excess area (A_{ex}) is the area under the segregation spike (A_{spike}) with the contribution from the bulk (A_{bulk}) removed, (EQ.19):

$$A_{ex} = A_{spike} - A_{bulk} \qquad (19)$$

A sample profile was created to visualize the excess area calculations (Figure 47). The area under the spike was calculated using EQ.20:

$$A_{spike} = \sum_{i=x_1}^{x_2} X_i w \qquad (20)$$

Where X_i is the concentration of the individual point in at% and w is the fixed bin width in nm. x_1 and x_2 are simply the beginning and end positions of the spike. A_{bulk} was calculated using EQ.21:

$$A_{bulk} = \sum_{i=x_1}^{x_2} X_{average} w \qquad (21)$$

w, x_1, and x_2 are the same values used when calculating A_{spike}. $X_{average}$ is the average concentration in the APT profile. The average was comprised of all the points in the profile except points from the segregation spike and regions significantly affected by artefacts.

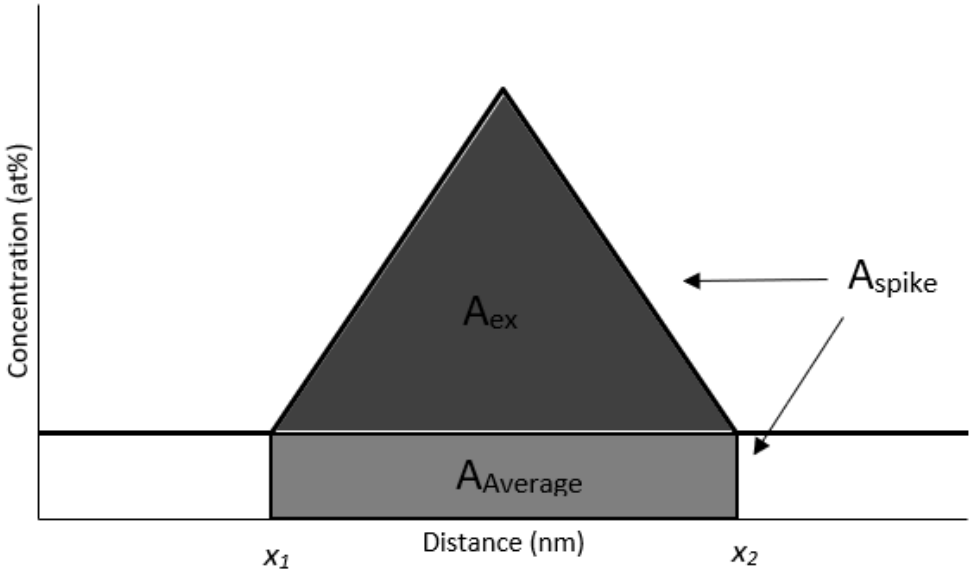

Figure 47: Visualization of excess area calculation.

The other value calculated from the APT data is K_{2nm}. K_{2nm} is the ratio of segregation concentration to bulk concentration if the excess area was made into a rectangle with a 2 nm width. This was calculated using EQ.22:

$$K_{2nm} = 1 + \frac{A_{ex}}{(2nm)X_{bulk}} \qquad (22)$$

K_{2nm} is a unitless ratio with a value of unity when no segregation is present. X_{bulk} is slightly different from the $X_{average}$ used in EQ.21 as this is the concentration confirmed from ICP.

The average APT concentration was not used because it significantly altered the K_{2nm} values, especially for molybdenum. Molybdenum had bulk concentrations ranging from 0.23 at% to 0.3 at%, which were the lowest bulk concentrations of all the substitutional elements studied. The APT average for molybdenum varied between samples and dropped as low as 0.13 at%. This 0.1at% is not out of the ordinary for APT results but it could nearly double the K_{2nm} value. Actual deviations from the bulk concentrations are not expected to be significant so the concentrations confirmed by ICP were used.

K_{2nm} was used solely to compare solute segregation while taking bulk composition into account. The rectangle with a 2 nm width was used for simplicity and is not meant reflect the true profile. The true segregation profile is unlikely to be uniform and could resemble shapes such as the truncated wedge profile that Hillert proposed [33]. K_{2nm} allows for the excess area to be normalised to the bulk concentration of the element. Excess area would certainly change with the bulk concentration, but the impact is not yet quantified. A further discussion on the possible impact that the bulk concentration has on the segregation levels is included in the Appendix 2.

6.5 Ternary Segregation Behaviour

Understanding the behaviour of substitutional elements within the ternary systems is essential to understanding their behaviour in the quaternary systems. For this reason, the segregation behaviour of the substitutional elements will be analyzed and discussed in

the subsequent section. A summary of the excess areas and K_{2nm} values for the ternary samples is included at the end of the section (Table 1).

6.51 Fe-Ni-C

Three Fe-Ni-C diffusion couples were tested using APT (Figure 17Figure 18Figure 19Figure 20). Minor segregation at the interface was found in the 465 and 870 min samples but no segregation was observed in the 120 min sample. This segregation is surprising, as nickel is often thought to have a negligible affinity towards carbon and the interface [54]. Two possible explanations of nickel's behaviour at the interface are provided. The first possible explanation is that nickel does have a slight affinity towards the interface. The 120 min data may simply have been an area of low segregation. The lack of nickel segregation in the Fe-.91at%Ni-2.29at%C alloy analyzed by Van Landeghem et al. [54] would need to be explained in a similar manner. The second possibility is that the nickel segregation is actually a LENP solute spike. LENP spikes are often considered kinetically infeasible due to the low diffusivity of alloying elements in comparison to the interface velocity. However, the velocity is sluggish in this diffusion couple and would make a LENP spike feasible. The only sample to have no excess also has the highest velocity. It is reasonable to assume that the higher velocity was the cause of the uniform concentration (very thin spike). The LENP spike sufficiently explains the APT data and maintains the general consensus on the segregation behaviour of nickel. It is concluded that this is not true nickel segregation but rather a LENP spike at the interface.

This LENP spike may not be a full spike but rather a partial one. It is assumed to be a partial spike rather than a full spike because the interface consistently surpassed the LENP limit during the second decarburization by several microns. This partial spike would produce a slight energy dissipation but it may not be sufficiently noticeable in kinetic results.

6.52 Fe-Mn-C

Manganese has shown significant segregation in the Fe-1.41Mn-.47C sample. The two tips tested had similar segregation amounts with an average excess area of 7.55 at%-nm. The excess area produced a K_{2nm} value of 3.6. Unlike nickel, this segregation could not be a LENP spike as the excess area is greater than expected and the interface velocity is too high to sustain the spike. This segregation was slightly greater than that reported in by Van Landeghem et al. [42,54] and Langelier et al. [55]. They also performed APT on the Fe-Mn-N system and found negligible manganese segregation. This may suggest that manganese has an affinity towards carbon rather than the interface itself or that nitrogen repels the manganese. However, nitrogen and manganese are attracted to each other in the bulk phases so it would seem unlikely that nitrogen would change behaviour at the interface. Regardless, it is clear from this work and from the literature that manganese segregates strongly and consistently to interfaces in the Fe-Mn-C system.

6.53 Fe-Mo-C

Molybdenum also showed significant segregation in the Fe-.51Mo-.54C system. The sample had an excess area of 5.80 at%-nm. Molybdenum has a stronger affinity to the

interface than the rest of the substitutional elements tested. Although manganese had a higher excess area, molybdenum has a K_{2nm} of 10.7, nearly triple that of manganese. This segregation is also slightly higher than the Fe-Mo-C sample studied by Van Landeghem et al. [54]. Strong molybdenum segregation is consistent with literature and several authors have proposed that molybdenum has a significantly high binding energy (BE) to the interface [54,57].

6.54 Fe-Si-C

Although the Fe-Si-C system did not have interfaces investigated using APT in this thesis, silicon was investigated in quaternary alloys. As silicon will be discussed in the quaternary section, it would be prudent to discuss its behaviour in the ternary system. Van Landeghem et al. [42]. investigated an Fe-Si-C alloy at two decarburization times (Figure 27). Desegregation was observed in the 64 min sample but not in the 240 min sample. The 64 min sample has an excess area of (-2.20) at%-nm[1] which amounts to a K_{2nm} of 0.5. The authors suggested that this inconsistent desegregation could be due to local variations along the interface or a slow quench of the 240 min sample that allowed the interface to break away from the desegregation [42]. Even with the variation, it is still clear that silicon is not attracted to the interface.

[1] A negative excess area signifies desegregation.

6.55 Fe-Al-C

The Fe-1.0Al-.6C alloy was decarburized at 900°C and 950°C. One sample from each temperature was tested with APT and each tip showed negligible segregation to the ferrite-austenite interface. This would suggest that aluminum is indifferent to the interface. In light of the silicon results, it is difficult to decisively state that aluminum does not interact with the interface. It may be that the three tips happened to be in regions of low segregation. However, it can be concluded that aluminum does not interact strongly with the interface, unlike manganese and molybdenum.

Table 1: Segregation values for ternary APT samples.

Composition (wt%)	Temperature (°C)	Time (min)	Excess Area (at%-nm)	K_{2nm}
Fe-1.41Mn-.47C	775	18.5	8.4	3.9
Fe-1.41Mn-.47C	775	18.5	6.7	3.3
Fe-0.51Mo-0.54C	775	79	5.8	10.8
Fe-0.88Si-0.7C	775	16	-1.6	0.5
Fe-0.88Si-0.7C	775	240	0	1
Fe-1.0Al-0.6C	900	32	0	1
Fe-1.0Al-0.6C	950	64	0	1
Fe-1.0Al-0.6C	950	64	0	1

6.6 Quaternary

Three quaternary alloy (Fe-X-Y-C) systems were selected to study co-segregation among substitutional elements. Manganese was present across all quaternary alloys while the Y element was varied. The three chosen Y elements were: aluminum, molybdenum, and silicon. The following section will compare the segregation behaviour of these elements

in the ternary and quaternary systems. These comparisons provide insights into Mn-Al, Mn-Mo, and Mn-Si interactions at the interface. A summary of the excess areas and K_{2nm} values for the quaternary samples is included at the end of the section (Table 2).

6.61 Fe-Mn-Al-C

Two alloy compositions were decarburized at 900°C. The compositions were Fe-.94Mn-.94Al-.6C and Fe-1.91Mn-1.81Al-.6C. In every tip tested, manganese and aluminum behaved as they do in their respective ternary systems. This would suggest that there is negligible co-segregation behaviour between manganese and aluminum. The Fe-.94Mn-.94Al-.6C tip had an excess area of 4.8 at%-nm and a K_{2nm} of 3.55 for manganese. The second alloy had two tips tested with significant variation. The excess areas for the two tips were 8.7 at%-nm and 4.2 at%-nm, giving a K_{2nm} of 3.3 and 2.1 respectively for manganese. This variation within the same interface is further evidence of variations of the solute content along the interface. Due to the variation, it is unclear whether or not the difference in composition had a significant influence on segregation. Another observation is that manganese segregation does not appear to be affected by the change in temperature. The 125°C increase from the ternary decarburization temperature has not had a significant impact on the segregation levels. Through comparison of the ternary and quaternary APT results, a significant Mn-Al interaction can be ruled out.

6.62 Fe-Mn-Mo-C

Similar to the previous alloy system, manganese and molybdenum maintained the same behaviour in the ternary and quarternary systems. The Fe-1.36Mn-.42Mo-.48C alloy was decarburized at 775°C for 23.5 min, 120 min, and 240 min. The average excess areas for manganese and molybdenum were 5.51 at%-nm and 4.86 at%-nm respectively. These excess areas correspond to K_{2nm} values of 2.9 for manganese and 10.9 for molybdenum. The degree of segregation is comparable to the ternary alloys. The continued strong segregation of both elements suggests that either site availability is not a limiting factor for their segregation or that these elements do not segregate to the same sites.

While the average segregation values were consistent with the ternary systems, there was significant variation in the data. For each sample, two tips were investigated. Both the 23.5 min and 120 min samples had higher manganese and molybdenum segregation present, along with significant variation between the two tips. In the 23.5 min sample, molybdenum in tip “A” had an excess area of 7.7 at%-nm while tip “B” had 5.2 at%-nm (Figure 48). Similarly, the manganese had an excess area of 7.3 at%-nm in tip “A” while tip “B” had 4.7 at%-nm (Figure 49). Although the segregation peaks for both tips are nearly identical for both elements, tip A has a significantly broader profile, providing a higher excess area (Figure 48Figure 49). This is further evidence of interface inhomogeneity. The 240 min sample had consistently low segregation values with average excess areas of 4.1 at%-nm for manganese and 1.8 at%-nm for molybdenum. It is often thought that a slower interface should have greater segregation, so this result was contrary to predictions.

However, it was previously mentioned that the true velocity of the interface cannot be confidently known because of the argon purge and quench. The velocity of this interface could have actually been higher than the other two samples and thus given lower segregation values. Another possibility is simply that these two tips were taken from an area of low segregation. The previous two samples showed significant variation between individual tips and it is entirely possible that the two tips selected for the 240 min sample had lower than average segregation for that interface.

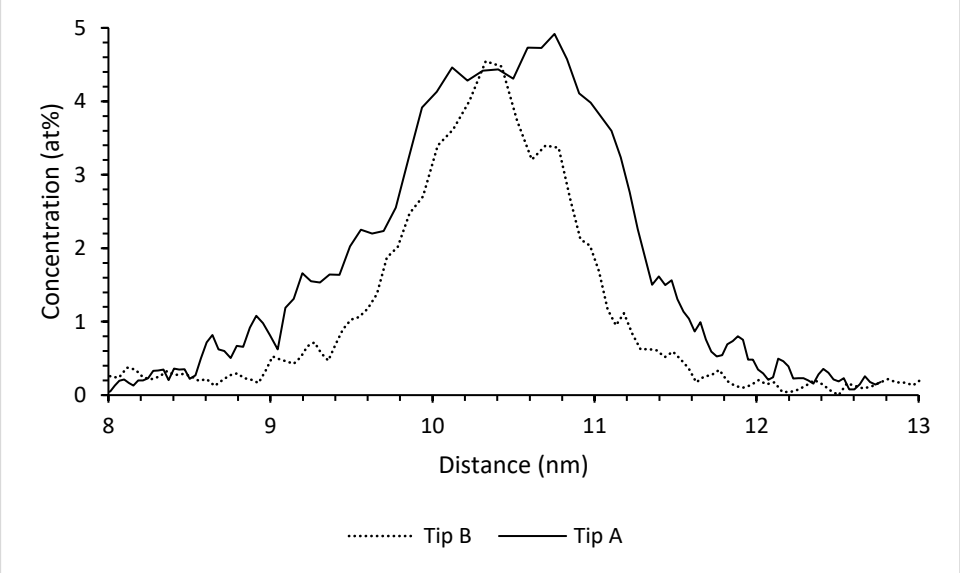

Figure 48: Comparison of molybdenum segregation at 23.5 min in tips A and B.

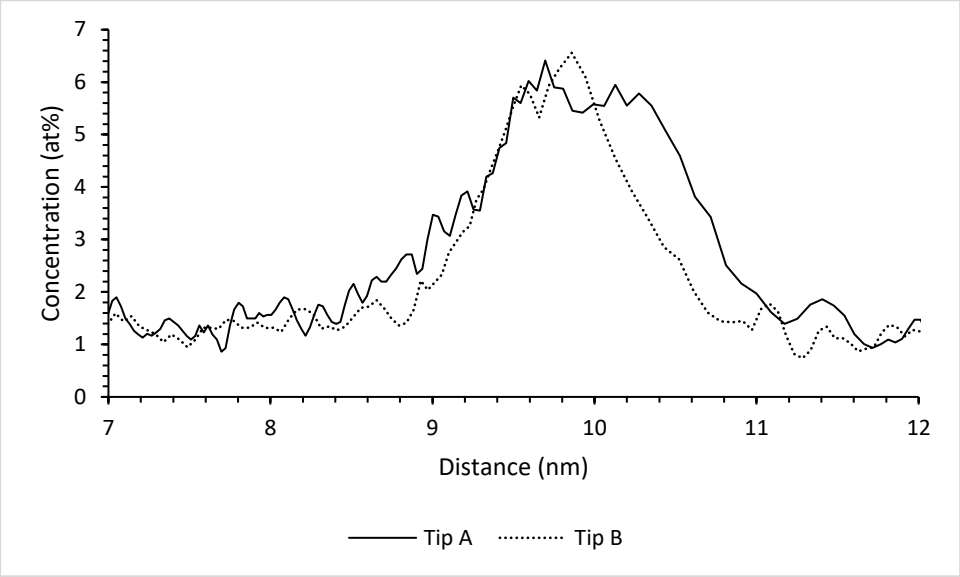

Figure 49: Comparison of manganese segregation at 23.5 min in tips A and B.

Interestingly, all six tips tested showed a positive correlation between manganese and molybdenum segregation (Figure 50). If manganese and molybdenum had an affinity toward each other, a correlation in segregation would also be expected. However, if there was an attraction between manganese and molybdenum, it should generally cause greater segregation than in the ternaries. This is not present in the data, so it is more likely that their segregation is dependent on another common factor. It was previously mentioned in the Fe-Mn-C section that researchers suspected that manganese segregation is due to an attraction to carbon at the interface. Molybdenum is a strong carbide former and could have an affinity to carbon at the interface as well. An alternative to a Mo-C interaction would be a Mo-interface (Mo-I) interaction. Molybdenum may have an affinity to the interface in similar manner to carbon. If the interfacial conditions alter the molybdenum and carbon's degree of attraction, then the segregation of all three

elements would change. Similarly, if there was a variation in the velocity along the interface, it could alter the extent of segregation. Regardless of which mode causes the molybdenum and manganese correlation, it can be concluded that there is a negligible Mn-Mo interaction and that they are both affected by interface inhomogeneity.

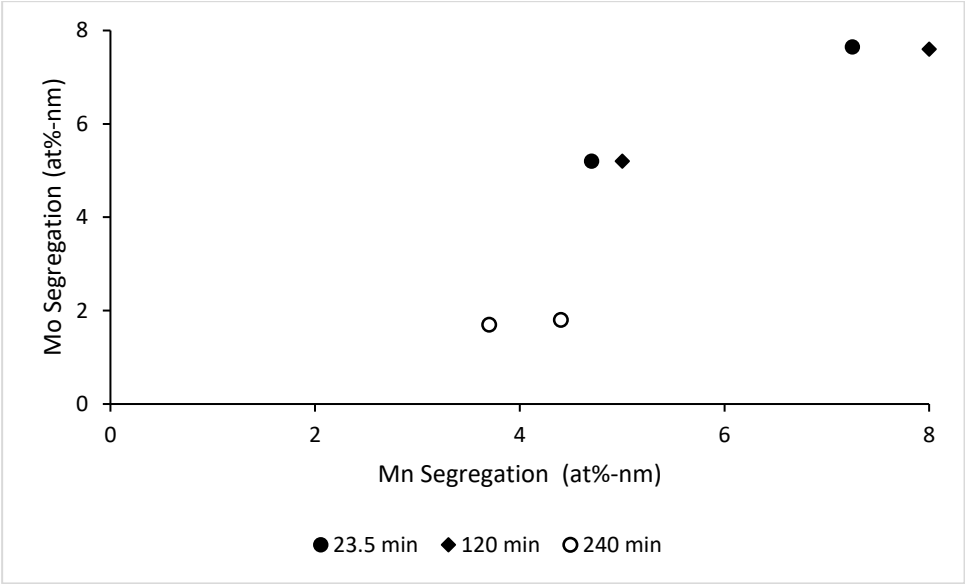

Figure 50: Excess areas of manganese and molybdenum in the Fe-Mn-Mo-C samples.

6.63 Fe-Mn-Si-C

Three decarburized Fe-Mn-Si-C alloys had interfaces investigated for segregation. The Fe-1.5Mn-1.3Si-.66C and Fe-1.0Mn-.9Si-.68C alloys both had ferrite precipitation ahead of the interface. The exact cause of this precipitation is uncertain, but it may be linked to the 240 min decarburization time. If the carbon concentration ahead of these interfaces were below the LENP limit, precipitation would be favourable. The interface would also need to be sufficiently slow, so that the incubation period for precipitation is completed before the region is consumed by the approaching interface. No precipitation was found in the

Fe-1.55Mn-1.5Si-.67C samples, but this can be reasonably explained by its longest decarburization being 32 min. This shorter decarburization time allowed for a greater velocity that should prevent precipitation ahead of the interface. Interfaces with precipitation ahead of them will not be used to analyze the possible interactions taking place between the alloying elements. This exclusion was exercised because the precipitation adds uncertainty to the interfacial conditions, as an orientation relationship could exist between the ferrite and austenite. Therefore, the interfaces without precipitates will be analyzed separately.

The Fe-1.5Mn-1.3Si-.66C and Fe-1.0Mn-.9Si-.68C alloys had some of the highest manganese segregation values with excess areas of 8.6at%-nm and 7.7at%-nm, respectively. These produced K_{2nm} values of 3.9 and 4.8, which surpass the segregation values found in the ternary system. The apparent increase in manganese segregation is assumed to be linked to the precipitation ahead of the interface. While the interface formed during decarburization is thought to be negligibly affected by crystallographic orientation, this is not necessarily shared by the interface of a precipitate. The precipitate may grow preferentially along certain orientations which in turn may alter the structure of the interface. This altered structure could then affect the relative affinities of elements toward the interface.

The Fe-1.55Mn-1.5Si-.67C had four tips tested. Three were decarburized for 32 min while the other was decarburized for 16 min. Manganese continued to segregate with an

average excess area of 4.19 at%-nm, giving a K_{2nm} of 2.4. The manganese segregation appears to be less than in the ternary, but this cannot be stated with certainty due to the previously observed variation in segregation. However, silicon has a pronounced change in behaviour in the quaternary alloy. It has shifted from inconsistent desegregation to inconsistent segregation. Three out of four tips tested showed minor silicon segregation, while the fourth had a flat concentration profile. The average excess area for silicon is 1.6 at%-nm, giving a K_{2nm} of 1.3. The reason for the altered behaviour of silicon is theorized to be an attractive Mn-Si interaction. It is assumed from the ternary systems that manganese is attracted to carbon whereas silicon is repelled by carbon. The interactions between these three elements would make the segregation difficult to intuitively predict. For example, if carbon were to increase at the interface, manganese should also increase. Silicon would clearly be more attracted to the interface with the manganese present than it would be in the ternary and may segregate. This excess of silicon would then have a repulsive interaction with carbon, thus decreasing the carbon at the interface. The decrease of carbon could also lead to a decrease in manganese. The segregation values of the three elements would depend on the strength of the Mn-Si, Mn-C, and Si-C interactions as well as the kinetics of solute segregation to the interface. The general behaviour would be that silicon would have an increased presence at the interface in this quaternary system and carbon would have a decreased presence. The manganese segregation could shift, depending on whether it is more attracted to carbon or silicon. The present APT data suggests that manganese segregates similarly or slightly less than in

the ternary system. In conclusion, the altered behaviour of silicon provides support for an attractive Mn-Si interaction.

Table 2: Segregation values for quaternary APT samples.

Composition (wt%)	Temperature (°C)	Time (min)	Excess Area Mn (at%-nm)	K_{2nm} Mn	Excess Area Y (at%-nm)	K_{2nm} Y
Fe-1.91Mn-1.81Al-.6C (A)	900	17	8.7	3.3	0	1
Fe-1.91Mn-1.81Al-.6C (B)	900	17	4.2	2.1	0	1
Fe-.94Mn-.94Al-.6C	900	17	4.8	3.7	0	1
Fe-1.55Mn-1.5Si-.67C	755	16	3.4	2.1	1.0	1.2
Fe-1.55Mn-1.5Si-.67C (A)	755	32	3.3	2.1	1.5	1.3
Fe-1.55Mn-1.5Si-.67C (B)	755	32	5.0	2.7	3.9	1.7
Fe-1.55Mn-1.5Si-.67C (C)	755	32	4.9	2.6	0	1
Fe-1.5Mn-1.3Si-.66C	755	240	8.6	3.9	1.3	1.3
Fe-1.0Mn-.9Si-.68C (A)	755	240	8.2	5.1	0	1
Fe-1.0Mn-.9Si-.68C (B)	755	240	7.2	4.6	0	1
Fe-1.36Mn-.42Mo-.48C (A)	775	23.5	7.3	3.5	7.7	16.6
Fe-1.36Mn-.42Mo-.48C (B)	775	23.5	4.7	2.6	5.2	11.6
Fe-1.36Mn-.42Mo-.48C (A)	775	120	8.0	3.8	7.6	16.5
Fe-1.36Mn-.42Mo-.48C (B)	775	120	5.0	2.7	5.2	11.6
Fe-1.36Mn-.42Mo-.48C (A)	775	240	4.4	2.5	1.8	4.7
Fe-1.36Mn-.42Mo-.48C (B)	775	240	3.7	2.3	1.7	4.5

7.0 Modelling Results and Discussion

A challenge arose while attempting to use the APT data to model the ternary systems. Initially, the binding energies of the various elements to the interface were to be extracted from the APT results. The BE of an element to the interface is often calculated using EQ.23:

$$K = \frac{C_{max}}{C_0} = e^{\frac{-BE}{RT}} \qquad (23)$$

The K value is needed to calculate BE. C_{max}, the peak segregation concentration at the interface, is needed to calculate K. As previously stated, the peak concentration of the APT profile cannot be reliably determined. While the excess area can be used to recreate the concentration profile, the shape of the profile remains unknown. The 2 nm rectangle used to calculate the K_{2nm} values was arbitrarily chosen and should not be used to calculate BE. The BE is dependent on the shape of the concentration profile and therefore the BE cannot be accurately calculated. Therefore, BEs calculated from the APT results will not be used in modelling the ternary systems. Instead, the BE used in modelling will qualitatively reflect the segregation behaviour of the element in the APT results.

Manganese, molybdenum, and carbon consistently segregated to the interface in the ternary systems. It is reasonable to assume that all three have net negative (attractive) BE to the interface. Manganese and molybdenum should contribute to the energy dissipation at the interface and slow the growth of the ferrite. Carbon segregation does not directly affect the energy dissipation at the interface as binary Fe-C kinetics do not significantly deviate from LENP predictions. Carbon can affect energy dissipation indirectly by affecting

the BEs of other elements at the interface. The influence of carbon on energy dissipation should not be neglected.

Nickel and aluminum showed negligible segregation in the ternary systems. This would suggest a minimal contribution to energy dissipation at the interface. Previous modelling of the Fe-Ni-C system by has shown that the Fe-Ni-C system adheres closely to LENP conditions and thus supports the assumption that nickel does contribute significantly to energy dissipation [21,22]. Difficulties with the kinetic results from the Fe-Al-C and Fe-Mn-Al-C systems were present. Ferrite growth was significantly less than LENP and aluminum oxidation at the interface is assumed to be the cause. The Fe-Al-C and Fe-Mn-Al-C results are discussed fully in Appendix 3.

Silicon was the only element to desegregate in the analyzed ternary systems. This would suggest a net positive (repulsive) BE and this would contribute to energy dissipation. As Cahn et al. [30] suggested, a positive BE would still contribute to slower than expected growth. The inconsistency of the desegregation could be an anomaly and therefore have no impact on energy dissipation. Alternatively, it could be evidence of fluctuations at the interface and the average BE would then be lower.

7.1 Model Parameters

The three-jump model developed by Zurob et al. was used to model the Fe-Mo-C, Fe-Mn-C, and Fe-Si-C systems. The Fe-Al-C system was not modelled due to the quality of the kinetic data and the insufficient thermodynamic data in Thermo-Calc.

The diffusion coefficients for carbon in austenite and ferrite were calculated using equations from Agren et al. [58] with a 20% decrease in the diffusion coefficient of carbon in ferrite above 800^{o}C. This adjustment is due to an overestimation of the diffusivity of carbon in ferrite above the magnetic transition temperature [10,59]. The diffusion coefficients of the substitutional elements were taken from the MOB2 database of DICTRA.

A modified version of austenite phase was used as the boundary phase for the calculations in Thermo-Calc. Two terms that will be used while discussing the modelling results are adjustments and effective binding energies. Adjustments are the modifications made to the boundary phase description to account for the affinity of elements towards the interface. The effective binding energies are calculated in Thermo-Calc and represent the deviation of the chemical potential of X in the boundary phase, with respect to the average chemical potential of X in ferrite and austenite. This effective binding energy is then used to calculate the energy dissipation during the transformation. The adjustments are the choice of the modeller and the effective binding energies results from that choice. As BEs of the elements cannot be conclusively calculated from the APT results, the adjustments to the boundary phase will be used as a fitting parameter. An adjustment would be considered unacceptable if it does not accurately capture the behaviour observed in the APT profiles. To account for the significant carbon segregation observed in the results, a -50 kJ/mol adjustment was made for carbon at the interface. This adjustment was kept constant in all the alloys modelled, as the interaction of carbon at

the interface is assumed to be governed by the reduction of elastic strain energy and not X-C interactions. Adjustments to the Fe-X interaction in the boundary phase were made to account for the affinities that the X elements have towards the interface.

The following section presents the modelling of the Fe-.88Si-.58C, Fe-.51Mo-.54C, and Fe-.94Mn-.57C alloys. These alloys were decarburized and reported by Odqvist et al., Zurob et al., Hutchinson et al., and Enomoto et al. [26,60-62]. PE and LENP predictions are included with the model predictions for each data set. Each plot also contains the model's prediction of the X element concentration at the interface. The adjustments to the boundary phase to account for the substitutional element segregation will be presented along with the effective BE. The effective BE differs from the adjustment as it takes into account factors such as the temperature and the interaction with carbon. The adjustments made to the boundary phase and the resulting effective BEs for each data set modelled are included in Table 3 at the end of the section.

7.2 Fe-Si-C

The ternary Fe-Si-C APT results showed desegregation at the interface. This desegregation should cause energy dissipation and resulted in growth kinetics slower than LENP predictions. The effective BE for silicon should then be large and positive in order to accurately represent its behaviour. The kinetic data from the Fe-.88Si-.58C alloy decarburized at 775°C, 806°C, 825°C, and 850°C was modelled below (Figure 51Figure 52Figure 53Figure 54). As expected, the thickness measurements at each temperature fall

below LENP and PE predictions. Before making adjustments to the BE of silicon, the model predicted a strongly positive effective BE because of the repulsive Si-C interaction. This effective BE predicted slower kinetics than what was experimentally observed. In order to fit the data, an attractive interaction between Si and the interface was introduced for all four temperatures. Therefore, the model predicts that silicon has an attractive interaction with the interface but is repelled by the presence of carbon. As seen in Table 3, the magnitude of the boundary adjustments decreased with increasing temperature, starting at -12 kJ/mol at 775°C and finishing at -6 kJ/mol at 850°C. However, the effective BE did not follow this trend and did not deviate more than 1.1 kJ/mol from the average of +15.9 kJ/mol. This would suggest that the energy dissipation due to silicon does not vary significantly within the 75°C temperature range investigated. Silicon has been successfully modelled by adjusting the Si-I interaction so as to maintain a nearly constant effective BE of approximately +15.9 kJ/mol.

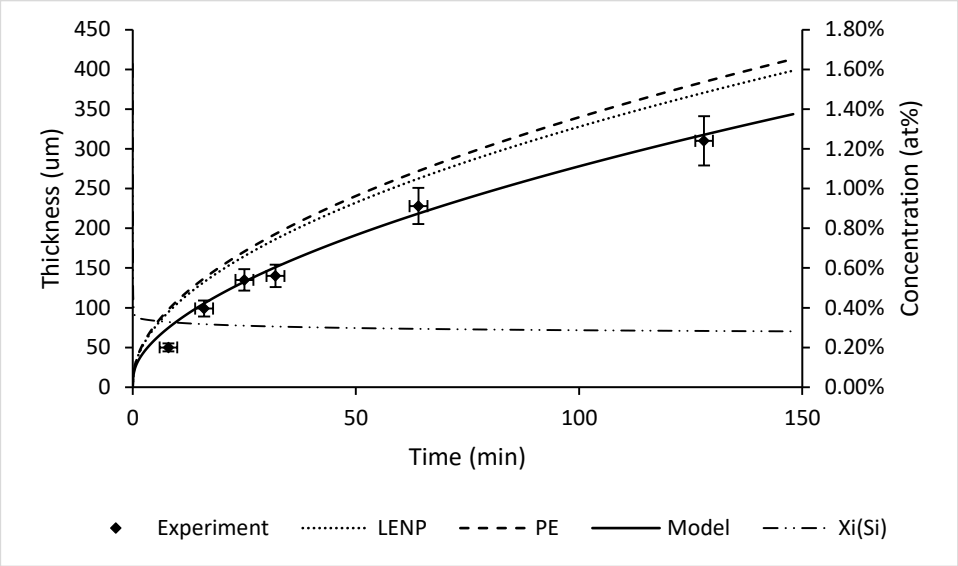

Figure 51: Modelling of Fe-.88Si-.58C decarburized at 775°C.

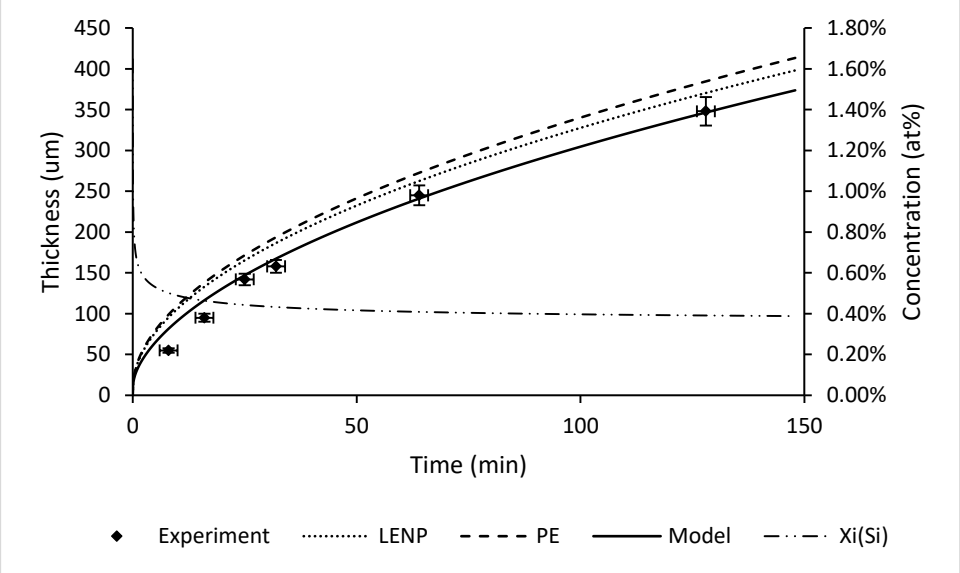

Figure 52: Modelling of Fe-.88Si-.58C decarburized at 806°C.

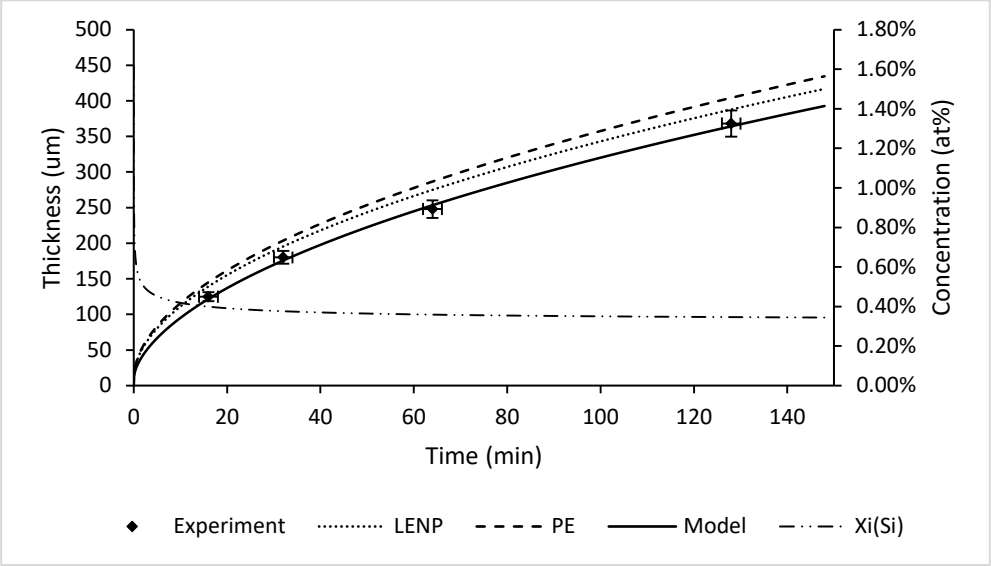

Figure 53: Modelling of Fe-.88Si-.58C decarburized at 825°C.

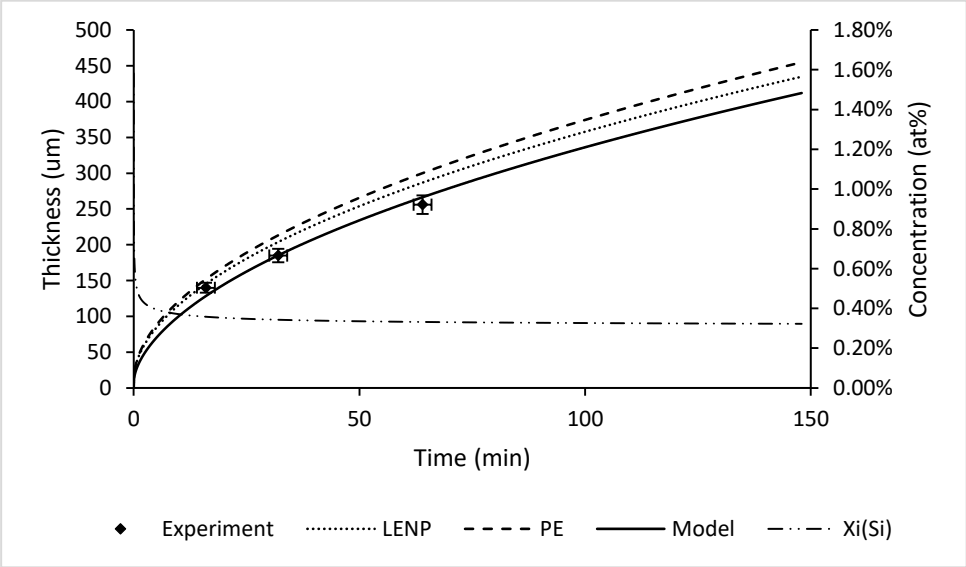

Figure 54: Modelling of Fe-.88Si-.58C decarburized at 850°C.

7.3 Fe-Mo-C

Molybdenum showed a consistent segregation to the interface in both the ternary and quaternary systems. This should correspond to a negative effective BE to the interface

causing energy dissipation during the transformation. The kinetic data is therefore expected to be below PE and LENP predictions. The Fe-.51Mo-.54C was decarburized at temperatures of 775°C, 806°C, and 825°C. The ferrite layer thicknesses were compared to PE, LENP, and model predictions (Figure 55Figure 56Figure 57). The PE and LENP carbon contact conditions were nearly identical for this alloy and so average concentrations were used instead. As expected, the experimental data fell below the PE/LENP predictions and it is assumed that energy dissipation was the cause. The molybdenum interaction at the boundary was adjusted to account for the segregation observed in the APT results. The adjustments for molybdenum at 775°C, 806°C, and 825°C are: -16 kJ/mol, -16 kJ/mol, and -20 kJ/mol respectively. These adjustments produced effective BEs of -20.6 kJ/mol, -19.1 kJ/mol, and -21.3 kJ/mol. Similar to the Fe-Si-C modelling, the effective BEs did not deviate significantly from their average of -20.3 kJ/mol. Temperature does not appear to be a significant factor in determining the effective BEs for molybdenum in this range. If the effective BE does not vary significantly with temperature, the segregation should vary slightly with temperature to balance EQ.23. Molybdenum has been successfully modelled by making negative adjustments in order to keep the effective BE near the average of -20.3 kJ/mol.

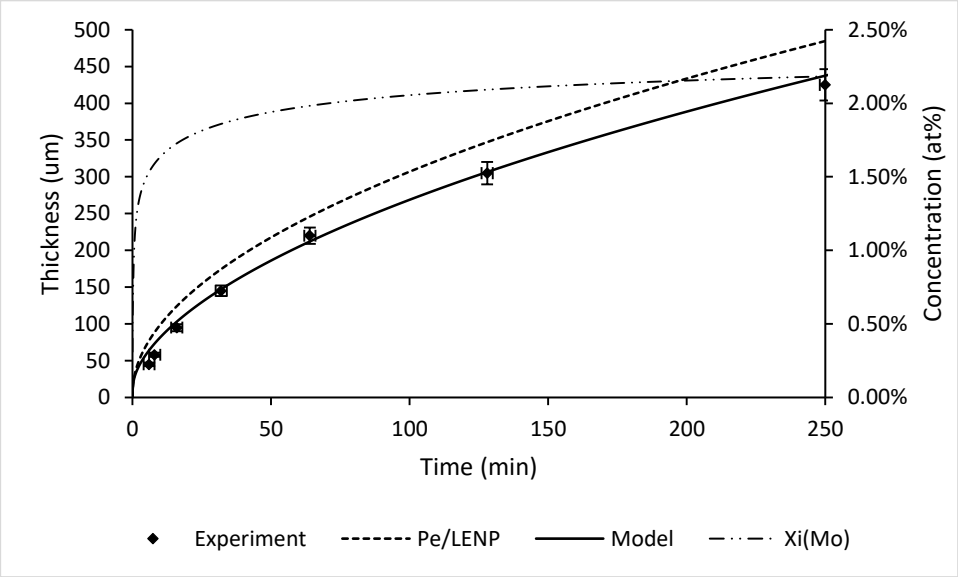

Figure 55: Modelling of Fe-.51Mo-.54C decarburized at 775°C.

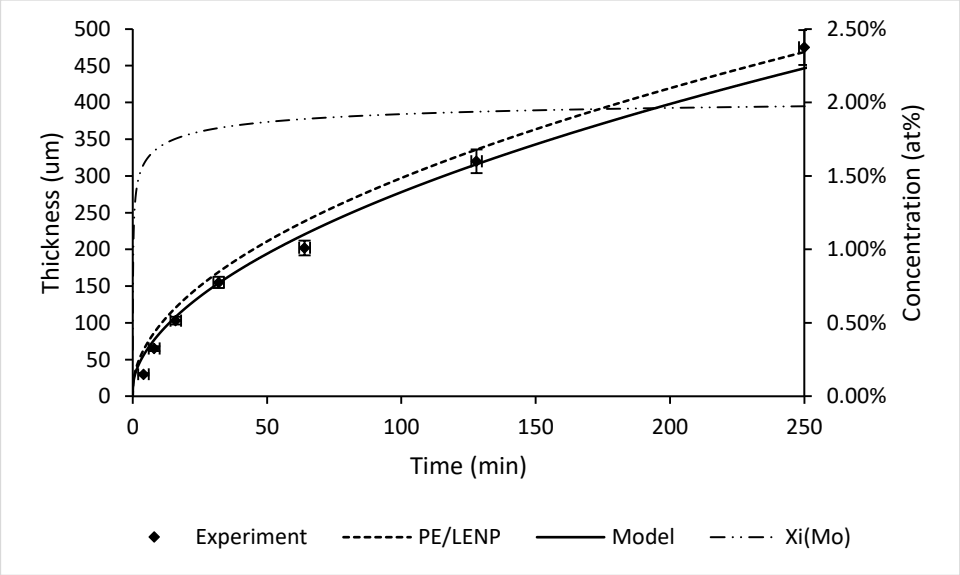

Figure 56: Modelling of Fe-.51Mo-.54C decarburized at 806°C.

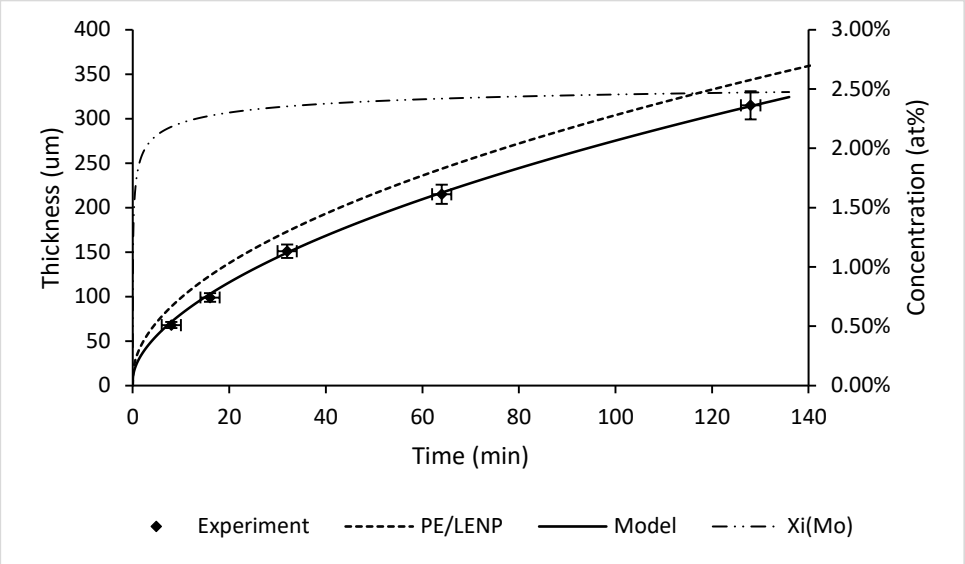

Figure 57: Modelling of Fe-.51Mo-.54C decarburized at 825°C.

7.4 Fe-Mn-C

The Fe-.94Mn-.57C alloy is the final alloy that was modelled. The APT results consistently showed strong manganese segregation to the interface in the ternary and quaternary systems. Like molybdenum, manganese should have a negative BE that would produce energy dissipation. This dissipation would then slow the growth of ferrite below the LENP and PE predictions. Samples were decarburized at 755°C, 775°C, 806°C, and 825°C. The data from these experiments were plotted along with PE, LENP, and model predictions (Figure 58Figure 59Figure 60Figure 61). As previously noted, the thermodynamic description for manganese in ferrite was modified, as suggested Zurob et al. [25]. The original thermodynamic description is thought to underestimate carbon solubility in ferrite at elevated temperatures [25]. The original description puts the experimental data between the PE and LENP predictions [23], whereas the modified description has the

experimental data below the LENP predictions. The modified description appears to align the behaviour of the Fe-Mn-C system with that of the other alloys. Each data set falls below the LENP predictions, as expected if manganese contributed to energy dissipation. The model had difficulty with the Fe-Mn-C system. The difficulty lies in the low carbon solubility in ferrite. If the boundary adjustment of manganese was too large, carbon contact conditions could not be calculated for all velocities. As energy dissipation increases, the carbon concentration in the austenite adjusts to satisfy the zero driving force assumption. If the energy dissipation is too high, the carbon concentration may not be adjusted enough to account for the dissipation. In this case, the model would not be able to complete the calculations. The boundary adjustments at temperatures of 775°C and above were chosen not because they produced the best fit, but because they were the highest allowable adjustment that the model could withstand. This limited the energy dissipation that could be produced by the manganese and the model overestimated the ferrite growth, especially at 825°C. The model fit the data best at 755°C and 775°C with a boundary adjustment of -8 kJ/mol and -9 kJ/mol respectively. This produced an effective BE of -8.9 kJ/mol for both temperatures. It is assumed that the average effective BE for manganese would be near -8.9 kJ/mol if greater boundary adjustments could be performed at 806°C and 825°C. Limited success was attained in modelling due to the inability of the Fe-Mn-C system to handle greater degrees of energy dissipation. If this issue did not arise, it is reasonably assumed that the effective BEs would follow a similar pattern to silicon and molybdenum.

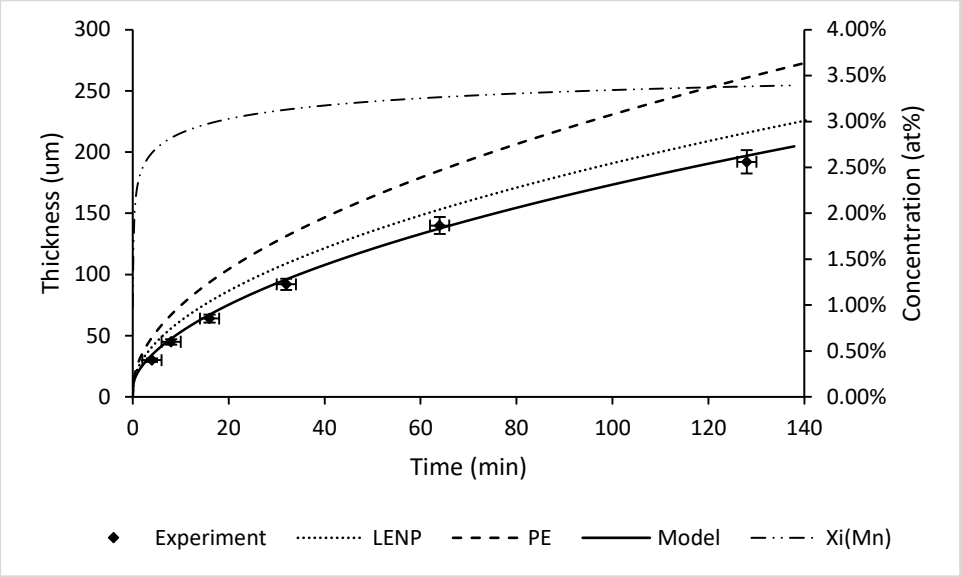

Figure 58: Modelling of Fe-.94Mn-.57C decarburized at 755°C.

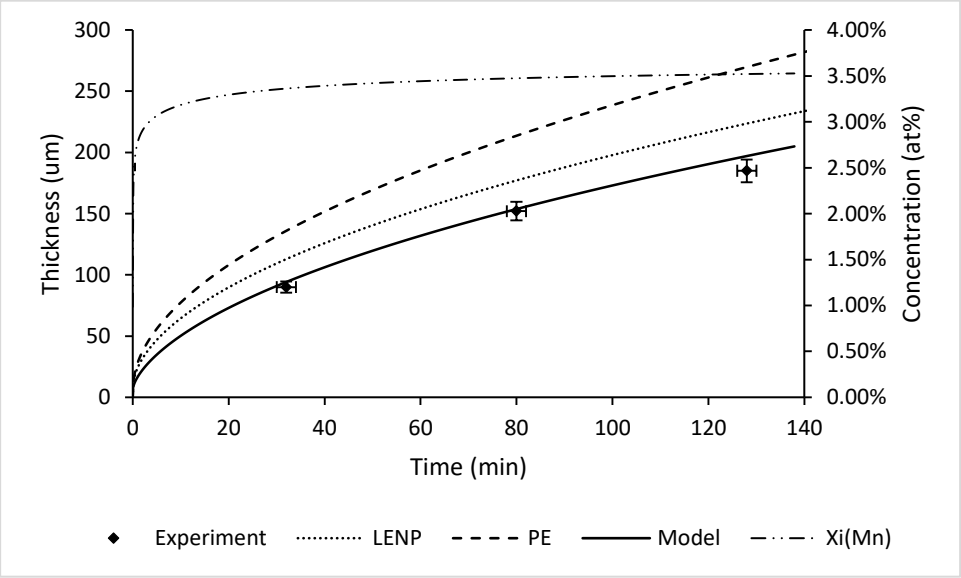

Figure 59: Modelling of Fe-.94Mn-.57C decarburized at 775°C.

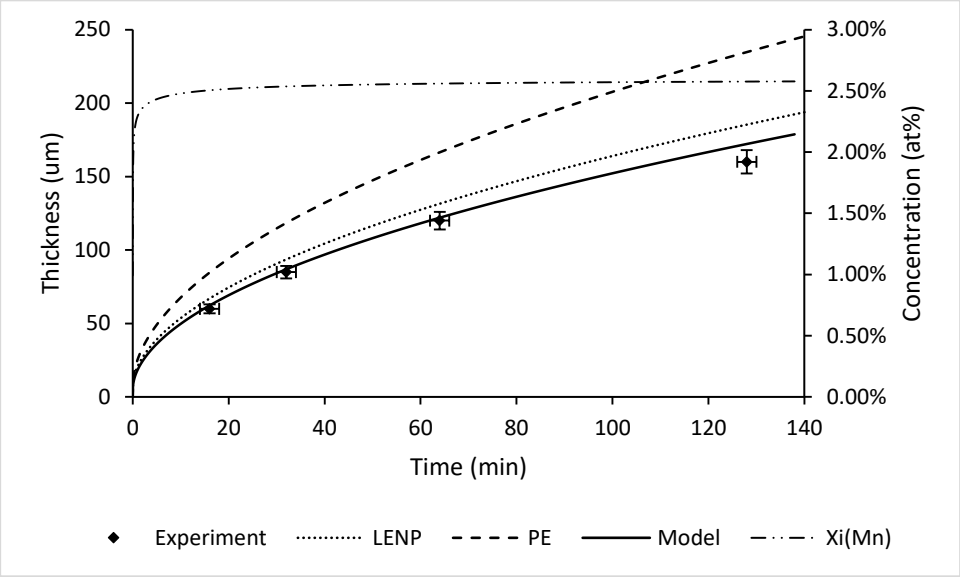

Figure 60: Modelling of Fe-.94Mn-.57C decarburized at 806°C.

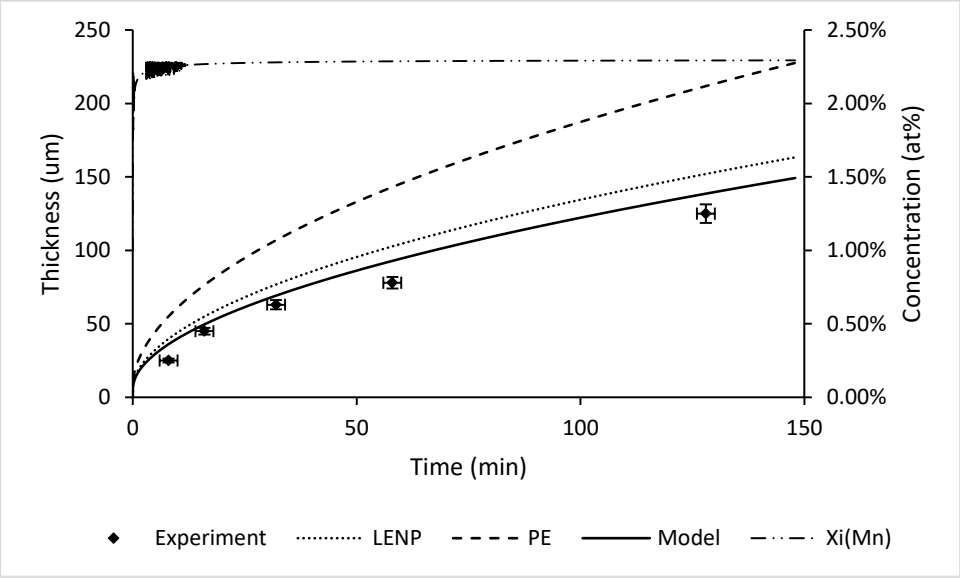

Figure 61: Modelling of Fe-.94Mn-.57C decarburized at 825°C.

Table 3: Summary of ternary boundary adjustments and resultant effective BEs.

Composition (wt%)	Temperature (°C)	Effective BE (kJ/mol)	Boundary Adjustment (kJ/mol)
Fe-.88Si-.58C	775	+17.1	-11
Fe-.88Si-.58C	806	+14.7	-12
Fe-.88Si-.58C	825	+15.8	-9
Fe-.88Si-.58C	850	+16.0	-6
Fe-.51Mo-.54C	775	-20.6	-16
Fe-.51Mo-.54C	806	-19.1	-16
Fe-.51Mo-.54C	825	-21.3	-20
Fe-.94Mn-.57C	755	-8.9	-8
Fe-.94Mn-.57C	775	-8.9	-9
Fe-.94Mn-.57C	806	-5.4	-6
Fe-.94Mn-.57C	825	-3.8	-5

7.5 Quaternary Implications

As manganese provided issues in modelling in the ternary, the quaternary systems were not extensively modelled. However, the kinetic implications of the quaternary APT results will be discussed for the Fe-Mn-Mo-C and Fe-Mn-Si-C systems. The Fe-Mn-Al-C system is discussed in the Appendix 3.

7.51 Fe-Mn-Mo-C

The APT results for manganese and molybdenum revealed a strong and consistent segregation behaviour. The average segregation amounts for both elements in the Fe-Mn-Mo-C alloy were comparable to the amounts observed in their respective ternary alloys. This led to the conclusion that a significant Mn-Mo interaction does not exist. If the segregation has a negligible change, the energy dissipation contribution from each

element should also negligibly change. Therefore, the APT results predict that the ternary energy dissipation values could also be used to model the quaternary system.

Sun et al. attempted to model the Fe-Mn-Mo-C system using the three-jump model [63]. They were able to successfully model the experimental data from controlled decarburization experiments using the ternary values for energy dissipation. This modelling work fits the prediction made from the APT results. It should be noted that this behaviour in the Fe-Mn-Mo-C is not necessarily true for all quaternary systems. It would be quite convenient if the behaviour of an element remains consistent, regardless of the addition of other alloying elements. Then ternary experiments would provide sufficient information to model the multi-component systems. However, this does not appear to be the case, as observed in the Fe-Mn-Si-C system.

7.52 Fe-Mn-Si-C

Investigations of interfaces from Fe-Mn-Si-C alloys revealed manganese segregation consistent with the observed segregation in the ternary system. Although manganese had greater segregation levels at the interface of samples that had ferrite precipitation ahead of the interface, these were not included in the analysis for the reasons previously stated in section 6.63. The silicon in the quaternary system had a significant departure from the ternary desegregation. Instead of desegregation, silicon showed minor segregation in the quaternary APT results. The K_{2nm} changed from 0.5 in the ternary to 1.3 in the quaternary. Both behaviours should produce energy dissipation during the transformation, but it

should be more pronounced in the ternary system as the desegregation was more extensive than the segregation observed in the quaternary system. Manganese did not significantly differ in the ternary and quaternary system so the energy dissipation should behave in like manner. Therefore, the APT results lead to the prediction that energy dissipation should be less than the addition of silicon and manganese ternary contributions and greater than the manganese ternary contribution.

Qiu et al. sought to model the Fe-Mn-Si-C system using the three-jump model [64]. They were unsuccessful in accurately modelling the system using the manganese and silicon adjustments from the ternary systems. The ternary values overestimated energy dissipation, just as the APT results predicted. They then removed the Mn-Si interaction in the thermodynamic description of the boundary to improve the agreement between the model and the experimental data. This would suggest that manganese and silicon have no interaction at the interface. As previously discussed, it is reasonably assumed that the Mn-Si interaction is the cause of the drastic change in the segregation behaviour of silicon. Removal of the Mn-Si interaction would not accurately represent the segregation behaviour observed. An issue that might have been an obstacle in modelling the Fe-Mn-Si-C system is the Mn-C thermodynamic description. The Si-C interaction is evident in Thermo-Calc as a -11 kJ/mol silicon adjustment and a -50 kJ/mol carbon adjustment at 775°C produces an effective BE of +17.1 kJ/mol for silicon. Clearly the carbon adjustment significantly affects the effective BE of silicon. It is assumed that manganese segregates because of an attraction to carbon, yet a -9 kJ/mol adjustment of manganese and the

same -50kJ/mol adjustment of carbon at 775°C produces an effective BE of -8.9 kJ/mol. The influence of carbon on the effective BE of manganese appears to be minimal. Manganese and carbon do not appear to be coupled as the effective BE comes primarily from the adjustment of manganese, not carbon, unlike in the case of silicon where the effective BE was significantly affected by carbon. If a complex relationship between Mn-C, Si-C, and Mn-Si interactions is taking place at the interface, it is no surprise that an incorrect description of the Mn-C interaction would lead to incorrect effective BEs. The effective BE for silicon would be overstated if the Mn-C interaction is understated as this alters the balance between the Mn-C, Si-C, and Mn-Si interactions. This overstatement is evident as the model predicted the interfacial silicon concentration should increase to more than double the bulk concentration [64]. The effective BE of silicon should have been much lower to match the minor segregation observed using APT. If there are inaccuracies in the thermodynamic descriptions, the adjustments made while modelling the ternary systems not only represent adjusting for BE, but also compensating for the inaccuracies. As shown in the work by Qiu et al., the ternary adjustments were not adequate in compensating for the inaccuracies in the quaternary system. If the error comes from the thermodynamic descriptions, there is hope that modelling using the ternary adjustments is still feasible in multi-component systems that exhibit co-segregation.

8.0 Conclusions

Ternary Fe-X-C and quaternary Fe-Mn-Y-C systems were investigated to study the interfacial segregation during isothermal ferrite growth. Controlled decarburization experiments produced planar ferrite interfaces that were subsequently studied using APT.

The excess area under each segregation profile was used to quantify the segregation present at the interface. This was done to mitigate the influence of factors such as artefacts and interfacial roughness. The K_{2nm} values were also calculated to normalize the excess area to the bulk concentration. Carbon was not analyzed in detail because its greater diffusivity and artefacts could not be mitigated sufficiently.

APT results revealed strong manganese, molybdenum, and carbon segregation in the ternary systems. Aluminum had a negligible interaction with the interface in the ternary system. Silicon inconsistently desegregated in the ternary system [42].

The Fe-Ni diffusion couple surpassed the LENP limit for ferrite growth and it is thought that only a partial LENP spike must have been present to surpass the LENP limit. APT showed slight segregation in samples with longer decarburization time. This segregation is assumed to be a partial nickel spike rather than segregation to the interface.

In the Fe-Mn-Mo-C system, manganese and molybdenum segregated in comparable amounts to their ternary systems. This was also the case for the Fe-Mn-Al-C system. This led to the conclusion that the Mn-Mo and Mn-Al interactions are negligible at the

interface. In contrast, silicon started to weakly segregate in the Fe-Mn-Si-C system. It was proposed that there exists a non-negligible, attractive Mn-Si interaction at the interface.

Three ternary systems were modelled using the three-jump-model developed by Zurob et al. Binding energies for the silicon, molybdenum, and manganese were adjusted in agreement with their segregation behaviour observed in the APT results. These adjustments allowed for the satisfactorily modelling of the experimental results.

The APT data provided insight into the modelling results for the Fe-Mn-Mo-C system by Sun et al. and for the Fe-Mn-Si-C system by Qiu et al. The Fe-Mn-Mo-C system was satisfactorily modelled by Sun et al. while using the ternary binding energies because the Mn-Mo interaction is negligible. There was difficulty in modelling the Fe-Mn-Si-C system by Qiu et al. while using the ternary binding energies because the Mn-Si interaction is non-negligible. Modelling multi-component systems may still be possible while using ternary binding energy adjustments if satisfactorily accurate thermodynamic descriptions are available.

Appendix 1: TEM-EELS Data

EELS was also conducted on the 23.5 min Fe-1.36Mn-.42Mo-.48C sample. The TEM foil contained the ferrite/austenite interface, along with a ferrite grain boundary (Figure 62). Manganese and carbon segregation were detected at the interface (Figure 63). The manganese and carbon EELS results were comparable to the APT results (Figure 64). However, molybdenum segregation was not observed. Even at 4 at%, EELS has difficulties with accurately reporting element concentrations. For this reason, neither molybdenum segregation was not observed nor carbon away from the interface, unlike in the APT results. This limits the effectiveness of EELS in segregation studies. No segregation was found at the ferrite grain boundary. However, segregation is relatively difficult to detect with EELS so there may still be segregation present.

Figure 62: TEM image of the ferrite/austenite interface.

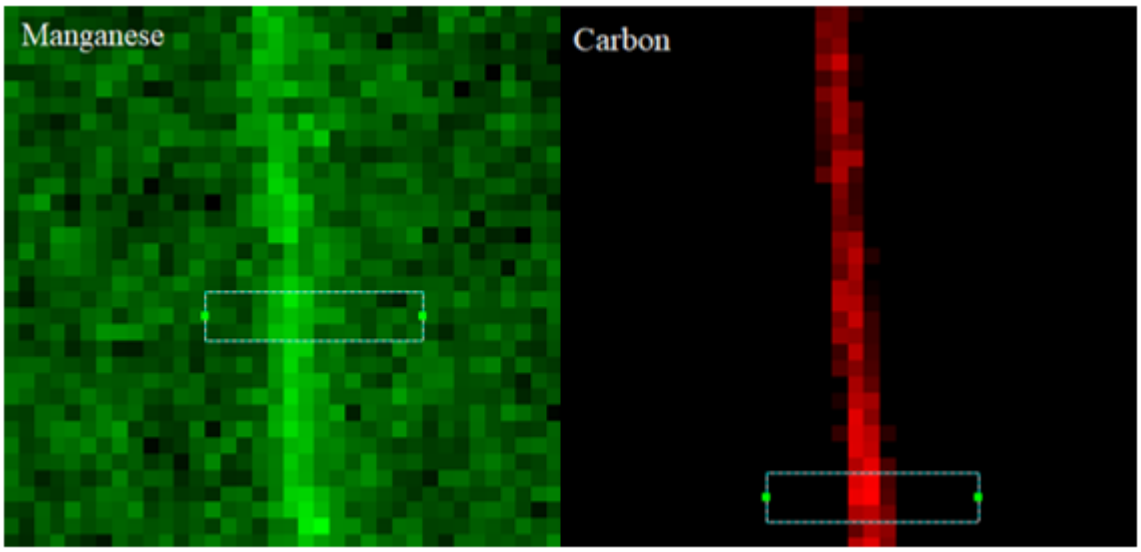

Figure 63: EELS map of the interface for manganese (left) and carbon (right).

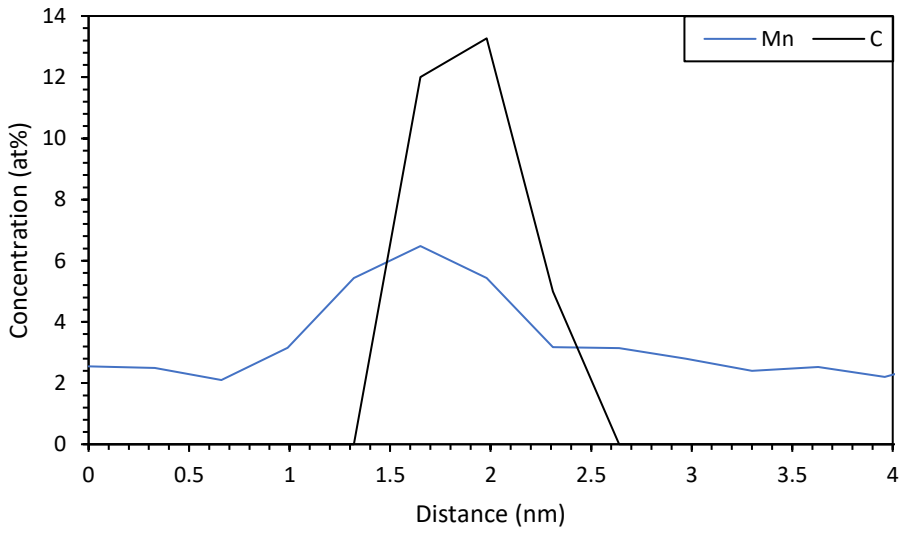

Figure 64: EELS concentration profile across the interface.

Appendix 2: The Effect of Element Concentration on Segregation

The effect that a marginal change in composition has on the segregation of that element is uncertain. A visualization of how the excess area and K value may change with concentration has been provided (Figure 65). It is clear that in the extremely dilute case, a segregating element would have an inflated K_{2nm} and a small excess area due to the limited availability of the element in the bulk. As the composition increases, the excess area would increase also and K_{2nm} values would deflate as composition is no longer miniscule. It may enter a stable region where excess area continues to increase and K_{2nm} remains relatively constant. This may be the region where much of the manganese data is. The composition does appear to have a significant impact on K_{2nm} although excess area may increase. Such is the case in the Fe-Al-Mn-C alloys where manganese concentrations had values of 0.94 wt% and 1.89 wt%. As the composition continues to arise, the availability of segregation sites may become the limiting factor. The excess area would eventually peak and then begin to decline. Although the number of available or favourable sites may remain unchanged in amount, as the concentration increases, the atoms already present at the interface may go to the available sites rather than the excess atoms. The composition would eventually reach a point where segregation is negligible at the interface.

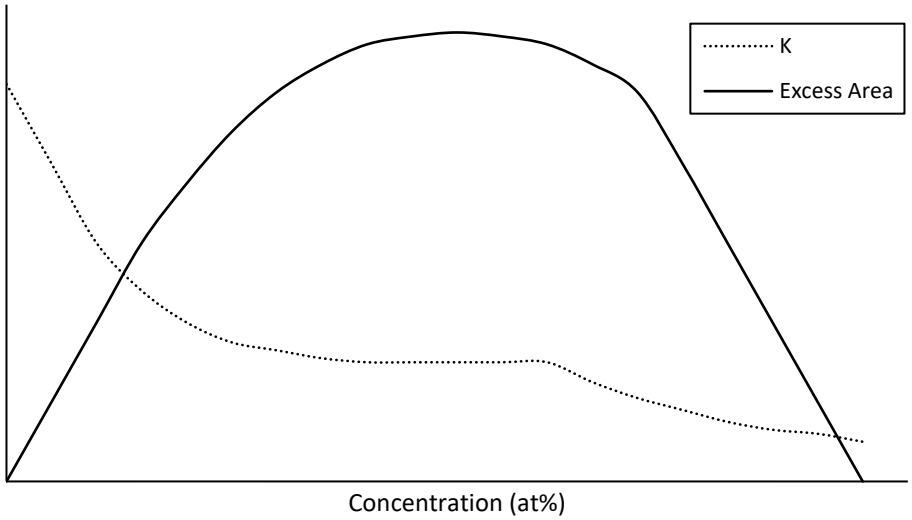

Figure 65: Visualization of proposed relationship between segregation and concentration.

Appendix 3: Fe-Al-C and Fe-Mn-Al-C Modelling Results

The kinetic results for the Fe-Al-C system were unexpected. Thickness measurements fell below the LENP predictions even though aluminum negligibly interacts with the interface (Figure 66). There are several factors that could explain the unexpected result. The first is that alumina formed on the surface of the sample. This oxide layer could have limited decarburization and could cause slower kinetic results. Another factor could be that aluminum may interact with the interface, but it simply was not observed in the APT results. It is a possibility but is unlikely that it was not observed in the six tips tested from the Fe-Al-C and Fe-Mn-Al-C systems. Lastly, the LENP conditions may be unsatisfactory. The thermodynamic descriptions for aluminum do not appear to be satisfactory in in Thermo-Calc and would lead to incorrect contact conditions at the interface. These potential issues with the Fe-Al-C system would also be extended to the Fe-Mn-Al-C system as well.

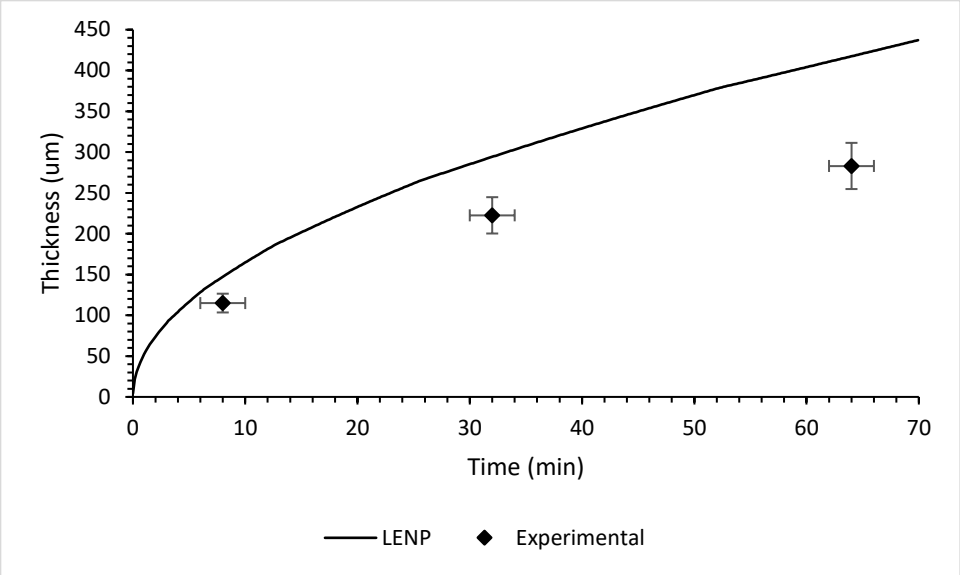

Figure 66: Comparison of the decarburization results for Fe-1.0Al-0.6C at 900°C and the LENP predictions.

Appendix 4: Silicon Segregation in an Fe-Mn-Mo-C Sample

The greatest extent of silicon segregation observed was in the Fe-1.36Mn-.42Mo-.48C sample. It was only present in one tip from the 23.5 min sample (Figure 67). Even in that tip, it was only present in a quarter of that interface. Although it is a trace element with a concentration of 0.08 at%, silicon peaked at 5 at% at the interface. It had an excess area of 7.6 at%-nm and a K_{2nm} of 42. This significant segregation considering that silicon is a trace element in the bulk. It is unlikely that this would significantly affect the transformation kinetics as the segregation is only in a quarter of one tip when six were tested. This is another example of interface inhomogeneity. This provides more evidence that silicon is willing to segregate to the interface, but it is dependent on the conditions at the interface. It may also be evidence of a Mo-Si interaction but with limited sample size, conclusions should not yet be drawn.

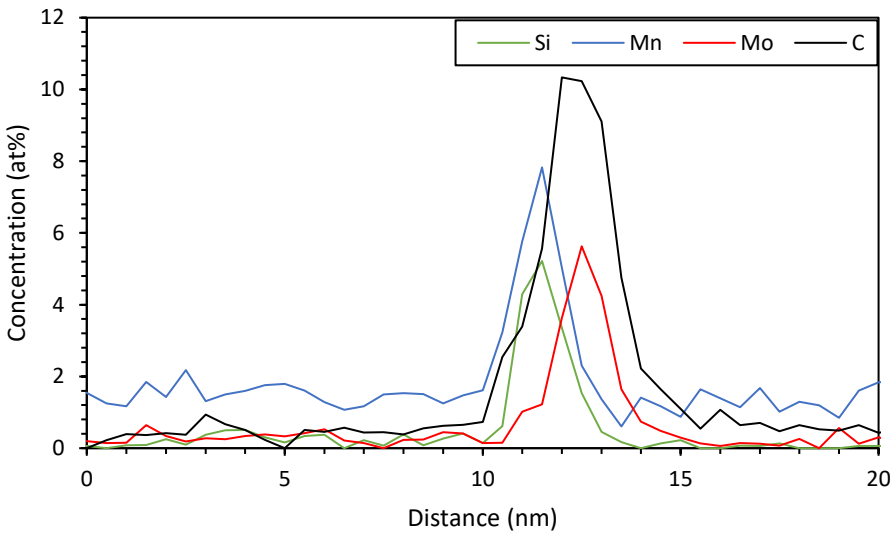

Figure 67: APT profile of the Fe-1.36Mn-.42Mo.48C alloy decarburized at 755°C for 23.5 min with high silicon. (Tip A)

References

[1] H.K.D.H. Bhadeshia, (1985). Prog. Mater. Sci., 321-386.

[2] M. Hillert, (2007). Phase Equilibria, Phase Diagrams and Phase Transformations: Their Thermodynamic Basis. Cambridge University Press.

[3] M. Hillert, (1969). Institute of Metals Monograph, 231-247.

[4] M. Hillert, (1975). Met. Trans. A, 5-19.

[5] C. Zener, (1949). Journal of Applied Physics, 950-953.

[6] G.R. Purdy, J. Kirkaldy, (1963). Trans TMS-AIME, 1255-66.

[7] C. Atkinson, H.B Aaron, H.R Kinsman, H.I Aaronson, (1973). Met. Trans., 783-792.

[8] K.R. Kinsman, H.I. Aaronson (1973). Met. Trans., 959-967.

[9] J.R. Bradley, H.I. Aaronson, (1977). Met. Trans., 323-333.

[10] A. Béché, H. S. Zurob, and C. R. Hutchinson, (2007). Met. Trans. A, 2950-2955.

[11] J.S. Kirkaldy, (1957) Can. J. Phys, 907.

[12] G. R. Purdy, D. H. Welchert, J. S. Kirkaldy, (1964). Trans. TMS-AIME, 1025-34.

[13] D.E. Coates, (1972). Met. Trans. B, 1203-1212.

[14] D.E. Coates, (1973). Met. Trans. B, 395-396.

[15] D.E. Coates, (1973). Met. Trans. B, 1077–1086.

[16] D.E. Coates, Met. Trans B, (1973) 2313-2325.

[17] M. Goune, F. Danoix, J. Ågren, Y. Brechet, C.R. Hutchinson, M. Militzer, G. Purdy, S. van der Zwaag, H.S. Zurob, (2015). Mater. Sci. Eng. 1-38.

[18] M. Hillert, (1999). Acta Mater., 4481–4505.

[19] M. Hillert, J. Odqvist, and J. Agren, (2001) Scripta Mater., 221-227.

[20] M. Hillert, (1981). TMS-AIME, 789.

[21] A. Phillion, H.S. Zurob, C.R. Hutchinson, H. Guo, D.V. Malakhov, J. Nakano, G.R. Purdy, (2004). Metall. Mater. Trans. A, 1237-1242.

[22] C.R. Hutchinson, A. Fuchsmann, H.S. Zurob, Y. Brechet, (2004). Scripta Mater., 285-289.

[23] H. S. Zurob, C. R. Hutchinson, A. Beche, G. R. Purdy, and Y. J. M. Brechet, (2008). Acta Mater., 2203-2211.

[24] D. Panahi, (2013). Effect of Alloying Elements on Ferrite Growth in Ternary Fe-C-X Ternary Alloys, Ph.D. Thesis, McMaster University.

[25] H.S. Zurob, D. Panahi, C.R. Hutchinson, Y. Brechet, G.R. Purdy, (2013). Met. Mater. Trans. A, 3456-3471.

[26] J. Odqvist, M. Hillert, and J. Agren, (2002) Acta Mater., 3211-3225.

[27] A. Hultgren, (1947). Trans. ASM, 915-1005.

[28] M. Hillert, (1953). “Paraequilibrium,” Swedish Institute for metal research, Stockholm, Sweden.

[29] D. V. Malakhov, G. R. Purdy, (2002). Canadian Metallurgical Quarterly, 231-242.

[30] J.W. Cahn, (1962). Acta Met., 789–798.

[31] K. Lucke and K. Detert (1957) Acta metal., 628.

[32] K. Lucke and H. P. Stuwe, (1971). Acta Metall., 1087-1099.

[33] M. Hillert, (1969). “The Mechanism of Phase Transformation in Crystalline Solids,” Inst. of Metals, London, 33.

[34] M. Hillert, B. Sundman, (1976). Acta Metal., 731-743.

[35] M. Hillert, (2004). Acta Mater., 5289-5293.

[36] G. R. Purdy, Y. J. M. Brechet, (1995). Acta Met. Mater., 3763-3774.

[37] Y. Brechet, G.R. Purdy, (1990). Scripta Met. Mater., 1831-1835.

[38] Y. Brechet, G.R. Purdy (2003). Acta Mater., 5587-5592.

[39] W.D. Murray and F. Landis, (1959). Trans. ASME, 106–12.

[40] M.K. Miller, (2000). Atom Probe Tomography: Analysis At the Atomic Level. New York: Kluwer Academic.

[41] B. Gault, M.P. Moody, J.M. Cairney, S.P. Ringer, (2012). Atom Probe Microscopy. New York: Springer.

[42] H.P. Van Landeghem, B. Langelier, B. Gault, D. Panahi, A. Korinek, G.R Purdy, H.S. Zurob, (2017). Acta Mater., 536-543.

[43] H. Yuan, Internal Report, McMaster University, 2019.

[44] M.P Seah, (1980). J. Phys. F, 1043-1064.

[45] D.B. Williams, (1989). Ultramicroscopy, 38-51.

[46] T. Tanaka, H.I. Aaronson, M. Enomoto, (1995). Met. Trans. A, 561-580.

[47] J.H. Westbrook, (1964). Met. Rev., 415-430.

[48] J.R. Michael, D.B. Williams, (1984). Met. Trans. A, 99-105.

[49] H.D. Wu, G. Miyamoto, Z. Yang, H. Chen, T. Furuhara, (2018). Acta Mater. 68-77.

[50] N. Maruyama, G.D.W. Smith, A. Cerezo, (2004). Mater. Sci. Eng. A, 126-132.

[51] L. Stefanovich, E. Feldman, V. Yurchenko, A. Krajnikov, D.B. Williams, (2003). Surface Science, 99-108.

[52] C. Li, D.B. Williams, (2005). Phil. Mag., 2023-2032.

[53] J.H. Kang, B. Hosseinkhani, C.A. Williams, M.P. Moody, P. Bagot, P. Rivera-Diaz-del-Castillo, (2013). Scripta Mater., 630-633.

[54] H.P. Van Landeghem, B. Langelier, D. Panahi, G.R. Purdy, C.R. Hutchinson, G.A. Botton, H.S. Zurob, (2016). JOM, 1329-1334.

[55] B. Langelier, H.P. Van Landeghem, G.A. Botton, H.S. Zurob, (2017). Microscopy and Microanalysis, 385-395.

[56] H. Erhart and H. J. Grabke (1981). Met. Sci., 401-408.

[57] M. Enomoto, C.L. White, H.I. Aaronson, (1988). Met. Trans. A, 1807-1818.

[58] J. Agren, (1986). Scripta Metal., 1507-1510.

[59] J. Agren, (1982). Acta Metal., 841-51.

[60] H. S. Zurob, C. R. Hutchinson, Y. Brechet, and G. R. Purdy, (2005). “A study of the austenite to ferrite transformation in fe-c-x alloys using decarburization experiments,” in Proceedings of an International Conference on Solid-Solid Phase Transformations in Inorganic Materials 2005, Phoenix, AZ, United states, 111-116.

[61] C. R. Hutchinson, H. S. Zurob, and Y. Brechet, (2006). Metall. Mater. Trans. A, 1711-1720.

[62] M. Enomoto, (1999). Acta Mater., 3533-3540.

[63] W.W. Sun, H.S. Zurob, C.R. Hutchinson, (2017). Acta Mater., 62-74.

[64] C. Qiu, H.S. Zurob, C.R. Hutchinson, (2015). Acta Mater., 333-343.